INVESTIGATING RIBOSOMAL TRANSLOCATION MECHANISM WITH PRECISE MAGNETIC DNA RULERS

A Dissertation Presented to

the Faculty of the Department of Chemistry

University of Houston

In Partial Fulfillment

of the Requirements for the Degree of

Doctor of Philosophy

By

Heng Yin

August 2019

INVESTIGATING RIBOSOMAL TRANSLOCATION MECHANISM WITH PRECISE MAGNETIC DNA RULERS

Heng Yin

APPROVED:

Dr. Shoujun Xu, Chairman

Dr. Thomas S. Teets

Dr. Roman Czernuszewicz

Dr. Tai-Yen Chen

Dr. Masaya Fujita

Dean, College of Natural Sciences and Mathematics

Dedication

To my parents, He Yin and Wenrong Jiang:

Thank you for the love and understanding in this long journey

ACKNOWLEDGMENTS

Foremost, I would like to express my sincere gratitude to my advisor Dr. Shoujun Xu, for his continuous support and guidance of my Ph.D. study and research. He is always a patient advisor and motivates me to pursue truth in scientific research. He also taught me how to keep a 'strong mind' when facing difficulties, and persist to find solutions to solve challenging problems. There is an old Chinese proverb that says 'Give a man a fish and you feed him for a day. Teach a man to fish and you feed him for a lifetime.' I believe the training I obtained during my Ph.D. career will be beneficial to my entire life. My appreciation is extended to all of my committee members, Dr. Tai-Yen Chen, Dr. Roman Czernuszewicz, Dr. Thomas Teets, and Dr. Masaya Fujita for their time to review my dissertation.

My sincere appreciation goes out to all the members of the Dr. Xu group and Dr. Wang group. First, I appreciate Dr. Wang for her incisive comments and constructive suggestions in biochemistry field. None of my papers would be published without her continuous help. I am grateful to Dr. Te-wei Tsai who taught me how to operate and maintain the atomic magnetometer which is the most complicated instrument I have ever used. I am deeply thankful to Dr. Qionzheng Hu who gave me lots of invaluable research advice and guided me in biosensing research. I would also like to thank Dr. Haina Jia, Dr. Haopeng Yang, Ran Lin, and Miriam Gavriliuc for their tremendous help during my graduate research. In addition, I thank to Yi-ting Chen, Yujia Mao, Edgar Hinojosa and Yu Zhang in Dr. Xu's lab for their support and professional help. I would like to express my appreciation to all my friends. I thank Yang Song and Tianlang Yu for all the happy

memories we have; and Chengyi Wu, Chenchen Li, Tingting Liu for all the support and assistant.

In the last, I would like to extend my sincerest gratitude to my parents and girlfriend. I am grateful to my parents for their endless support and unconditional love. I could have never completed my degree without their love and understanding. I would thank to my girlfriend, Yu Zhang, the love for my life. I feel extremely lucky to meet you during the most difficult time in my life. Thank you for being with me for this long journey.

INVESTIGATING RIBOSOMAL TRANSLOCATION MECHANISM WITH PRECISE MAGNETIC DNA RULERS

An Abstract of a Dissertation

Presented to

the Faculty of the Department of Chemistry

University of Houston

In Partial Fulfillment

of the Requirements for the Degree of

Doctor of Philosophy

By

Heng Yin

August 2019

Abstract

This dissertation focuses on developing precise magnetic DNA rulers to investigate ribosomal translocation mechanism and measure the power stroke of translocase EF-G. The precise 3-nucleotide movement of mRNA is critical for translation fidelity. One mRNA translocation error propagates to all of the following codons, which is detrimental to the cell. However, frameshifting motifs without any secondary mRNA structures were identified but rarely studied experimentally. Through magnetic labeling on the 3′-ends of the mRNA, we observed efficient "-1" and "-2" frameshiftings on a mRNA containing a GA_7G slippery motif without the downstream secondary structure. The detection technique we used was force-induced remnant magnetization spectroscopy (FIRMS), which was invented by our group. The result represented the first experimental evidence of multiple frameshifting steps. To further reveal the mRNA dynamics near the ribosome entry site, I have developed an assay of dual magnetic DNA rulers that uniquely probe both the 3′- and 5′-ends of mRNA. An antibiotic-trapped intermediate state was observed, which indicated a novel ribosomal conformation containing mRNA asymmetric partial displacements at its entry and exit sites. Based on the available ribosome structures and computational simulations, we proposed a "looped" mRNA conformation, which suggested a stepwise "inchworm" mechanism for ribosomal translocation. The same "looped" intermediate state identified with the dual rulers persists with a "-1" frameshifting motif, indicating that the branching point of normal and frameshifting translocations occurs at a later stage of translocation. In the last, we reported quantitative measurements of the power strokes of structurally modified EF-Gs using both magnetic and microscope detections. The results

showed that the power stroke was reduced by 30 pN when the EF-G was restrained by a short crosslinking molecule or by the binding of fucidic acid. The results also showed that the reduced power stroke only lowered the percentage of translocation but did not introduce translocation error. Furthermore, the microscope detection method that I developed produced consistent results with the magnetic detection using FIRMS. Compared to magnetic detection, microscope detection is more straightforward, cheaper, and easier to implement. Therefore, it may be adapted to measuring other forces in biological systems.

TABLE OF CONTENTS

LIST OF FIGURES

LIST OF TABLES

LIST OF ABBREVIATIONS

FIRMS	Force-Induced Remnant Magnetization Spectroscopy
EXIRM	Exchanged-Induced Remnant Magnetization
ORFs	Open Reading Frames
EF-G	Elongation Factor G
GTP	Guanosine Triphosphate
PEP	Phosphoenolpyruvate
EF-Tu	Elongation Factor Thermo Unstable
EF-Ts	Elongation Factor Thermo Stable
ATP	Adenosine Triphosphate
PK	Pyruvate Kinase
EDTA	Ethylenediaminetetraacetic Acid
IPTG	Isopropyl β-D-1-Thiogalactopyranoside
PAGE	Polyacrylamide Gel Electrophoresis
PBS	Phosphate-Buffered Saline
SLP	Stem Loop
FPLC	Fast Protein Liquid Chromatography
TCA	Trichloroacetic Acid
PEG	Polyethylene Glycol
SDS	Sodium Dodecyl Sulfate

Chapter 1 Applications of Magnetic Labeling in Biomolecular Research

1.1 Introduction

Detection and purification of specific biomolecular targets, such as DNAs, proteins, bacteria, and even mammalian cells, are important in chemistry and biology. With the distinct advantages of molecule-specificity, high sensitivity, and single-molecular force manipulation, magnetic labeling has become a robust approach for biosensing. With affinity ligands conjugated onto their surfaces, magnetic particles ranging in size on the scale of nanometers to micrometers can selectively bind to the biological entities of interest.[1] Extensive applications have been reported in scientific literature, such as medium separation, imaging agents,[2] thermal generators,[3] drug carrier in clinical trials,[4] or force transducers in biophysical studies.[5]

In this chapter, I will review the fundamental properties and functionalization of magnetic particles and their corresponding biomolecular applications. The applications are divided into two categories. One is conventional single-function applications, such as biomolecular sorting, NMR imaging contrast agent, and guided drug delivery. The other is multi-function applications that have been recently developed including magnetic tweezers, DNA rulers based on FIRMS, mechanical force rulers, and exchange-induced remnant magnetization.

1.2 Physical properties of magnetic particles

Magnetic materials, based on iron, cobalt. nickel, or metal oxides, have played an important role in modern technology. Compared with bulk magnetic materials, magnetic particles show remarkable novel physical properties such as superparamagnetism, extra anisotropy contribution, high field irreversibility and saturation field.[6] These new properties arise from their small volume, single-magnetic domain, and unusual surface effects of individual particles.[7] Typical magnetic particles can be paramagnetic, ferromagnetic, antiferromagnetic, or superparamagnetic based on their magnetic behavior in the presence or absence of an external magnetic field. When the particle size is less than the size of single-magnetic domain, the coercivity decreases to zero and particles exhibit superparamagnetic property. For instance, Fe-based nanoparticles become superparamagnetic at size below 25 nm.[8]

Superparamagnetic nanoparticles have a unique advantage in application of biomolecular research due to their "magnetic switch" property. Their thermal fluctuations are strong enough to spontaneously demagnetize a previously saturated assembly. Consequently, these particles have zero coercivity and no hysteresis.[6] Therefore, superparamagnetic nanoparticles are magnetic only in the presence of an external magnetic field. Once the magnetic field is removed, the magnetic property disappears immediately and the magnetic moment of entire crystallites no longer aligns with the magnetic field.[9] (Figure 1.1) Because of the instantaneous magnetic switching property, superparamagnetic nanoparticles are widely used as hyperthermia material, NMR contras agent, and as a drug delivery carrier. Theoretically, relatively larger superparamagnetic nanoparticles are

favored due to their larger magnetic moments. But a balance is necessary between ideal magnetic property and appropriate biocompatibility. This is the reason why ferrite oxide-magnetite (Fe_3O_4) is one of the best candidates for a broad range of biological applications.[10,11]

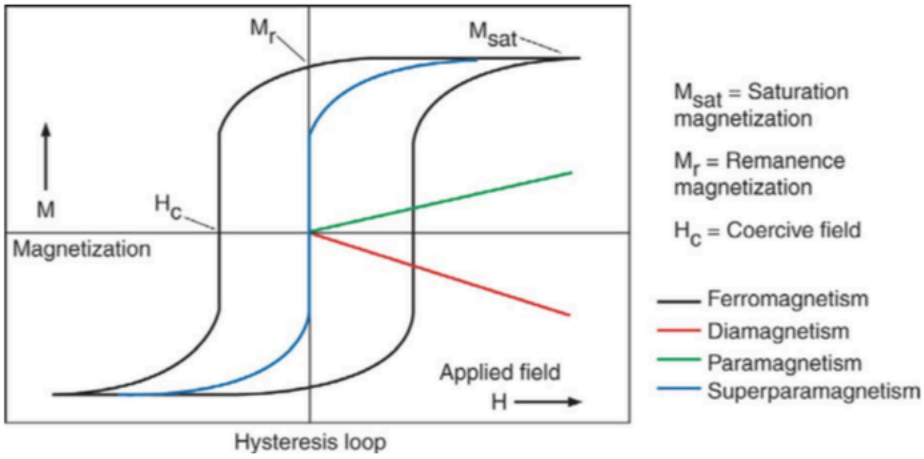

Figure 1.1 Hysteresis loops of various magnetic particles. The figure also indicates the values of the remanence, M_r, and coercive filed, H_c, Reprinted with permission from Ref. 9.

When an external alternating magnetic field is applied, magnetic particles re-orientate their magnetic moments and generate heat because of Néel relaxation or Brownian relaxation. Néel relaxation occurs when the rotation of the magnetic moment within magnetic particles exceeds their anisotropy energy barrier, while Brownian relaxation comes from the mechanical rotation of magnetic particles that induces frictional losses with surroundings.[12] The relaxation process occurring in magnetic particles is utilized in magnetic hyperthermia therapy application.

In addition, magnetic particles generate a small local magnetic field to the surrounding protons, which lead to shorter relaxation times (T_1 and T_2). T_1 and T_2

represents the longitudinal and transverse proton relaxation times, respectively. The longitudinal relaxation time covers the population redistribution of the nuclear spin states, while the transverse relaxation time indicates the decoherence of the magnetization of the precessing protons. The presence of magnetic particles in biological environment specifically shortens T_2 and less effectively shortens T_1, hence improves the differentiation of signals in magnetic resonance imaging (MRI) as contrast enhancing agents.[13,14]

1.3 Labeling strategies for molecular sensing

Magnetic particles can be conveniently labeled with biomolecular targets, such as DNAs, proteins, antibodies, even bacteria or mammalian cells, which subsequently convert molecular information into magnetic signals.[15] To achieve a highly sensitive biomolecular sensing, an appropriate labeling strategy is necessary, which is determined by the chemical properties of magnetic particles surfaces, the characteristics of targeting molecules, and the desired applications.[16]

Covalent and noncovalent conjugation are both commonly used in magnetic particles labeling but for different purposes. In general, covalent bonds can be formed between functional groups such as amine ($-NH_2$), carboxylic acid (-COOH), hydroxyl (-OH), and sulfhydryl (-SH), and the surface of magnetic particles.[17] In addition to these conventional covalent bonds, Sletten et al. (2009, 2011) developed biorthogonal reactions that facilitated azide-alkyne Huisgen cycloaddition to achieve selective targeting, which enabled the high-precision chemical modification of biomolecules in vitro, as well as real-time visualization of molecules in cells and live organisms.[18,19] Noncovalent bonds are typically much weaker than covalent bonds, but multiple non-covalent interactions can

produce stable, specific linkages between different molecules. Streptavidin-biotin conjugation is one of the most typical representatives of multiple noncovalent interactions, which is capable to interact with up to four biotin molecules (Figure 1.2). Due to its relatively small molecular mass, the streptavidin-biotin conjugation has ideal biocompatibility and maintains the integrity of functionalities on surface.[20]

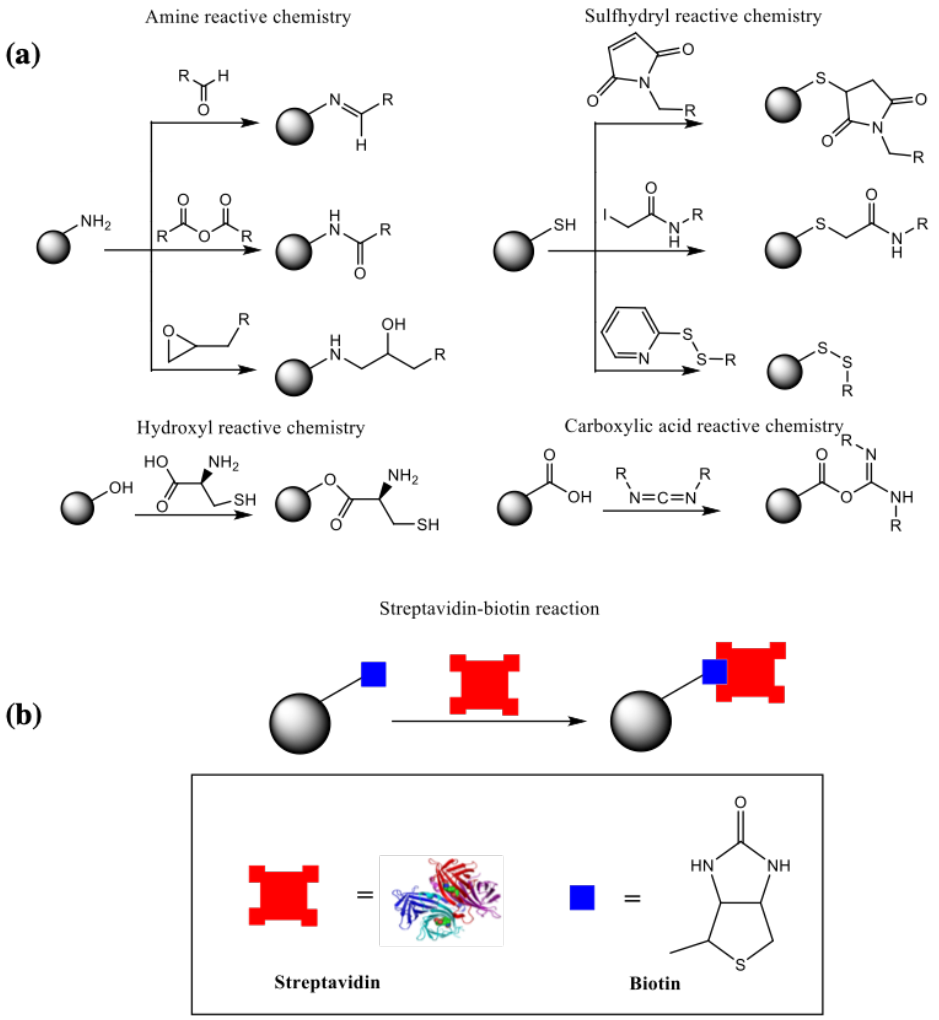

Figure 1.2 Magnetic particles surface conjugations. **(a)** Example of representative covalent bonding. **(b)** Schematic illustration of noncovalent conjugation commonly used for bioconjugation.

In magnetic-sensing research, most of the labeling strategies can be categorized into direct labeling, surface labeling, and multi-layer labeling. Direct labeling is achieved by mixing magnetic particles with the ligands that bind with the target molecules. While in the approach of surface labeling, a solid substrate/sensor surface functionalized with affinity ligands captures the target molecules first, then the target molecules are selectively coupled with magnetic particles via secondary affinity ligands. For instance, in Figure 1.3 (a), after a biotin-streptavidin coated surface is functionalized with specific DNA strand, it subsequently couples with magnetic particles labeled with complementary DNA strand.[21] This strategy is well-suited to detect a small field-of-view targeting molecules with high sensitivity. To further improve the detection sensitivity, a multi-layer labeling can be formed by sequentially applying magnetic particles conjugated with orthogonal binding partners.[22] Liong et al. (2011) reported to utilize oligonucleotide hybridization as a cell-labeling method to significantly amplify the loading of magnetic probes onto target cells.[23] (Figure 1.3 (b))

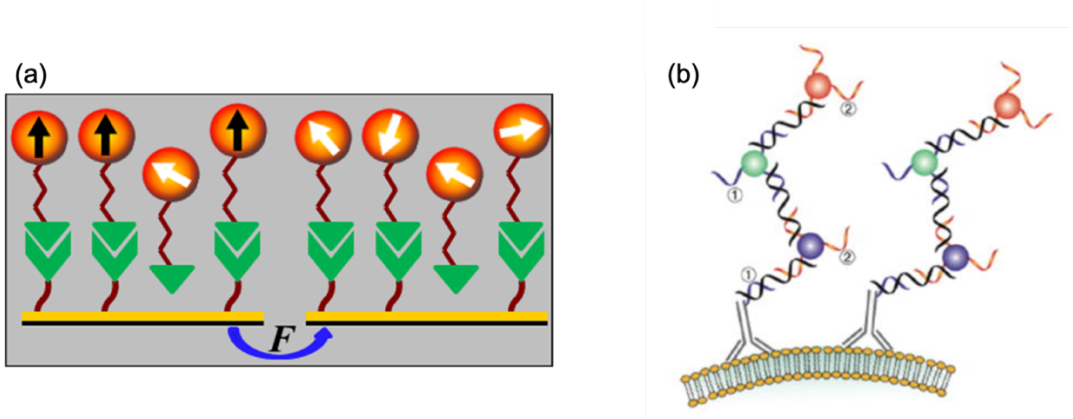

Figure 1.3 (a) By functionalizing a solid substrate surface with affinity ligands, small molecular targets can be effectively immobilized onto a surface. Magnetic particles are captured through secondary affinity ligands. **(b)** By grafting multiple layers of magnetic particles onto a target, magnetic signals can be amplified to detect rare molecular targets. Reprinted with permission from Ref. 21 and 23.

1.4 Single-function applications

1.4.1 Biomolecular separation and sorting

Separation, purification, and manipulated sorting of biomolecules are of great importance in biotechnology and life sciences. Conventional protocols that currently being used include electrophoresis, precipitation, ultrafiltration, and chromatography.[1,2] However, recently developed magnetic particles labeling provides an alternative option, especially for inhomogeneous matters such as protein or DNA mixtures. The magnetic separation or sorting has the advantages of being simple, cheap, and scalable. Only small quantities of biomolecules are needed because of the high surface-to-volume ratio of magnetic particles. In addition, dedicated equipments and pre-concentration are not required for magnetic separation or sorting.

In the most common magnetic separation procedure, affinity tags or ligands immobilized magnetic particles are mixed with the desired bio-targets. These bio-targets could be DNAs, proteins, or even cells. After sufficient incubation, the desired bio-targets bind to the magnetic particles and are subsequently isolated by an external magnetic field. Finally, the desired bio-targets are dissociated from magnetic particles by proper elution procedures. Affinity tags or ligands on magnetic particles are specifically designed for different separation requirements. But in most strategies, DNA or RNA are isolated by magnetic particles with complementary strands. Nitrilotriacetic acid (NTA) functionalized magnetic particles have high affinity and specificity to His-tagged protein.[25] Nucleic acids can also be purified by amine-functionalized magnetic particles. Except for small biomolecules, magnetic particles also contribute to the extract specific cells. In a

pioneering study in 1988, Lund et al. (1988) exploited mAbs coated magnetic beads to separate K88 (F4) fimbrail antigen.[26] Hornes et al. (1991) further developed it for immune-magnetic separation of enterotoxigenic *E. coli* strains.[27]

In recent years, magnetic particles have also widely been used in microfluidics for micromolecular sorting. Pamme et al. (2006) achieved continuous sorting of magnetic cells via on-chip free-flow magnetophoresis.[28] As shown in Figure 1.4, a flat separation chamber with numbers of inlet and outlet channels generated Laminar flow. Meanwhile, a permanent magnet applied a strong magnetic field perpendicular to the direction of flow. Non-magnetic particles left the chamber and were deflected into the inlet channels while magnetic particles were dragged by magnetic field and were deflected into one of the outlet channels. Figure 1.4(b) shows that sorting depends on size and magnetic susceptibility. Different biological cells labeled with different magnetic particles are selectively sorted according to their magnetic loadings. However, a long-standing problem for this method is that channels are easily clogged by magnetic particles. To solve this problem, Sista et al. (2008) developed a droplet-based manipulation of magnetic beads without any channels to sort sandwich heterogeneous immunoassays on human insulin and interleukin-6 with a total time of seven minutes for each assay.[29] The results presented a 100% bead retention after 7776-fold dilution-based washing of the supernatant.

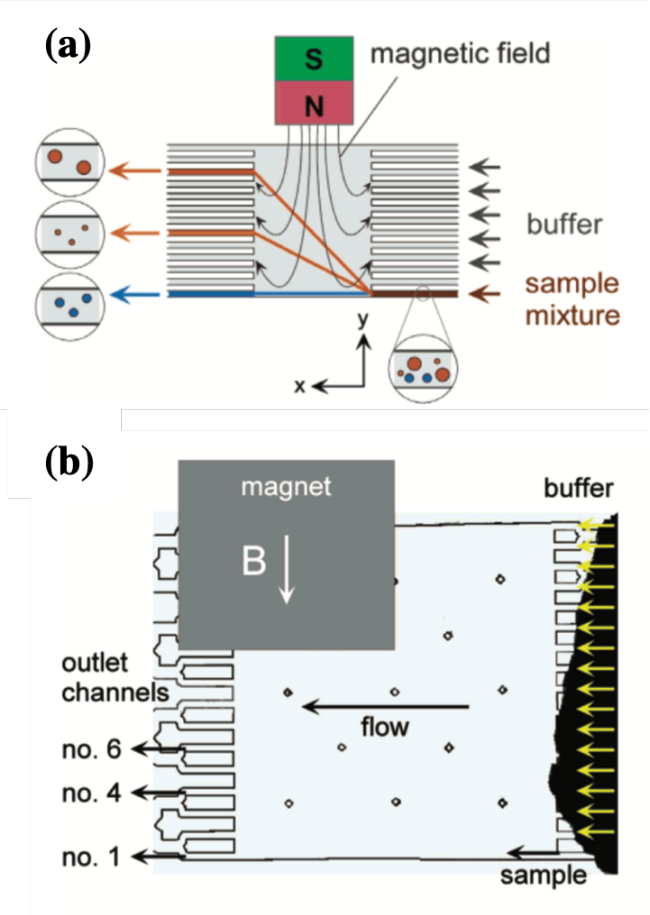

Figure 1.4 (a) The principle of free-flow magnetophoresis **(b)** Separation of different types of magnetic particles from each other as well as from non-magnetic particles. Reprinted with permission from Ref. 28.

1.4.2 Imaging contrast agent

Diagnosis of tumors, tissue damage, and neurological disorders has been a long-standing issue for medical research. Since the 1970s, improvements in imaging techniques have greatly contributed to solving this problem.[30] Among all the imaging techniques, magnetic resonance imaging (MRI) is one of the most important and feasible techniques. MRI offers several advantages such as no irradiation, possibility to generate 3D images, excellent spatial resolution with optimal contrast with soft tissues, and good signal-to-noise

ratio.[31] However, even with MRI's superior spatial resolution, improvements are still needed and such improvements can be feasible with the use of a special chemical medium called imaging contrast agent.[2]

The underlying principle of contrast imaging is that the agents will alter the relaxation time of their nearby nuclear spins. There are two types of relaxation times, T_1 and T_2, for the polarized nuclear spins in a strong magnetic field. T_1 means the time required for excited nuclei to come back to original ground state and accompanied with energy loss to the environment (spin-lattice relaxation). T_2, the spin-spin relaxation, means the exchange of energy between high and low energy nuclei without loss of energy to surrounding nuclei.[32] Therefore, two types of MRI contrast agents exist: one that increases the T_1 signal in T_1-weighted images, which results in a positive/brighter contrast, and the other that reduces the T_2 signal in T_2-weighted image, which results in a negative/dark contrast.[33] However, due to undesired detection sensitivity and cytotoxic concerns of gadolinium-based T_1 contrast agents, iron oxide-based T_2 contrast agent can find unique biomedical applications.[34]

Two different types of iron oxide nanoparticles are the most typically used T_2 contrast agents: magnetite (Fe_3O_4) and its oxidized and more stable form of maghemite (γ-Fe_2O_3). Table 1.1[35] shows the main properties of these two types of nanoparticles. Different sizes of iron oxide nanoparticles provide multiple choices for various clinical uses. Since they all exhibit superparamagnetic behavior, they lose their magnetization in the absence of external magnetic field, which provides a real-time biological response.[36] The main disadvantage of iron oxide nanoparticles is the aggregation of particles due to Van der

Waals force. To avoid the aggregation, surface modification with polymers is commonly used and has proved to have a positive contribution to biological distribution.[37]

Table 1.1 Properties of iron oxide nanoparticles

Name	Core material	Surface	Core Size (nm)	Hydrodynamic Diameter (nm)	r_2 ($mM^{-1}*s^{-1}$)	Magnetic field (T)
Ferumoxides	Fe_3O_4-γ-Fe_2O_3	Dextran	4.96	~ 200	120	1.5
Ferucarbotran	Fe_3O_4	Carboxydextran	4.2	> 50	186	1.5
Ferumoxtran	Fe_3O_4	Dextran	5.85	< 50	65	1.5

Reprint with permission from Ref. 35.

Regardless of the materials being used, the first and major prerequisite of contrast agents is the clear identification of magnetic biomarkers. The magnetic biomarker should specifically bind on the desired targets and have a clear difference compared to the surroundings. Figure 1.5 shows tumor-bearing mice were prepared by subcutaneous injection of the SKBR-3 and KB cells into the left and right lateral thighs, respectively. MRI of the mice was performed at scheduled times after the intravenous injection of herceptin-nanoparticles. The images clearly indicate that, for both black-white or color MRI, a significant improvement is observed after applying contrast agents.[38] Although the problems of toxicity and adverse side effects exist, magnetic nanoparticles have been proved an efficient method to enhance MRI contrast.

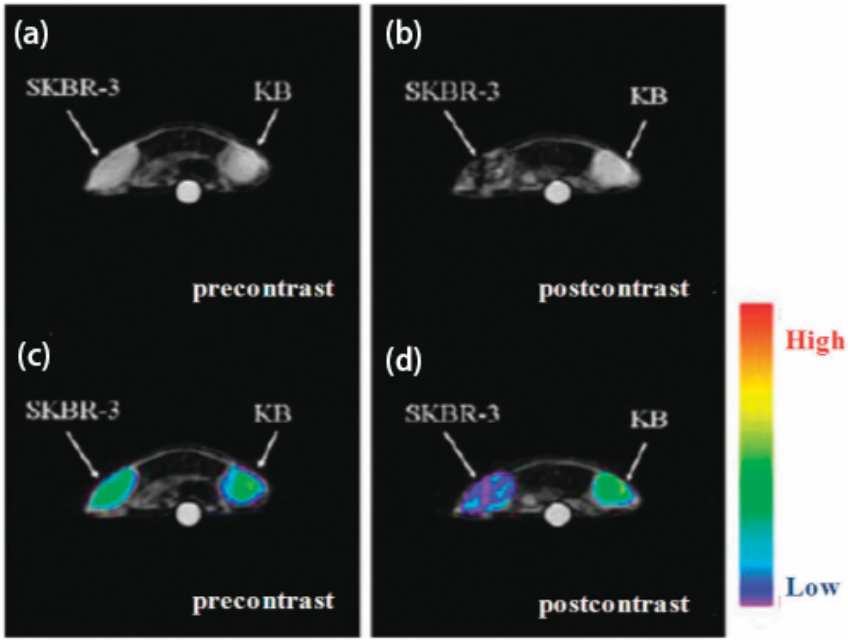

Figure 1.5 Target-specific detection of two different breast cancer types (SKBR-3 and KB) by anti-Her2/neu-magnetic nanoparticles (a–d). **(a)** and **(b)** are traditional black–white MRI, and **(c)** and **(d)** show color maps. **(a)** and **(c)** MRIs show the pre-contrast, and **(b)** and **(d)** display the post- contrast. Reprinted with permission from Ref. 38.

1.4.3 Guided drug delivery

The primary shortcomings of most chemotherapeutic agents are their high cytotoxicity and poor specificity for the intended biological target. In recent years, different organic materials (polymeric nanoparticles, liposomes, micelles) have been developed as drug delivery vectors using either passive targeting or active targeting. However, these organic systems still present limited chemical and mechanical stability, sensitive susceptibility, and especially inaccurate drug release.[9]

To overcome these problems, the idea of utilizing magnetic nanoparticles to guide drug delivery has been investigated for decades and shows advantages compared to other drug delivery methods. By exploiting an implanted permanent magnet or an external

magnetic field, magnetic nanoparticles deliver drugs to precise targets of desired diseased sites, and the drug release is easily triggered by a magnetic field change (see Figure 1.6). It is also important to notice that the accumulation of magnetic nanoparticles is also capable of absorbing near-infrared, microwave, and ultrasound radiation for hyperthermia treatment. [4]

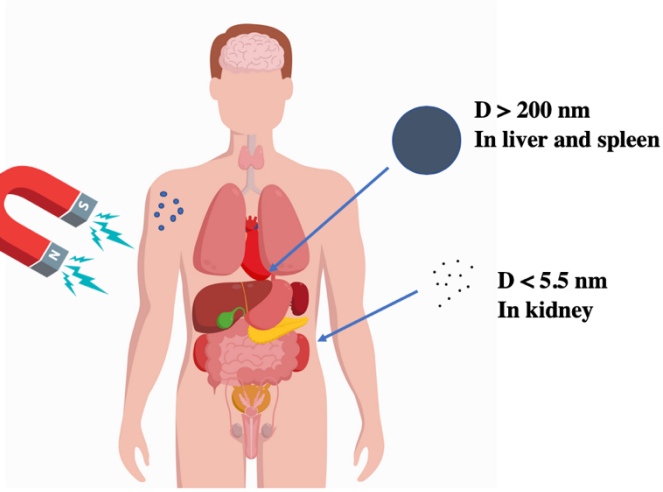

Figure 1.6 Image shows that by exploiting an external magnetic field, magnetic nanoparticles deliver drugs to precisely target the desired diseased sites. Large magnetic nanoparticles (D > 200 nm) are accumulated in liver and spleen, while small magnetic nanoparticles (D < 5.5 nm) are removed through kidney.

There are two common mechanisms for magnetic-nanoparticles-guided the drug delivery: the passive targeting and the active targeting. The passive targeting route takes the advantage of the biological function of reticuloendothelial system (RES), including bone marrow progenitors, blood monocytes, and tissue macrophages. Once the magnetic nanoparticles are immersed into the blood stream, the RES recognizes them and adsorbs the magnetic nanoparticles on their surfaces. The final destination of these nanoparticles mainly depends on their sizes. Large magnetic nanoparticles (> 200 nm) are easily detected

by the immune system and removed from the blood and finally delivered to the liver and the spleen. Very small magnetic nanoparticles (< 5.5 nm) can be excreted through the kidneys.[39] Therefore, The optimal magnetic nanoparticle size for drug delivery treatments ranges between 10 to 100 nm,[40,41] as these have the longest blood circulation time (see Figure 1.6). However, comprehensive factors need to be considered to decide the optimal particle size. On one hand, smaller nanoparticles have longer blood circulation time and consequently have more chance to be captured to desired tissue by an external magnet; on the other hand, bigger nanoparticles have stronger magnetic force and less likely to be influenced by the viscosity of blood.[42]

In contrast with passive targeting, active targeting has the advantage of higher efficiency of target binding but involves more complicated designs for the magnetic nanoparticles. By binding on the targeted tissues with receptor-ligand or antigen-antibody interactions, the nanoparticles have a better affinity and longer residence time. Targeting ligands, such as proteins,[43] peptides,[44] aptamers,[45,46] and small molecules,[47] have been designed to immobilize on magnetic nanoparticles to improve accumulation ability.

The main limitation of magnetic-nanoparticles-guided drug delivery is the significant magnetic gradient field generated by external magnets. Not all the magnetic nanoparticles are well controlled and are able to be attracted to desired tissues. Furthermore, the effective depth underneath the skin is not satisfactory. Even using permanent Nd-Fe-B magnets in combination with superparamagnetic iron oxide nanoparticles, which have excellent magnetic properties, the effective magnetic field depths only reaches 10-15 cm underneath the body.[48] Therefore, a deeper understanding of the magnetic gradient and

better magnetic materials are necessary to improve the practical application of magnetic labeling in drug delivery.

1.5 Multi-function applications

1.5.1 Magnetic tweezers

Magnetic tweezers is a single-molecule force technique that investigates biomolecular interactions. As one of the most important parts of magnetic tweezers configuration, the magnetic particles serve not only as a force transducer, but also as a signal transducer and carrier. This bi-functional magnetic system provides a robust tool to study a biomolecule's stretching and twisting forces with high resolution.[49–51] A common setup of magnetic tweezers is shown in Figure 1.7.[52] A paramagnetic particle is tethered to the surface via biomolecular interactions, such as a DNA molecule. Meanwhile, another particle is immobilized directly to the surface as a reference. The paramagnetic particle is manipulated by a permanent magnet and the generated force is proportional to the gradient of the magnetic field.[53,54] In recent years, electromagnetic tweezers has been developed to achieve a faster control of the magnetic field, which employs electromagnets to generate the field.[55] However, the main disadvantages are the inevitable hysteretic effect in the ferromagnetic core and poor integration of electromagnets.[56]

The cores of magnetic tweezers are the particle tracking and 3D modeling. Typically, the movement of both the magnetic particle and the reference particle are tracked by a charge-coupled device (CCD) camera and a real time motion signal is recorded by a computer for magnetic control. To minimize the instrumental drift, the movement of

DNA tethered particle is calibrated by the surface immobilized particle as reference. Detecting the x-y locations of the particles is relatively simple, either by direct fitting of the subpixel location of the bead[57] or by image-reference cross-correlation.[55,58] However, the movement along the z axis is difficult to track if the diameter of magnetic bead is close to wavelength of the incident light. In this case, the image quality is significantly affected by diffraction.[59] To solve this problem, Kim et al. (2008, 2009) combined reflection interference contrast microscopy with magnetic tweezer to improve the z-axis resolution of images.[60,61]

The position resolution of magnetic tweezer is primarily limited by two reasons: the Brownian motion of the bead and the intrinsic resolution of the instrument depends on the sensing technique and stability. Berg-Sorensen and Flyvbjerg (2004) proposed an equation to interpret the Brownian motion of the bead in aqueous environment and the power spectrum of bead motion was found to be Lorentzian:[62]

$$S(f) = \frac{kT}{\pi^2 \xi (f^2 + f_0^2)}$$

Here, S(f) is the power spectrum of the bead motion, ξ is the hydrodynamic drag coefficient, k is the Boltzmann constant, and f is the mechanical response frequency of the DNA-bead tether. Thus, under constant temperature, smaller beads, shorter tethers, and a smaller f value will lead to a better power spectrum of the beads motion.

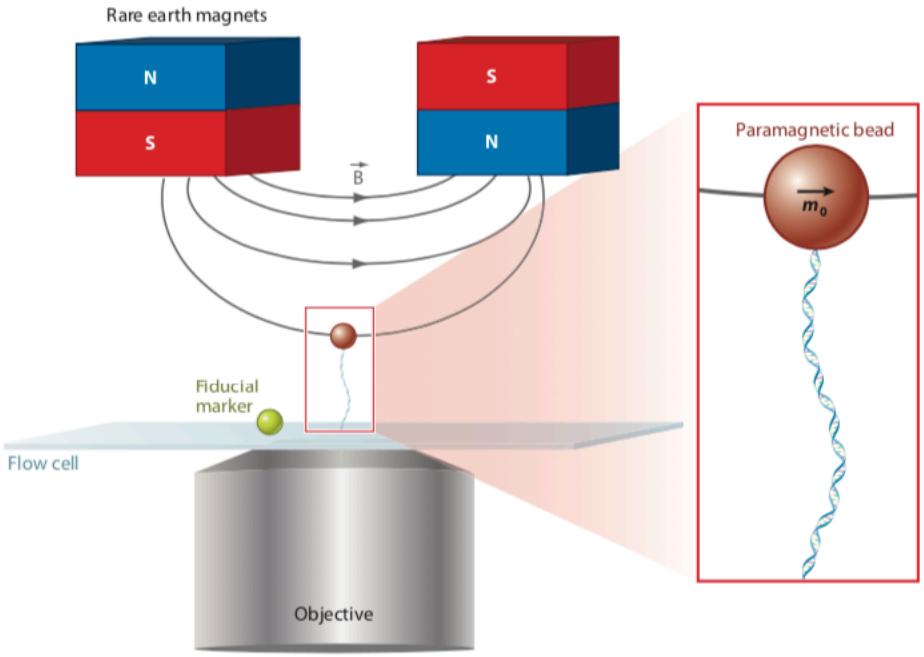

Figure 1.7 Schematic of basic implementation of magnetic tweezers. A paramagnetic bead is tethered to the surface via the biomolecule of interest. The magnetic field generated by a pair of permanent magnets induces a magnetic moment in the paramagnetic bead. The bead experiences a force proportional to the gradient of the field. The molecule can be coiled by rotating the external magnet. Abbreviations: N, magnetic north pole; S, magnetic south pole. Reprinted with permission from Ref. 52.

In addition, significant efforts have been made to increase the throughput and broaden the application scope of magnetic tweezers. Since Ribeck et al. (2008) proved the feasibility to control parallel single-DNA manipulation with magnetic tweezers,[63] the multiplexed magnetic tweezers showed promises in the study of collagen-associated extracellular matrix proteolysis,[64,65] competitive antibody-antigen interactions,[66] and DNA cleavage activity of type III restriction enzymes.[67,68] Furthermore, the hybridizations between magnetic tweezers and other manipulation or sensing techniques have expanded the capability of magnetic tweezers in more complex systems. Crut et al. (2007) combined magnetic tweezers and optical tweezers to achieve a three-dimensional manipulation of

DNA molecules.[69] Schroff et al.[70] (2005) and Hugel et al.[71] (2007) investigated the dynamics of an enzyme on DNA by combining Forster resonance energy transfer (FRET) with magnetic tweezers.

1.5.2 DNA rulers based on FIRMS

Ribosomal translocation is one of the most essential steps of protein synthesis, during which the ribosome moves exactly three nucleotides to decode the mRNA to the amino acid. However, most of ribosome sensing techniques are not capable to precisely detect the position of the ribosome, which makes the mechanism of accurate mRNA movement remain elusive. For example, the toe-printing assay uses a reserve transcriptase primed at the 3'-distal end to transcribe the mRNA toward the ribosome but it is not capable to measure 5'-distal end.[72] The ribosome profiling method maps ribosome-covered mRNA but it lacks single-codon precision.[73]

DNA rulers based on force-induced remnant magnetization spectroscopy (FIRMS) was recently developed to reveal the position and mechanism of ribosome movement with single-nucleotide resolution. Briefly, different lengths of DNA rulers formed different lengths of duplexes with a portion of the mRNA uncovered by the ribosome. The magnetic particles labeled on either the DNA rulers or the mRNA are dissociated from the surface by gradually applying external mechanical forces to induce the rupture of the duplex. The rupture of the duplex is indicated by a decrease in the magnetic signal due to the dipole randomization of the dissociated magnetic particles. The duplex-binding force is determined from the FIRMS spectrum by differentiating the magnetization curve as a function of the force amplitude.[74] The force spectra of the duplexes with different lengths

are combined to locate the position of the ribosome from both the entrance and exit sites with single-nucleotide resolution.[75] Figure 1.8 shows the schematic of DNA rulers. The typical force range of the DNA rulers is 20-100 pN and on the order of 10^5 duplex bonds are simultaneously measured within a macroscopic filed-of-view of several mm^2.

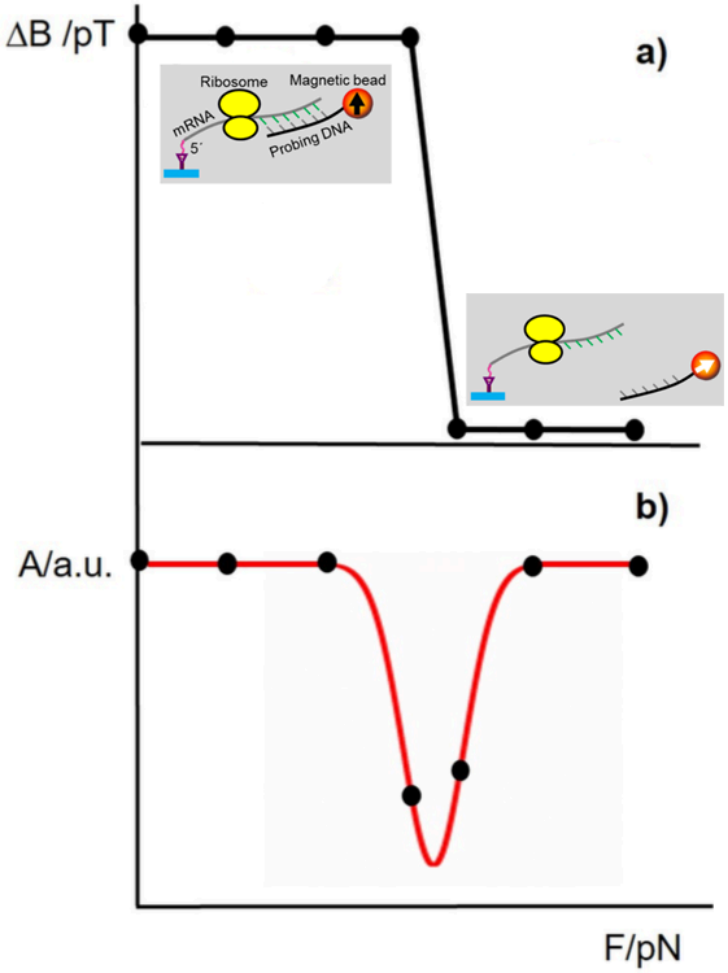

Figure 1.8 Schematic of DNA rulers based on FIRMS. **(a)** Magnetic signal decrease after applying external forces. **(b)** Corresponding FIRMS.

In the DNA rulers technique, the magnetic particles are not only manipulated by the external force, but also provide the magnetic signal to indicate the rupture of the duplex bonds. The magnetic signal is precisely detected by an atomic magnetometer, which is the

most sensitive device to measure a magnetic field under physiological temperature.[76] Atomic magnetometers are based on the nonlinear magneto-optical resonance of alkali atoms interacting with a polarized laser beam. The sensor is paraffin coated to reduce the decoherence from the collisions among polarized atoms. Polarized by the laser beam, the atomic polarization processes in the magnetic field and subsequently rotates the polarization axis of the laser. When the modulation frequency of laser matches the atomic Larmor frequency, the magneto-optical resonance is observed and magnetic field is derived by dividing the modulation frequency by the gyromagnetic ratio of the atoms.[77]

Through mapping the position of ribosome, the DNA rulers technique has been utilized to investigate the power stroke mechanism,[78] unusual frameshifting,[79] and intermediate states during translocation.[75] It provides a valuable complement to conventional methods, such as X-ray crystallography and cryogenic electron microscopy to study the mechanism of ribosome functions.

1.5.3 Mechanical force rulers

The resolution and subsequent selective control of molecular bonds are of great significance in chemistry and biology. Both optical and magnetic labeling are widely used to identify molecules and cells. While optical labeling uses wavelength parameters to distinguish different molecular and cellular bindings, the magnetic labeling shows less capability in this field of study.[80–83] It relies on either a washing process to remove nonspecifically bound magnetic particles[84] or a measurement of relaxation times of bound magnetic particles in contrast with free particles.[85]

The mechanical force rulers based on FIRMS was a recently developed technique that implemented external force as the distinguishing parameter in magnetic detection to achieve molecular and cellar specificity. When the amplitude of an external force exceeds the molecular or cellar noncovalent bonds, the magnetically labeled molecules dissociate from the surface and undergo Brownian motion, which results in a magnetic signal decrease detected by atomic magnetometer.

The mechanical force rulers show the capability with unambiguous differentiation of specifically and physically absorbed magnetic particles due to the binding force difference of various molecular pairs. In Figure 1.9,[74] magnetic particles bind to human CD3 + T cells surface by the CD3 antibody, whereas particles without CD3 antibody are physisorbed. The antibody-antigen bound and physisorbed particles dissociate under different mechanical forces, yielding distinct force spectra. Therefore, the magnetization difference before and after the force disturbance represents the number of magnetic particles with this specific binding force. In addition to being able to distinguish binding force on a cell surface, a characterization of noncovalent antibody-antigen bonds on a molecular level was also fulfilled by the mechanical force rulers. Figure 1.10 shows the physisorption and specific bonds between IgG−α-IgG under different conditions.[21] The physisorbed and specifically bound magnetic particles were clearly distinguished by the force spectra.

In summary, the mechanical force rulers offer a novel and quantitative method to reveal different binding types among molecular or cellar interactions, which is not well

achieved in other magnetic labeling methods. The mechanical force is potentially capable of serving as an indicator for particular biomarkers.

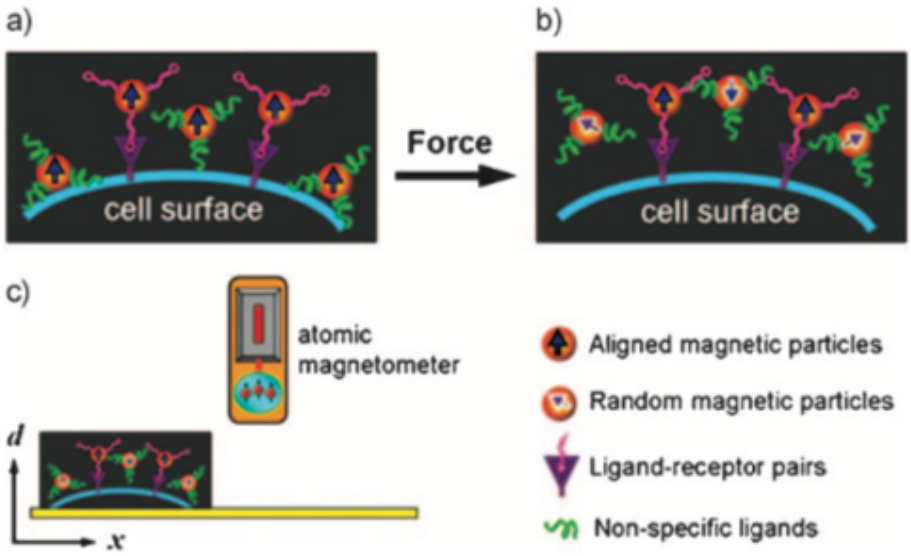

Figure 1.9 The mechanical force ruler method. **(a)** Binding between magnetic particles and cells without an external disturbing force; **(b)** An external force induces dissociation of weakly-bound magnetic particles; **(c)** Scanning magnetic imaging. The sample is scanned along the x axis; the magnetic field along the d axis is measured by an atomic magnetometer during scanning. Reprinted with permission from Ref. 74.

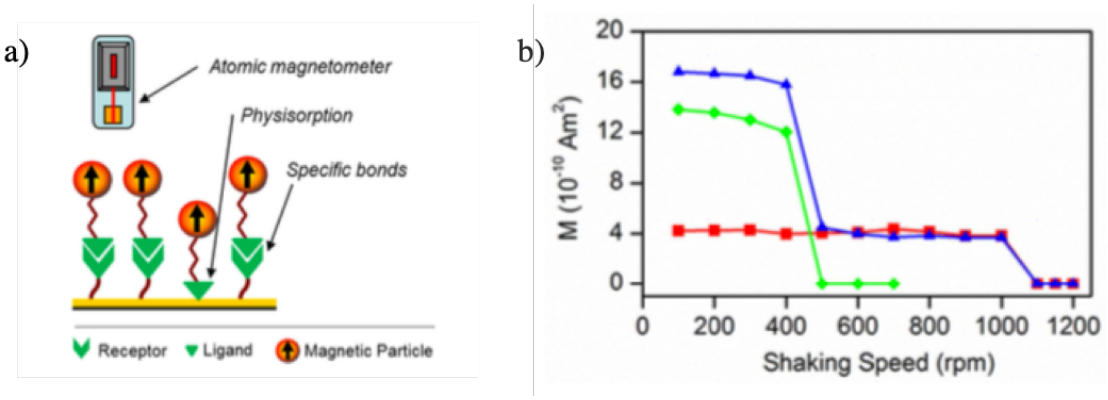

Figure 1.10 Application of FIRMS for distinguishing physisorbed and specifically bound magnetic particles. **(a)** The targeted receptor molecules are immobilized on the surface of a substrate, while the ligand molecules are conjugated with magnetic particles. **(b)** Plots of magnetization M vs shaking force for magnetically labeled α-mouse IgG binding to a bare gold surface (green trace) and IgG-coated gold surface (red and blue traces). M is the total magnetic moment of the magnetic particles. The error bar for the magnetization values is approximately 5×10^{-12} A•m^2. Reprinted with permission from Ref. 21.

1.5.4 Exchange-induced remnant magnetization

MicroRNAs (miRNAs) are short RNA strands containing 18-25 nucleotides that play important roles on gene expression, cell differentiation, and disease development.[86–88] However, due to short distance and diverse expression levels of miRNA, the high detection sensitivity is difficult for conventional techniques like northern blotting,[89] reverse transcriptase polymerase chain reaction,[90] in situ hybridization,[91] and microarray.[92] The low-detection limit of magnetic labeling provides a promising development in this field. The recently developed exchange-induced remnant magnetization (EXIRM) exploited high-specificity magnetic detection to reach a picomole sensitivity.

Figure 1.11 shows the basic principle of the EXIRM technique.[93] The target miRNA 1 is immobilized on the surface and forms a single-base mismatched duplex with miRNA 2 which is labeled with a magnetic particle. When miRNA 3 is introduced and incubated with the RNA duplex, miRNA 2 is replaced because miRNA 3 has thermodynamically stronger binding to miRNA 1. The dissociation of miRNA 2 leads to randomization of the magnetic dipoles of the magnetic particles due to Brownian motion and a decrease of magnetic signal is detected by the atomic magnetometer.

The EXIRM technique avoids some of the shortcomings associated with other analytical techniques, such as amplification, purification, and extensive washing. Its straightforward procedure ensures high reliability of the measurements. However, an improved EXIRM with higher throughput and shorter reaction time is necessary for broader applications.

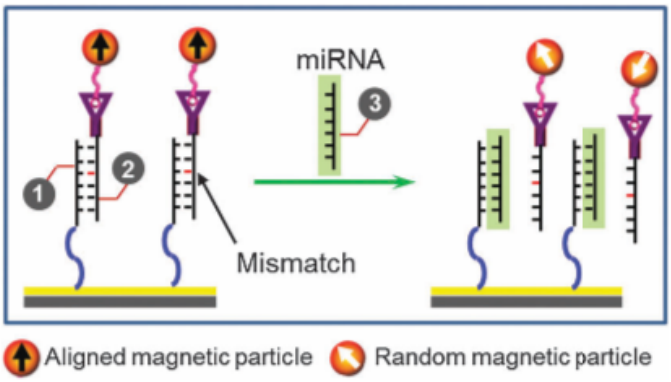

Figure 1.11 Principle of the EXIRM technique. Three RNA strands are involved: immobilized strand 1, strand 2 with one mismatched base, and strand 3 of the target miRNA. Strand 2 is hybridized with strand 1 and is labelled by a magnetic particle. The particles are magnetically aligned before exchange but randomized after exchange-induced dissociation. Reprinted with permission from Ref. 93.

1.6 Summary and perspectives

Magnetic labeling has shown diverse applications in biomolecular research ranging from sensing, sorting, drug delivery carrier, to force dragger, and signal transducers. Multiple synthesis and labeling strategies provide the physical and chemical foundations for versatile applications. Therefore, iron-oxide based magnetic particles inducing significant relaxation time have been favored to MRI contrast agents; biocompatible size and easily ligands-labeled surface make magnetic particles a good candidate for biomolecular sorting and drug delivery. In addition, recent developed single-molecule manipulated techniques utilize their unique magnetic properties to investigate single-molecule interactions like DNA-DNA duplex bonds and antibody-antigen bonds. A future goal for the development of magnetic labeling is to achieve better magnetic property, stable biocompatibility, and robust labeling protocols. Improvements in these aspects will bring benefits to biological analysis and medical research.

1.7 References

1. Chen, Y.-T., Kolhatkar, A. G., Zenasni, O., Xu, S. & Lee, T. R. Biosensing using magnetic particle detection techniques. *Sensors* **17**, 2300 (2017).
2. Felton, C., Karmakar, A., Gartia, Y., Ramidi, P., Biris, A. & Ghosh, A. Magnetic nanoparticles as contrast agents in biomedical imaging: recent advances in iron- and manganese-based magnetic nanoparticles. *Drug Metab. Rev.* **46**, 142–154 (2014).
3. Yoo, D., Lee, J.-H., Shin, T.-H. & Cheon, J. Theranostic magnetic nanoparticles. *Acc. Chem. Res.* **44**, 863–874 (2011).
4. Dobson, J. Magnetic nanoparticles for drug delivery. *Drug Dev. Res.* **67**, 55–60 (2006).
5. Ebrahimian, H., Giesguth, M., Dietz, K.-J., Reiss, G. & Herth, S. Magnetic tweezers for manipulation of magnetic particles in single cells. *Appl. Phys. Lett.* **104**, 063701 (2014).
6. Akbarzadeh, A., Samiei, M. & Davaran, S. Magnetic nanoparticles: preparation, physical properties, and applications in biomedicine. *Nanoscale Res. Lett.* **7**, 144 (2012).
7. Grancharov, S. G., Zeng, H., Sun, S., Wang, S., O'Brien, S. *et al.* Bio-functionalization of monodisperse magnetic nanoparticles and their use as biomolecular labels in a magnetic tunnel junction based sensor. *J. Phys. Chem. B* **109**, 13030–13035 (2005).
8. Lee, J., Isobe, T. & Senna, M. Preparation of ultrafine Fe3O4 particles by precipitation in the presence of PVA at high pH. *J. Colloid Interface Sci.* **177**, 490–494 (1996).
9. Arruebo, M., Galan, M., Navascues, N., Tellez, C., Marquina, C. *et al.* Development of magnetic nanostructured silica-based materials as potential vectors for drug-delivery applications. *Chem. Mater.* **18**, 1911–1919 (2006).
10. Peng, X., Schlamp, M. C., Kadavanich, A. V. & Alivisatos, A. P. Epitaxial growth of highly luminescent CdSe/CdS core/shell nanocrystals with photostability and electronic accessibility. *J. Am. Chem. Soc.* **119**, 7019–7029 (1997).
11. Rockenberger, J., Scher, E. C. & Alivisatos, A. P. A New nonhydrolytic single-precursor approach to surfactant-capped nanocrystals of transition metal oxides. *J. Am. Chem. Soc.* **121**, 11595–11596 (1999).
12. Fortin, J.-P., Wilhelm, C., Servais, J., Menager C., Bacri J. C. *et al.* Size-sorted anionic iron oxide nanomagnets as colloidal mediators for magnetic hyperthermia. *J. Am. Chem. Soc.* **129**, 2628–2635 (2007).
13. Tromsdorf, U. I., Bruns, O. T., Salmen, S. C., Beisiegel, U. & Weller, H. A highly effective, nontoxic T1 MR contrast agent based on ultrasmall PEGylated iron oxide nanoparticles. *Nano Lett.* **9**, 4434–4440 (2009).

14. Borges, M., Yu, S., Laromaine, A., Roig, A., Suarez-Garcia, S. *et al.* Dual T1/T2 MRI contrast agent based on hybrid SPION@coordination polymer nanoparticles. *RSC Adv.* **5**, 86779–86783 (2015).

15. Issadore, D., Park, Y. I., Shao, H., Min, C., Lee, K. *et al.* Magnetic sensing technology for molecular analyses. *Lab. Chip* **14**, 2385 (2014).

16. Lee, H., Shin, T.-H., Cheon, J. & Weissleder, R. Recent developments in magnetic diagnostic systems. *Chem. Rev.* **115**, 10690–10724 (2015).

17. Sun, E. Y., Josephson, L., Kelly, K. A. & Weissleder, R. Development of nanoparticle libraries for biosensing. *Bioconjug. Chem.* **17**, 109–113 (2006).

18. Sletten, E. M. & Bertozzi, C. R. Bioorthogonal chemistry: fishing for selectivity in a sea of functionality. *Angew. Chem. Int. Ed Engl.* **48**, 6974–6998 (2009).

19. Sletten, E. M. & Bertozzi, C. R. From mechanism to mouse: A tale of two bioorthogonal reactions. *Acc. Chem. Res.* **44**, 666–676 (2011).

20. Miller, B. T., Collins, T. J., Rogers, M. E. & Kurosky, A peptide biotinylation with amine-reactive esters: differential side chain reactivity. *Peptides* **18**, 1585–1595 (1997).

21. Yao, L. & Xu, S. Force-induced selective dissociation of noncovalent antibody–antigen bonds. *J. Phys. Chem. B* **116**, 9944–9948 (2012).

22. Peterson, V. M., Castro, C. M., Lee, H. & Weissleder, R. Orthogonal amplification of nanoparticles for improved diagnostic sensing. *ACS Nano* **6**, 3506–3513 (2012).

23. Liong, M., Tassa, C., Shaw, S. Y., Lee, H. & Weissleder, R. Multiplexed magnetic labeling amplification using oligonucleotide hybridization. *Adv. Mater. Deerfield Beach Fla* **23**, H254–H257 (2011).

24. Smith, C. Striving for purity: advances in protein purification. *Nat. Methods* **2**, 71–77 (2005).

25. Xu, C., Xu, K., Gu, H., Zhong, X., Guo, Z. *et al.* Nitrilotriacetic acid-modified magnetic nanoparticles as a general agent to bind histidine-tagged proteins. *J. Am. Chem. Soc.* **126**, 3392–3393 (2004).

26. Lund, A., Hellemann, A. L. & Vartdal, F. Rapid isolation of K88+ Escherichia coli by using immunomagnetic particles. *J. Clin. Microbiol.* **26**, 2572–2575 (1988).

27. Hornes, E., Wasteson, Y. & Olsvik, O. Detection of Escherichia coli heat-stable enterotoxin genes in pig stool specimens by an immobilized, colorimetric, nested polymerase chain reaction. *J. Clin. Microbiol.* **29**, 2375–2379 (1991).

28. Pamme, N. & Wilhelm, C. Continuous sorting of magnetic cells via on-chip free-flow magnetophoresis. *Lab. Chip* **6**, 974–980 (2006).

29. Sista, R. S., Eckhardt, A. E., Srinivasan, V., Pollack, M. G., Palanki, S. *et al.* Heterogeneous immunoassays using magnetic beads on a digital microfluidic platform. *Lab. Chip* **8**, 2188–2196 (2008).

30. Yoo, J.-W. Toward improved selectivity of targeted delivery: the potential of magnetic nanoparticles. *Arch. Pharm. Res.* **35**, 1–2 (2012).

31. Colombo, M., Carregal-Romero, S., Casula, M. F., Gutierrez, L., Morales, M. P. *et al.* Biological applications of magnetic nanoparticles. *Chem. Soc. Rev.* **41**, 4306 (2012).

32. Gossuin, Y., Roch, A., Muller, R. N. & Gillis, P. An evaluation of the contributions of diffusion and exchange in relaxation enhancement by MRI contrast agents. *J. Magn. Reson.* **158**, 36–42 (2002).

33. Geraldes, C. F. G. C. & Laurent, S. Classification and basic properties of contrast agents for magnetic resonance imaging. *Contrast Media Mol. Imaging* **4**, 1–23 (2009).

34. Busquets, M. A., Estelrich, J. & Sánchez-Martín, M. J. Nanoparticles in magnetic resonance imaging: from simple to dual contrast agents. *Int. J. Nanomedicine* 1727 (2015).

35. Na, H. B., Song, I. C. & Hyeon, T. Inorganic nanoparticles for MRI contrast agents. *Adv. Mater.* **21**, 2133–2148 (2009).

36. Lam, T., Pouliot, P., Avti, P. K., Lesage, F. & Kakkar, A. K. Superparamagnetic iron oxide based nanoprobes for imaging and theranostics. *Adv. Colloid Interface Sci.* **199–200**, 95–113 (2013).

37. Laurent, S., Elst, L. V., Roch, A. & Muller, R. N. Structure, synthesis and characterization of contrast agents for magnetic resonance molecular imaging in NMR-MRI, μSR and Mössbauer spectroscopies in molecular magnets (eds. Carretta, P. & Lascialfari, A.) 71–87 (Springer Milan, 2007).

38. Chen, T.-J., Cheng, T. H., Chen, C. Y., Hsu, S. C., Cheng T. L. *et al.* Targeted Herceptin–dextran iron oxide nanoparticles for noninvasive imaging of HER2/neu receptors using MRI. *JBIC J. Biol. Inorg. Chem.* **14**, 253 (2008).

39. Choi, H. S., Liu, W., Misra, P., Tanaka, E., Zimmer, J. P. *et al.* Renal clearance of quantum dots. *Nat. Biotechnol.* **25**, 1165–1170 (2007).

40. Chomoucka, J., Drbohlavova, J., Huska, D., Adam, V., Kizek, R. *et al.* Magnetic nanoparticles and targeted drug delivering. *Pharmacol. Res.* **62**, 144–149 (2010).

41. Choi, H. S., Liu, W., Liu, F., Nasr, K., Misra, P. *et al.* Design considerations for tumour-targeted nanoparticles. *Nat. Nanotechnol.* **5**, 42–47 (2010).

42. Nacev, A., Beni, C., Bruno, O. & Shapiro, B. The behaviors of ferro-magnetic nano-particles in and around blood vessels under applied magnetic fields. *J. Magn. Magn. Mater.* **323**, 651–668 (2011).

43. Kresse, M., Wagner, S., Pfefferer, D., Lawaczeck, R., Elste, V. *et al.* Targeting of ultrasmall superparamagnetic iron oxide (USPIO) particles to tumor cells in vivo by using transferrin receptor pathways. *Magn. Reson. Med.* **40**, 236–242 (1998).

44. Berry, C. C. & Curtis, A. S. G. Functionalisation of magnetic nanoparticles for applications in biomedicine. *J. Phys. Appl. Phys.* **36**, R198–R206 (2003).

45. Farokhzad, O. C., Jon, S., Khademhosseini, A., Tran, T. N., Lavan, D. A. *et al.* Nanoparticle-aptamer bioconjugates: a new approach for targeting prostate cancer cells. *Cancer Res.* **64**, 7668–7672 (2004).

46. Herr, J. K., Smith, J. E., Medley, C. D., Shangguan, D. & Tan, W. Aptamer-conjugated nanoparticles for selective collection and detection of cancer cells. *Anal. Chem.* **78**, 2918–2924 (2006).

47. Weissleder, R., Kelly, K., Sun, E. Y., Shtatland, T. & Josephson, L. Cell-specific targeting of nanoparticles by multivalent attachment of small molecules. *Nat. Biotechnol.* **23**, 1418–1423 (2005).

48. Neuberger, T., Schöpf, B., Hofmann, H., Hofmann, M. & von Rechenberg, B. Superparamagnetic nanoparticles for biomedical applications: possibilities and limitations of a new drug delivery system. *J. Magn. Magn. Mater.* **293**, 483–496 (2005).

49. van der Heijden, T., van Noort, J., van Leest, H., Kanaar, R., Wyman, C. *et al.* Torque-limited RecA polymerization on dsDNA. *Nucleic Acids Res.* **33**, 2099–2105 (2005).

50. Taneja, B., Schnurr, B., Slesarev, A., Marko, J. F. & Mondragón, A Topoisomerase V relaxes supercoiled DNA by a constrained swiveling mechanism. *Proc. Natl. Acad. Sci. U. S. A.* **104**, 14670–14675 (2007).

51. Lia, G., Semsey, S., Lewis, D., Adhya, S., Bensimon, D. *et al.* The antiparallel loops in gal DNA. *Nucleic Acids Res.* **36**, 4204–4210 (2008).

52. De Vlaminck, I. & Dekker, C. Recent advances in magnetic tweezers. *Annu. Rev. Biophys.* **41**, 453–472 (2012).

53. Lipfert, J., Hao, X. & Dekker, N. H. Quantitative modeling and optimization of magnetic tweezers. *Biophys. J.* **96**, 5040–5049 (2009).

54. Zacchia, N. A. & Valentine, M. T. Design and optimization of arrays of neodymium iron boron-based magnets for magnetic tweezers applications. *Rev. Sci. Instrum.* **86**, 053704 (2015).

55. Gosse, C. & Croquette, V. Magnetic tweezers: micromanipulation and force measurement at the molecular level. *Biophys. J.* **82**, 3314–3329 (2002).

56. Bijamov, A., Shubitidze, F., Oliver, P. M. & Vezenov, D. V. Quantitative modeling of forces in electromagnetic tweezers. *J. Appl. Phys.* **108**, 104701 (2010).

57. Brown, L. G. A survey of image registration techniques. *ACM Comput. Surv.* **24**, 325–376 (1992).

58. Gelles, J., Schnapp, B. J. & Sheetz, M. P. Tracking kinesin-driven movements with nanometre-scale precision. *Nature* **331**, 450–453 (1988).

59. Ovryn, B. & Izen, S. H. Imaging of transparent spheres through a planar interface using a high-numerical-aperture optical microscope. *JOSA A* **17**, 1202–1213 (2000).

60. Kim, K. & Saleh, O. A. Stabilizing method for reflection interference contrast microscopy. *Appl. Opt.* **47**, 2070–2075 (2008).

61. Kim, K. & Saleh, O. A. A high-resolution magnetic tweezer for single-molecule measurements. *Nucleic Acids Res.* **37**, e136 (2009).

62. Berg-Sørensen, K. & Flyvbjerg, H. Berg-Sorensen, K. & Flyvbjerg, H. Power spectrum analysis for optical tweezers. Rev. Sci. Instrum. 75, 594-612. *Rev. Sci. Instrum.* **75**, 594–612 (2004).

63. Ribeck, N. & Saleh, O. A. Multiplexed single-molecule measurements with magnetic tweezers. *Rev. Sci. Instrum.* **79**, 094301 (2008).

64. Adhikari, A. S., Chai, J. & Dunn, A. R. Mechanical load induces a 100-fold increase in the rate of collagen proteolysis by MMP-1. *J. Am. Chem. Soc.* **133**, 1686–1689 (2011).

65. Camp, R. J., Liles, M., Beale, John., Saeidi, N., Flynn, B. P. *et al.* Molecular mechanochemistry: low force switch slows enzymatic cleavage of human type I collagen monomer. *J. Am. Chem. Soc.* **133**, 4073–4078 (2011).

66. Monson, C. F., Driscoll, L. N., Bennion, E., Miller, C. J. & Majda, M. Antibody-antigen exchange equilibria in a field of an external force: design of reagentless biosensors. *Anal. Chem.* **81**, 7510–7514 (2009).

67. Holthausen, J. T., van Loenhout, M. T. J., Sanchez, H., Ristic, D., van Rossum-Fikkert, S. E. *et al.* Effect of the BRCA2 CTRD domain on RAD51 filaments analyzed by an ensemble of single molecule techniques. *Nucleic Acids Res.* **39**, 6558–6567 (2011).

68. Ramanathan, S. P., van Aelst, K., Sears, A., Peakman, L. J., Diffin, F. M. *et al.* Type III restriction enzymes communicate in 1D without looping between their target sites. *Proc. Natl. Acad. Sci. U. S. A.* **106**, 1748–1753 (2009).

69. Crut, A., Koster, D. A., Seidel, R., Wiggins, C. H. & Dekker, N. H. Fast dynamics of supercoiled DNA revealed by single-molecule experiments. *Proc. Natl. Acad. Sci. U. S. A.* **104**, 11957–11962 (2007).

70. Shroff, H., Reinhard, B. M., Siu, M., Agarwal, H., Spakowitz, A. & Linphardt J. Biocompatible force sensor with optical readout and dimensions of 6 nm3. *Nano Lett.* **5**, 1509–1514 (2005).

71. Hugel, T., Michaelis, J., Hetherington, C. L., Jardine, P. J., Grimes, S. *et al.* Experimental test of connector rotation during DNA packaging into bacteriophage φ29 capsids. *PLOS Biol.* **5**, e59 (2007).

72. Spiegel, P. C., Ermolenko, D. N. & Noller, H. F. Elongation factor G stabilizes the hybrid-state conformation of the 70S ribosome. *RNA N. Y. N* **13**, 1473–1482 (2007).

73. Woolstenhulme, C. J., Guydosh, N. R., Green, R. & Buskirk, A. R. High-precision analysis of translational pausing by ribosome profiling in bacteria lacking EFP. *Cell Rep.* **11**, 13–21 (2015).

74. Yao, L. & Xu, S. Force-induced remnant magnetization spectroscopy for specific magnetic imaging of molecules. *Angew. Chem. Int. Ed.* **50**, 4407–4409 (2011).

75. Yin, H., Xu, S. & Wang, Y. Dual DNA rulers reveal an 'mRNA looping' intermediate state during ribosome translocation. *RNA Biol.* **15**, 1392–1398 (2018).

76. Yao, L. & Xu, S. Long-range, high-resolution magnetic imaging of nanoparticles. *Angew. Chem. Int. Ed.* **48**, 5679–5682 (2009).

77. Budker, D. & Romalis, M. Optical magnetometry. *Nat. Phys.* **3**, 227–234 (2007).

78. Yao, L., Li, Y., Tsai, T.-W., Xu, S. & Wang, Y. Noninvasive measurement of the mechanical force generated by motor protein EF-G during ribosome translocation. *Angew Chem. Int. Ed.* **52**, 14041-14044 (2013).

79. Tsai, T.-W., Yang, H., Yin, H., Xu, S. & Wang, Y. High-efficiency "–1" and "–2" ribosomal frameshiftings revealed by force spectroscopy. *ACS Chem. Biol.* **12**, 1629–1635 (2017).

80. Pannetier, M., Fermon, C., Le Goff, G., Simola, J. & Kerr, E. Femtotesla magnetic field measurement with magnetoresistive sensors. *Science* **304**, 1648–1650 (2004).

81. Chemla, Y. R., Grossman, H. L., Poon, Y., McDermott, R., Stevens, R. *et al.* Ultrasensitive magnetic biosensor for homogeneous immunoassay. *Proc. Natl. Acad. Sci. U. S. A.* **97**, 14268–14272 (2000).

82. Gleich, B. & Weizenecker, J. Tomographic imaging using the nonlinear response of magnetic particles. *Nature* **435**, 1214–1217 (2005).

83. Maze, J. R., Stanwix, P. L., Hodges, S., Hong, J. M., Taylor, P. C. *et al.* Nanoscale magnetic sensing with an individual electronic spin in diamond. *Nature* **455**, 644–647 (2008).

84. Yao, L., Jamison, A. C. & Xu, S. Scanning imaging of magnetic nanoparticles for quantitative molecular imaging. *Angew. Chem. Int. Ed.* **49**, 7493–7496 (2010).

85. Grossman, H. L., Myers, W. R., Vreeland, V. J., Bruehl, R., Alper, M. D. *et al.* Detection of bacteria in suspension by using a superconducting quantum interference device. *Proc. Natl. Acad. Sci.* **101**, 129–134 (2004).

86. Bartel, D. P. MicroRNAs: genomics, biogenesis, mechanism, and function. *Cell* **116**, 281–297 (2004).

87. Alvarez-Garcia, I. & Miska, E. A. MicroRNA functions in animal development and human disease. *Dev. Camb. Engl.* **132**, 4653–4662 (2005).

88. Lee, Y. S. & Dutta, A. MicroRNAs in cancer. *Annu. Rev. Pathol.* **4**, 199–227 (2009).

89. Lagos-Quintana, M., Rauhut, R., Lendeckel, W. & Tuschl, T. Identification of novel genes coding for small expressed RNAs. *Science* **294**, 853–858 (2001).

90. Benes, V. & Castoldi, M. Expression profiling of microRNA using real-time quantitative PCR, how to use it and what is available. *Methods San Diego Calif* **50**, 244–249 (2010).

91. Obernosterer, G., Martinez, J. & Alenius, M. Locked nucleic acid-based in situ detection of microRNAs in mouse tissue sections. *Nat. Protoc.* **2**, 1508–1514 (2007).

92. Sudo, H., Mizoguchi, A., Kawauchi, J., Akiyama, H. & Takizawa, S. Use of non-amplified RNA samples for microarray analysis of gene expression. *PLOS ONE* **7**, e31397 (2012).

93. Yao, L., Wang, Y. & Xu, S. Label-free microRNA detection based on exchange-induced remnant magnetization. *Chem. Commun.* **49**, 5183 (2013).

Chapter 2 High-Efficiency "-1" and "-2" Ribosomal Frameshiftings Revealed by Force Spectroscopy

2.1 Introduction

Frameshifting is a process in which the ribosome decodes mRNA in an alternative grouping of consecutive nucleotide triplets.[1] Random frameshiftings are translational errors that often encounter stop codons shortly afterward, whereas programmed frameshiftings decode overlapping genes and regulate both mRNA stabilities and protein expression levels.[2] Despite the varying motifs for "-1" and "+1" frameshiftings, cis-acting mRNA elements generally induce this process in the thermodynamically favored direction.[2,3] Frameshifting is mostly studied in viral mRNAs for its association with infectiousness, although it occurs in both prokaryotic and eukaryotic cellular mRNAs. The putative "-1" frameshifting motif includes a slippery sequence in the form of "X XXY YYZ" (the blanks define the "0" reading frame), a downstream secondary structure, and a spacer between the two elements; less often upstream Shine−Dalgarno (SD) sequences can replace the downstream secondary structures.[4] However, bioinformatics analysis identified frameshifted open reading frames (ORFs) that were not associated with proximal secondary structures.[5,6] These ORFs were attributed to transcriptional slippage[7,8] or a trans-acting protein factor.[9] Similar motifs were also identified in bacteria.[4] However, frameshiftings without mRNA secondary structures are rarely experimentally studied.

The single nucleotide (nt) difference between the three reading frames makes it difficult to directly and precisely resolve them. The conventional dual luciferase assay

measures the ratio of the proteins translated in the "0" and "−1" reading frames inside the cell.[10] It cannot rule out the roles of transcription slippage and trans-acting factors as mentioned above.[5,8] In addition, dual luciferase assay or mass spectrometry cannot distinguish different frameshifting pathways, such as multiple frameshifting steps and sizes that lead to the same peptides.[11] Recently, single molecule and fast kinetic fluorescence signals have been tracked to deduce the ribosome reading frame, but the actual ribosome position was not directly probed.[12,13] Optical trap cannot identify the frameshifting positions because of the intrinsic ribosome fluctuation on the slippery site.[11] The toe-printing assay usually exhibits multiple-bands even for homologous ribosome complexes,[14] making it difficult to quantify mixtures of frameshifting products unless a single frameshifting product dominates.[15,16]

Here, we report a new assay of using systematically designed DNA probes labeled with magnetic beads to precisely reveal the ribosome positions on mRNA with single nt resolution. This assay consists of force-induced remnant magnetization spectroscopy (FIRMS) that we invented and two novel probing schemes that are first reported here. The position of the ribosome was determined by precisely identifying the mRNA nucleotides adjacent to the ribosome entry site, which is 11-13 nucleotides away from the first nucleotide of P-site codon.[17–19] The FIRMS measures the dissociation forces of nucleic acid duplexes formed with the mRNA and DNA probes with high resolution. Using this assay, we tracked three consecutive translocation steps to unambiguously identify nine possible ribosome positions on the mRNA under in vitro conditions. High-yield ribosomal "-1" and "-2" frameshiftings were revealed on a short slippery mRNA without a secondary

structure, which was confirmed by the conventional toe- printing assay and in vitro mRNA-translations. Mechanistic studies were carried out by modifying the mRNA motif, introducing a secondary structure, and varying other experimental conditions.

2.2 Experimental section

2.2.1 Materials

All of the mRNAs and DNA probes are purchased from IDTDNA (Integrated DNA Technologies). The sequence of the mRNA containing the GA_7G motif was 5′-Bio-C AAC UGU UAA UUA AAU UAA AUU AAA AAG GAA AUA AAA AUG UUU GAA AAA AAG UAC GUA AAU CUA CUG CUG AAC UC-3′; the mRNAs containing the GGA_6G and the GA_3GUA_2 (NS) motifs were the same as above except the replacements of GGA AAA AAG and GAA AGU AAG at the slippery sites, respectively; and the mRNA containing the dnaX stem loop was: 5′-Bio-GU UAA UUA AAU UAA AUU AAA AAG GAA AUA AAA AUG UUU GAA AAA AAG UAC GUA CCG GCA GCC GCU ACC CGC GGC GGC CGG UUG GUC UAC G-3′. The slippery motifs and the stem loop structure are underlined. Bio: biotin functionalized.

Table 2.1 The sequences of the probing DNAs

P15a: 3′-**G CAT TTAGAT GAC GA**G AAC TC/TEGBio/-5′
P14: 3′-**CAT TTAGAT GAC GA**G AAC TC/TEGBio/-5′
P13: 3′-**AT TTAGAT GAC GA**G AAC TC/TEGBio/-5′
P12: 3′-**T TTAGAT GAC GA**G AAC TC/TEGBio/-5′
P18: 3′-**C ATG CAT TTAGAT GAC GA**G AAC TC/TEGBio/-5′
P15b: 3′-**T TTAGAT GAC GAC TT**C TCGAA/TEGBio/-5′
P15c: 3′-**A GAT GAC GAC TTG AG**G AAC TC/TEGBio/-5′
SLP15a: 3′-**GCA TGG CCG TCG GCG** TAC CCG/TEGBio/-5′
SLP15b: 3′-**CCG TCG GCG ATG GGC**/TEGBio/-5′

The bases in bold are complementary bases with the mRNA. TEG: linker molecule (Integrated DNA Technologies). The probes were designed so that the ribosome complexes always formed 12-15 duplexes with the probes for optimal force resolution.

2.2.2 Sample preparation

All of the mixtures are in TAM_{10} buffer: 20 mM Tris-HCl (pH 7.5), 30 mM NH_4Cl, 70 mM KCl, 5 mM EDTA, and 7 mM BME (2-mercaptoethanol). Five mixtures were prepared: 200 mL ribosome mix, 400 mL TuWG mix, 400 mL Tu0G mix, 400 mL A mix, and 400 mL A-Lys mix. The details are as follows. The ribosome mix contained 1 μM ribosome, 1.5 μM of IF1, 2, 3, 2 μM of mRNA, 4 μM of charged fMet-$tRNA^{fMet}$, and 4 mM of GTP. The TuWG mix contained 6 μM EF-Tu, 3 μM EF-G, 4 mM GTP, 4 mM PEP, and 0.02 mg/ml pyruvate kinase (catalyzes the transfer of a phosphate group from phosphoenolpyruvate to adenosine diphosphate). The Tu0G mix contained no EF-G but all the rest components in TuWG. The A mix contained 100 mM Tris (pH 7.8), 20 mM $MgAc_2$, 1 mM EDTA, 4 mM ATP, 0.1 mg/ml total synthetase, 50 A_{260}/ml total tRNA, and 0.25 mM of phenylalanine, glutamic acid. The A-Lys mix contained 100 mM Tris (pH 7.8), 20

mM $MgAc_2$, 1 mM EDTA, 4 mM ATP, 0.1 mg/ml total synthetase, 2 A_{260}/ml $tRNA^{Lys}$, and 0.25 mM of lysine.

The five mixes were incubated at 37 ºC for 25 min. The ribosome, TuWG and A mixes were mixed with 1:2:2 ratio and then incubated at 37 ºC for 15 min. The resulting ribosome complex was added on 1.1 M sucrose cushion and purified by ultra-centrifuge. The concentration of ribosome was determined using A260 measurements. The ribosome complex was then incubated with the A- Lys and Tu0G mixes at 37 ºC for 2 min to form Pre_1. The resulting Pre_1 was then added on 1.1 M sucrose cushion and purified by ultra-centrifuge.

The $Post_1$ ribosome complex was formed by incubating Pre_1 (1 μM), 2 μM EF-G, 4 mM GTP, 4 mM PEP, and 0.02 mg/ml pyruvate kinase at 37 ºC for 30 min. The resulting $Post_1$ was added on 1.1 M sucrose cushion and purified by ultra-centrifuge.

The $Post_2$ ribosome complex was formed by incubating $Post_1$ (1 μM) with A-Lys and TuWG mixes in the ratio of 1:2:2 at 37 ºC for 30 min. The resulting $Post_2$ was added on 1.1 M sucrose cushion and purified by ultra-centrifuge.

To prepare $Post_3$ ribosome complex, three different tRNA solutions were prepared: A-Tyr, A-Val, and A-Ser. All three solutions contained 100 mM Tris (pH 7.8), 20 mM $MgAc_2$, 1 mM EDTA, 4 mM ATP, 0.1 mg/ml total synthetase, 50 A_{260}/ml total tRNA, and 0.25 mM each of phenylalanine, glutamic acid, and lysine. The A-Tyr, A-Val, and A-ser also contained 0.25 mM tyrosine, valine and serine, respectively. Each one of these tRNA solutions was incubated with the ribosome mix and TuWG mix in the ratio of 2:1:2, and

incubated at 37 ºC for 30 min. The resulting $Post_3$ complexes were purified by 1.1M sucrose cushion.

The Pre_NS_1 and Post_NS_1 ribosome complexes were prepared similarly as Pre_1 and $Post_1$, except the A-Lys mix is replaced by A-Ser mix to incorporate serine instead of lysine at the non-slippery codon. The resulting ribosome complexes were purified via 1.1M sucrose cushion.

The Post_CGC_{1-2} ribosome complexes were prepared in one step from the initiation complex in the presence of phenylalanine, glutamic acid, lysine, and without and with arginine for Post_CGC_1 and Post_CGC_2, respectively. The resulting ribosome complexes were purified via 1.1M sucrose cushion.

The Post_GGA_1 and Post_SLP_1 ribosome complexes were prepared similarly as $Post_1$, which were generated by translocation of their corresponding Pre_1 complexes. The resulting ribosome complexes were purified via 1.1M sucrose cushion.

The Post_GGA_{2-3} and Post_SLP_3 ribosome complexes were prepared in one pot from the initiation complex. But they were stopped at the corresponding codons. One tRNA solution was prepared containing: 100 mM Tris (pH 7.8), 20 mM $MgAc_2$, 1 mM EDTA, 4 mM ATP, 0.1 mg/ml total synthetase, 50 A_{260}/ml total tRNA, and 0.25 mM each of phenylalanine, glutamic acid (or glycine), lysine, and tyrosine or valine. The tRNA solution was incubated with the ribosome mix and TuWG mix in the ratio of 2:1:2, and incubated at 37 ºC for 30 min. The resulting Post-complexes were purified by 1.1M sucrose cushion.

2.2.3 FIRMS measurements

The surface area of the sample well was 2×6 mm^2, coated with biotin then incubated with streptavidin. The ribosome complexes were immobilized on the surface via the 5′-end biotin on the mRNA. The probing DNAs were incubated with streptavidin-coated magnetic beads (M280, Invitrogen). For each FIRMS experiment, the probing DNA labelled with a magnetic bead is hybridized to the 3' side of the ribosome-mRNA complex. Magnetic signal of the sample was measured by an atomic magnetometer as a function of mechanical force. The force was provided by a centrifuge (5417R from Eppendorf), with the speed increasing by 100 rpm (revolution per minute) per step. The dissociation of the DNA-mRNA duplexes was indicated by a decrease in the magnetic signal, which occurred when the centrifugal force reached the dissociation force of the duplex. This is because the dissociated magnetic beads were removed from the sample. The typical force range in this work was 82 pN, after which the residual magnetic signal was taken as the background. FIRMS profiles were obtained by normalizing the overall magnetic signal decrease (B_0) to be 100% and then plotting the relative magnetic signal decrease (B/B_0) vs. the external force. The force values were calculated according to $m\omega^2 r$, in which m is the buoyant mass of M280 magnetic beads (4.6×10^{-15} kg). ω is the centrifugal speed, and r is the distance of the magnetic beads from the rotor axis (8 cm for 5417R). The typical force resolution was 3-4 pN in this work. The samples were at room temperature during approximately 2-3 h total measuring time. Each profile reported in this work was repeated at least three times to assure reproducibility.

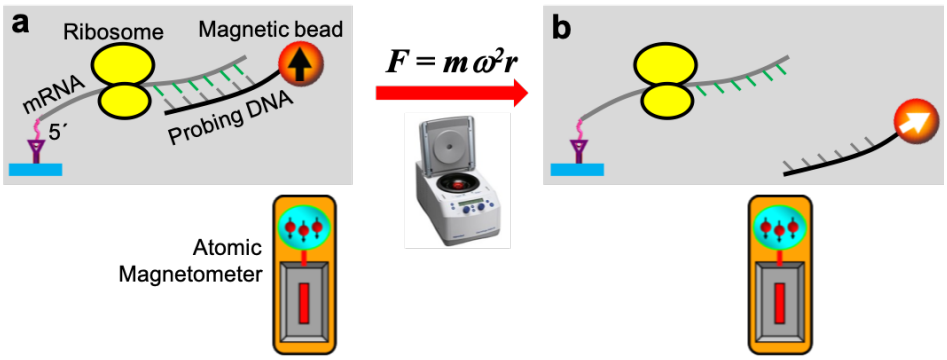

Figure 2.1 Scheme of the FIRMS method for probing frameshifting. (**a**) The ribosome complexes are immobilized on the streptavidin-coated surface via the 5′-end biotin on the mRNA. The probing DNAs are labelled with magnetic beads. The uncovered mRNA on the ribosome complexes forms duplexes of certain basepairs with the probing DNA. The number of bp of the duplex will thus reveal the position of the ribosome on the mRNA. The magnetic signal is measured by an atomic magnetometer. (**b)** A mechanical force is applied to the sample by using a centrifuge. The sample magnetic signal is measured again after applying the force. If the force reaches the dissociation force of the DNA-mRNA duplex, a sharp decrease in the magnetic signal will be observed, because the dissociated DNA will be removed from the sample.

2.2.4 Toe-printing assay

The mRNAs for toe-printings were transcribed and purified *in vitro* using the HiScribe T7 Quick High Yield RNA Synthesis Kit (NEB). The beginning codons were: "ATG-TTT-GAA-AAA-AAG" for GA_7G and SLP mRNAs , but the SLP mRNA contained the dnaX stem loop. The "AAA" codon was replaced with "AGT" in AGU mRNA. The ribosome complexes were prepared similarly as the $POST_3$ complexes, in the presence of only amino acids F, E, and K. For AGU mRNA, amino acid S was included in addition to the other amino acids. The 5'-terminal of the 20-nt-long primer was labeled with Cy5 dye (described in the following) and was 62-nt downstream from the first nucleotide of the "AAG" codon in the frameshifting motif. The ribosome complexes (10 pmol) were annealed with the primer (20 pmol) in 1_X reaction buffer of the AMV reverse transcriptase

from NEB under the following condition: (rt, 5min)-(37 ºC, 5 min)-(ice, 5 min). Then dNTP mixture (final concentration 0.5 mM), RNaseOUT (ThermoFisher, 60 units), DTT (final concentration 5 mM), and AMV reverse transcriptase (20 Units) were added. The mRNA extension reaction (total volume 20 μL) was continued under the following condition: (rt, 5 min)-(37 ºC, 30 min). The reverse transcriptase was deactivated by heating at 95 ºC for 10 min in the presence of 50 mM NaOH. Then the NaOH was neutralized with HCl, and the total volume was increased to 200 μL with 0.3M NaAc (pH 5.2). The solution was then extracted with equal volume phenol/chloroform, and precipitated with 100% ethanol. The pellets were collected by spin at 20 K x g at 4 ºC for 30 min, washed with 70% ethanol 2 times, and resuspended with 10μL loading solution. The cDNAs were separated on a 40 cm X 20 cm X 0.4 mm 15%-acrylamide gel contained 8 M of urea (40-45 W, 3-4 h). The Gels were immediately scanned on the Strom 860 scanner (Molecular Dynamics) under high sensitivity setting.

The unlabeled primer was ordered from IDTDNA. 0.6 nmol of the primer was mixed with T4 polynucleotide kinase and ATPγS according to the 5'-EndTag (Vector Laboratories) protocol. The reaction was continued at 37 ºC for 2 h. Then 50 μg of Cy5 Maleimide Mono-Reactive Dye (GE Healthcare) was dissolved in 5 μL of DMSO and was added in the primer reaction mix. The reaction was incubated at 30 ºC for 2-4 h, followed by the precipitation procedure of the manufacture's protocol. The labeled primer was resuspended with small amount of nuclease-free water and purified from free dye via a size-exclusive column with Sephadex G-25 fine medium (GE Healthcare).

2.2.5 Protein expressions

The construct II containing the sequence "ATG TTT GAA AAA AAG" + "CG" + "CTC-N_{84}-ACA-N_{15}-TTA-AAA-N_{15}-CAC-N_{15}-ACT-AAA-N_{45}-$(CAT)_6$-TAA" was ordered from IDTDNA and sub-cloned into the pet 20b(+) vector between the NdeI and XhoI sites (Stratagene). The constructs I and III were mutated from construct II via single and double nucleotides deletion at the variation segment, respectively (QuickChange Lightning kit from Agilent Technology). These plasmids were transformed into the BL21-star cells (LifeTechnologies) and cultured. The cells were induced by 0.1 mM IPTG for 1 h. Then 4x of the cell weight B-PER Complete protein extraction reagent (life technology) was added to lyse the cells. Then 10 ml of the clarified cell lysates were loaded on HisTrap HP 5 ml column (GE Healthcare Life Sciences). The His-tagged proteins were eluted via imidazole gradient and concentrated with Amicon Ultra filter (EMD Millipore). Typically, 500-1000 pmol of the 8.5 kDa protein was isolated (Figure 2.2). There was no significant yield difference comparing the different constructs, implying the frameshifting yield was high. However, the efficiencies could not be precisely determined because the proteins in the other reading frames were not detected on the gel.

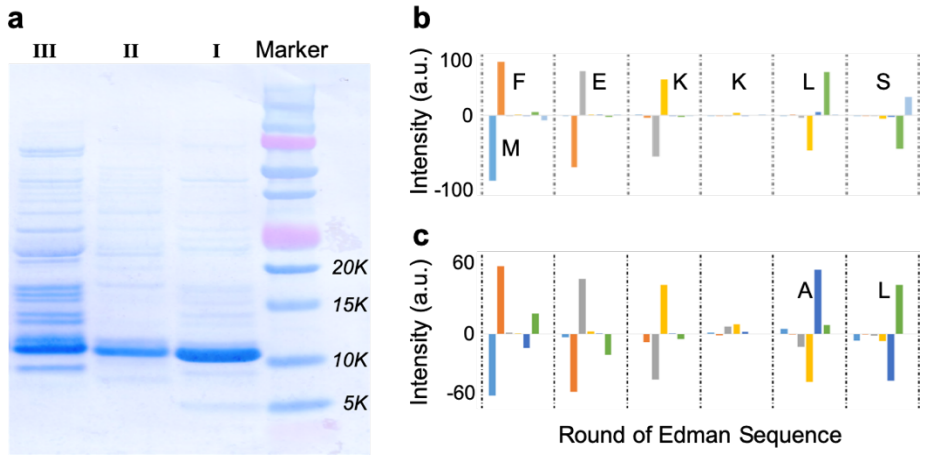

Figure 2.2 In cell translational frameshifting verified by sequencing. (**a**) The SDS-PAGE image of the recombinant proteins (all the expected sequences shown in Table 2.2). The8.5kDa proteins migrated near the 10 K marker. (**b**) Edman sequencing of the 8.5 kDa protein in construct I. (**c**) Edman sequencing of the 8.5 kDa protein in construct II. The signal is the differential value of the amino acid intensities of the current cycle minus the previous cycle; therefore， for the two consecutive lysine residues, the second signal was near zero.

To express the mCherry protein, the sequence with His_6 tag was ordered from IDTDNA and inserted in the "-2" reading frame after the slippery site to replace the codons in construct II. All the other operations were the same except the induction time was 6 h instead of 1 h. In vitro mRNA translation with PURExpress kit. The DNAs containing the sequence "T7 promoter" + "ATG TTT GAA AAA AAG" + "XX" + "mCherry" ("XX" are the variations in Table 2.2) were ordered from IDTDNA and transcribed into mRNA with the HiScribe T7 Quick High Yield RNA Synthesis Kit (NEB). The mRNAs were purified with PureLink RNA Mini Kit (Ambion). The qualities of the mRNAs were confirmed by RNA Gels and 5 μg of the mRNA were used for one protein synthesis reaction with the PURExpress in vitro Protein Synthesis Kit (NEB). The mCherry incubation solutions were directly read with the Spectra-Max M5 plate- reader, with excitation/emission wavelengths

at 584nm/612nm, respectively. Because the incubation conditions were exactly the same, the frameshifting efficiencies were compared directly from the fluorescence reading after subtracting with the background.

Table 2.2 Design of the recombinant protein constructs

	DNA Sequences			Protein Seuence	Frame-shifting	MW (kDa)
	5'-fragment	variation	3'-fragment			
I	ATG-TTT-GAA-AAA-AAG	--	CTC-N_{84}-ACA-N_{15}-TTA-AAA-N_{15}-CAC-N_{15}-ACT-AAA-N_{45}-$(CAT)_6$-TAA	MFEKK_LSDG	0	8.5
II		CG		MFEKKALSDG	-1	8.6
III		C_		MFEKKSLSDG	-2	8.6

a. "-" indicates null. b. Red sections indicates the His_6 tags in "-2", "-1", and "0" frame, respectively. c. The protein sequence refers to the peptide translated from the AUG codon at the beginning of the mRNA.

2.3 Results and discussion

2.3.1 Translocation probing strategies

Figure 2.3 displays the ribosome complexes studied in this work that tracked the ribosome movements over the slippery sequence "GAA AAA AAG" (GA_7G), from "AAA" at the A-site to "AAG" at the E- site. The overall displacement is 9 nt. The pretranslocation-complex-1 (Pre_1) carried $tRNA^{Glu}$ and MFEK-$tRNA^{Lys}$ at the peptidyl-tRNA-binding site

(P-site) and aminoacyl-tRNA- binding site (A-site), respectively. The mRNA sequence starting from the P-site to downstream was "GAA AAA AAG″. Then the EF-G·GTP complex was added to promote the first translocation step to form the post-translocation-complex-1 ($Post_1$), which potentially possesses all three reading frames, "0", "-1", and "-2" (denoted as $Post_1(0)$, $Post_1(-1)$ and $Post_1(-2)$, respectively). The second translocation step proceeded by adding EF-G·GTP and Lys-$tRNA^{Lys}$ ternary complex, to form $Post_2$ complexes that also potentially contained all three reading frames of $Post_2(0)$, $Post_2(-1)$ and $Post_2(-2)$. The $Post_3$ complexes were generated in one-pot from the ribosome initiation complex with EF-G·GTP, total tRNAs, and only the corresponding set of amino acids for each specific frame. In addition, $Post_3(0)$ was also prepared from $Post_2$ in the presence of the "0" frame substrate (Tyr-$tRNA^{Tyr}$ ternary complex) and EF-G·GTP.

Figure 2.3b,c shows two probing schemes using multiple magnetically labeled DNAs. For each scheme, FIRMS was used to determine the dissociation forces of the resulting DNA-mRNA duplexes by measuring the magnetic signal as a function of centrifugal force; the magnetic signal will show a decrease when the duplexes dissociate because of the removal of the associated magnetic beads (Figure 2.1). Specifically, in Figure 2.3b, three DNA oligomers were designed to have 3-nt shift in between, so that each one will probe one of the three translocation steps. In Figure 2.3c, to improve the precision of frameshifting assignments, a series of probing DNAs with1-nt difference in between and aligned at their 5′-termini were used to probe the same translocation. Therefore, the reading frames can be precisely determined from the DNA−mRNA binding patterns, and multiple frameshiftings can be unambiguously assigned.

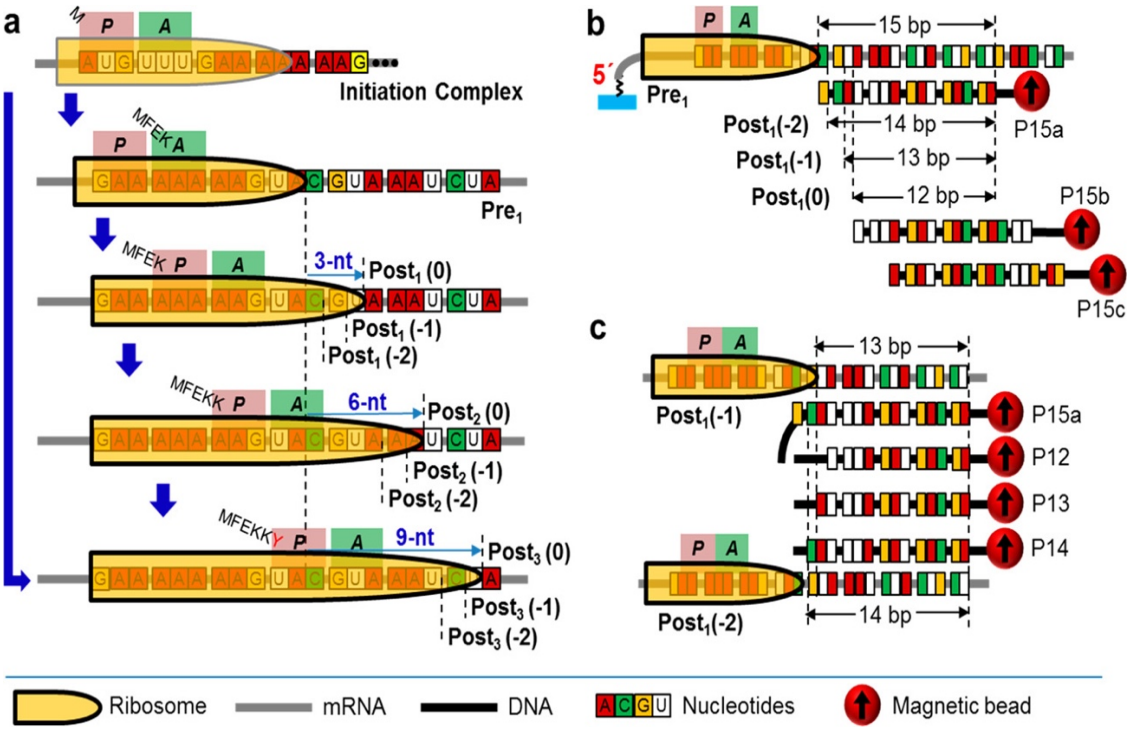

Figure 2.3 Schemes of the ribosome complexes and the FIRMS assay. **(a)** Ribosome complexes. Starting from the initiation complex, the pretranslocation complex was produced, followed by three consecutive steps of translocation going through the GA_7G motif. **(b)** The FIRMS scheme of using different magnetically labeled DNAs for probing different translocation step. In each step, the formation of 12-, 13-, and 14-bp DNA-mRNA duplexes indicate normal translocation, "-1" frameshifting, and "-2" frameshifting, respectively. **(c)** Scheme of using probe DNAs with a single nt difference to confirm the reading frame.

2.3.2 High-yield frameshiftings on the GA_7G motif

In the first translocation step, we observed 55% "-1" and 45% "-2" frameshiftings but no "0" frame translocation. This observation was confirmed with two probing schemes and extensive control sequences.

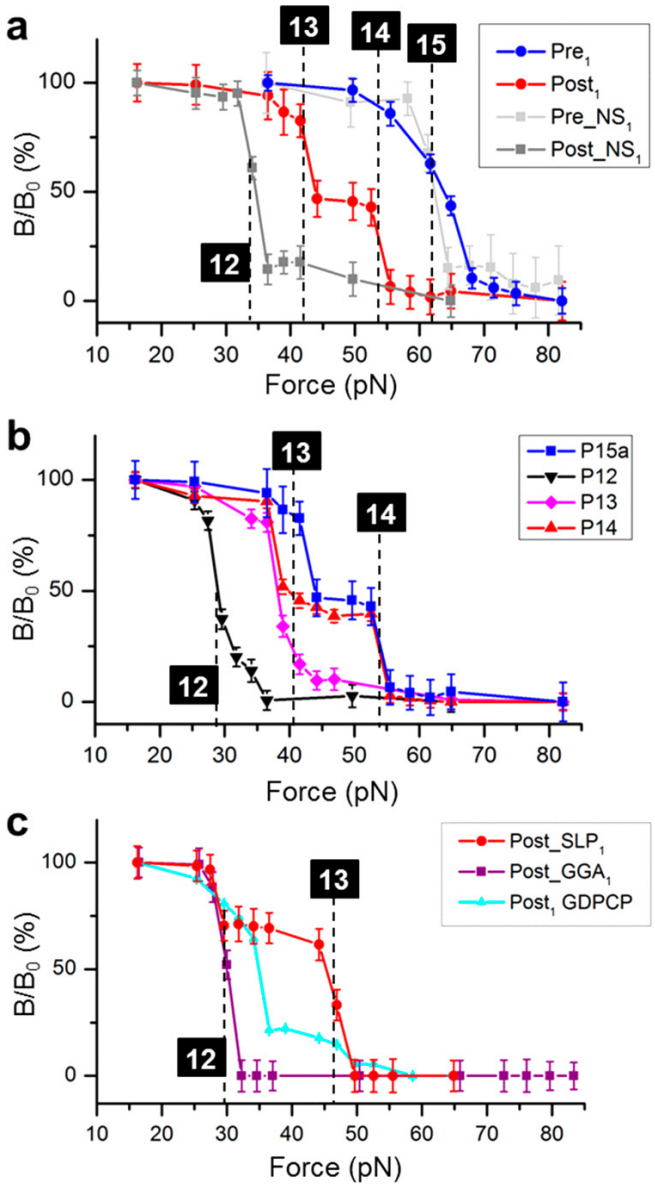

Figure 2.4 Probing the three reading frames of the first translocation step. **(a)** FIRMS profiles of Pre_1 and $Post_1$ for the GA_7G motif, in comparison with those for a nonslippery (NS) motif. **(b)** Confirmation of the "-1" and "-2" frameshiftings for GA_7G using a series of NDA probes. **(c)** FIRMS profiles for the stem loop (SLP), the GGA motifs, and GA_7G motif promoted by EF-G·GDPCP, showing different translocation behaviors.

Figure 2.4 shows the results of the first translocation step. The dissociation of the DNA−mRNA duplexes is indicated by a sharp decrease in the magnetic signal. A

calibration curve of dissociation force versus bp for a series of DNA−mRNA duplexes has been obtained (Figure 2.5). Using probe P15a, Pre_1 complex exhibited 15-bp binding force (Figure 2.4a, blue trace). $Post_1$ yielded two binding forces of 13- and 14-bp, respectively (Figure 2.4a, red trace). No 12-bp binding force was observed. This result indicates both "-1" and "-2" frameshiftings for the GA_7G motif but no normal translocation. When the slippery motif was replaced by a nonslippery (NS) "GAA AGU AAG", normal translocation occurred for its first translocation product, $Post\_NS_1$ (Figure 2.4a, dark gray trace). This was indicated by the binding force for 12-bp. For comparison, its pretranslocation complex, Pre_NS1, yielded binding force of 15-bp (Figure 2.4a, light gray trace).

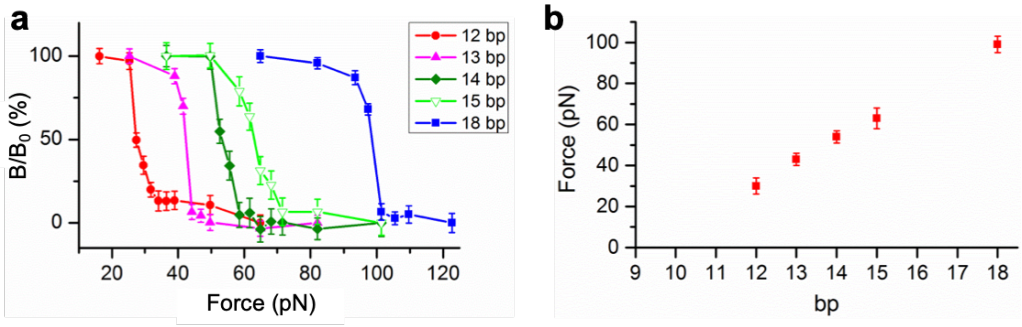

Figure 2.5 Force calibration for the DNA-mRNA duplexes. **(a)** FIRMS profiles of the various duplexes formed between the mRNA containing GA_7G and the probing DNAs that have different numbers of complementary bases to the mRNA. The magnetic signal was normalized to the overall magnetic field decrease B_0, which was the magnetic signal difference between the initial magnetic signal and the final magnetic signal at the maximum force in each case. B/B_0: relative magnetic signal; bp: basepair. (**b**) The correlation between the dissociation force and the number of bp. The plot shows that, on average, the dissociation force increases by approximately 11 pN per bp.

The unusual "-1" and "-2" frameshiftings of the GA_7G motif were confirmed in Figure 2.4b, using the probing scheme depicted in Figure 2.3c. The P12, P13, and P14

exhibited binding forces for $Post_1$ of 12-, 13-, and a combination of 13- and 14-bp, respectively. This indicated that the 13-bp DNA-mRNA duplex was limited by the ribosome front. The 13-/14-bp combination persisted when using P15a, but no 15-bp duplex appeared. This result again indicated that the ribosome front limited the duplexes to be 13 and 14 bps. Together, the two results conclusively determined the exact ribosome positions. Similarly, the exact ribosome front in Pre_1 was confirmed to form exactly 15-bp duplex with P15a and a longer DNA probe (Figure 2.6). Therefore, our assay unambiguously revealed that only Post1(-1) (∼55%) and Post1(-2) were present after the first round of translocation.

To elucidate the unusual frameshifting mechanism, three approaches were used (Figure 2.4c). The first experiment was to reveal the role of GTP. When EF-G·GTP was replaced by its nonhydrolyzable analogue, EF-G·GDPCP, which also promotes translocation,[20] mostly normal translocation occurred to produce $Post_1(0)$ of 32 pN binding force (cyan trace). The 12-bp complex was the major product, different from those in the EF-G·GTP experiments. These results indicate that GTP energy is indispensable to frameshifting.

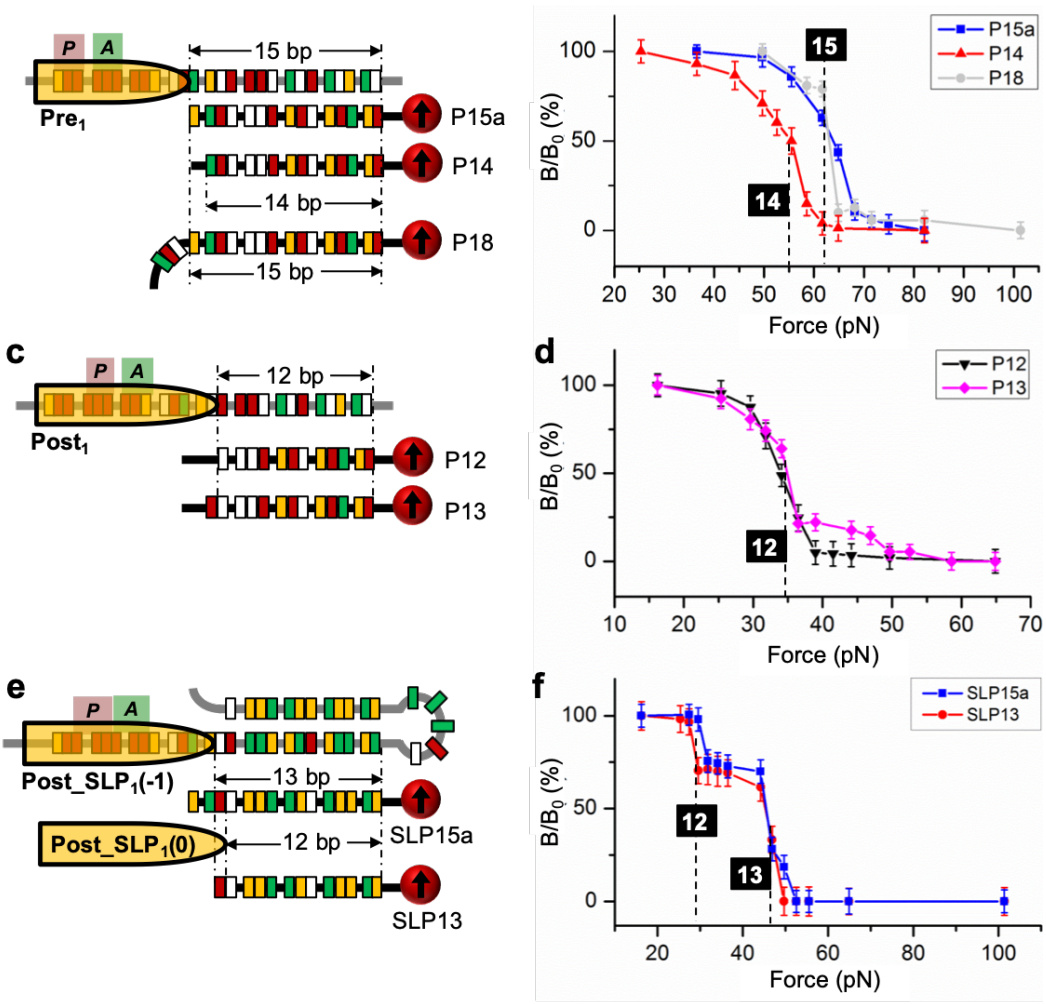

Figure 2.6 Use of multiple DNA probes to precisely determine the ribosome reading frame. **(a,b)** Scheme and results of using DNAs P14, P15a, and P18 to verify the position of ribosome in the Pre_1 complex. The dissociation force increase from P14 to P15a indicates the minimum of 15-bp duplexes formed between P15a and Pre_1. The constant dissociation force from P15a to P18 indicates the maximum of 15-bp duplexes. Therefore, the position of ribosome in Pre_1 is precisely determined to have 15 complementary bases with P15a. **(c,d)** Scheme and results of using P12 and P13 to verify the position of ribosome in the $Post_1$ complex promoted by EF- G•GDPCP. The overlap of the main feature for P13 and the feature for P12 indicates this dissociation force corresponds to 12-bp DNA-mRNA duplexes, confirming the main product to be the "0" reading frame. **(e,f)** Scheme and results of using SLP15a and SLP13 probes for the Post_SLP_1 complex. The overlapping profiles indicate the higher binding force belonged to the 13-bp duplexes. The lower binding force feature thus corresponds to the 12-bp duplex, i.e. the "0" reading frame in Post_SLP_1. Therefore, both Post_SLP1(-1) and Post_SLP1(0) were present, with the former being the main product at approximately 63%.

The second experiment was to change the slippery sequence. We modified the GA_7G sequence to GGA_6G (denoted as GGA for simplicity). The post complex (Post_GGA_1) formed only 12-bp duplexes with P15a, indicating only normal translocation (Figure 2.4c, purple trace). This result agrees with the literature,[12,21] showing the critical role of the P-site codon-anticodon interaction in stimulating frameshifting. It also means the SD-sequence was probably too far to play a significant role (13 nt away from AAA). Similarly, no significant frameshifting (less than ~10%, our current detection limit) was detected in the following two translocation steps to form Post_GGA_2 and Post_GGA_3 (Figure 2.7a,b). Even in the presence of the downstream aminoacyl tRNA of the "-1" reading frame, no Post_GGA_3(-1) was induced. This result is consistent with the literature that A AAA AAG needs a downstream secondary structure to cause frameshifting.[4,22] In addition, because the frameshifting has occurred on the GAA AAA sequence, we studied the mRNA that replaced the following AAG to CGC. As shown in Figure 2.7c,d, no frameshifting occurred for two translocation steps that led to Post_CGC_1 and Post_CGC_2. This result suggests that GAA AAA alone is insufficient to induce the frameshifting. Again, this result agrees with the literature.[4]

The third experiment was to determine the frameshifting with the authentic dnaX stem loop structure.[22] The post complex (Post_SLP) formed both 12- and 13-bp duplexes with SLP15a, respectively (Figure 2.4c, red trace). The assignments were confirmed using the scheme in Figure 2.3c (Figure 2.6). The "-2" frameshifting was absent. Instead, Post_SLP_1(-1) was the major product at 63 ± 12%, and the remaining was Post_SLP_1(0). This result agrees with the literature that showed approximately 70% frameshifting

efficiency.[12,21,22] The Post_SLP$_3$ was studied, and the frameshifting yield was preserved (Figure 2.74e,f).

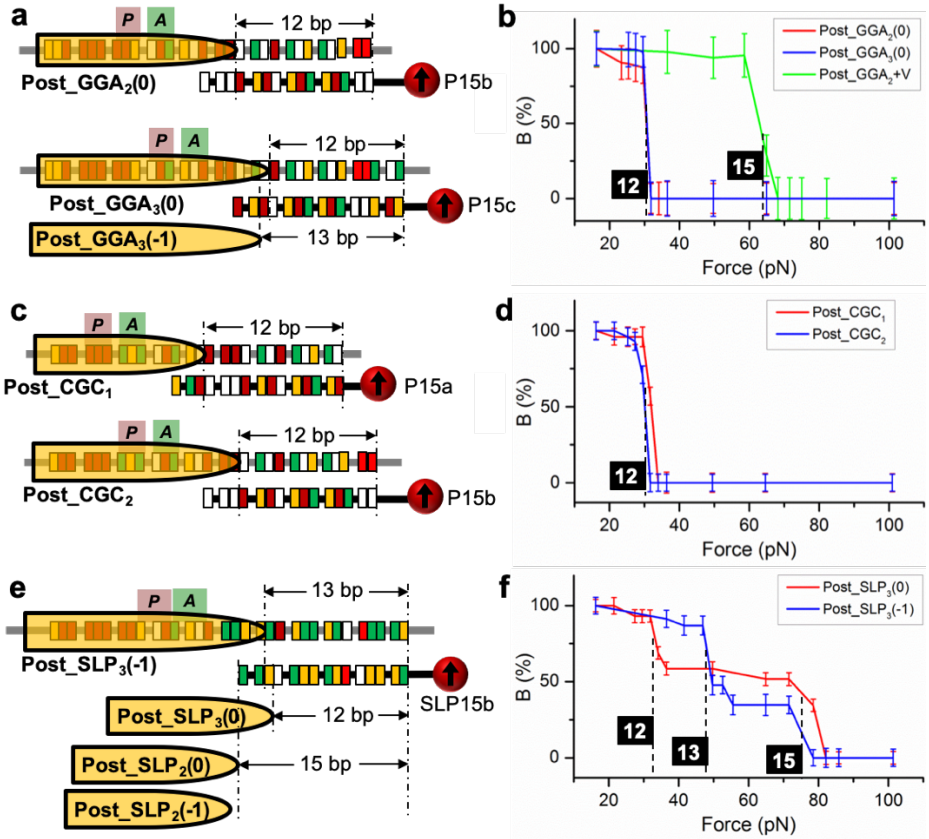

Figure 2.7 Control experiments to confirm the roles of the slippery sequence and the stem loop. **(a,b)** Scheme and results for probing the second and third translocation products when GGA replaced GAA in the GA$_7$G motif. The appearance of only 12-bp dissociation force in the red and blue traces indicated only the "0" frame product in Post_GGA$_2$ and Post_GGA$_3$, respectively. When the downstream aminoacyl tRNA for the "-1" frame translation, no Post_GGA$_3$(-1) was formed, because no13 bp duplex was detected. The15-bp corresponds to the unreacted Post_GGA$_2$(0). **(c,d)** Scheme and results for probing the translocation products when CGC replaced the AAG in the GA$_7$G motif. The appearance of only 12-bp dissociation force in both Post_CGC$_1$ and Post_CGC$_2$ showed that only the "0" frame products existed in the first two translocation steps. **(e, f)** Scheme and results for the GA$_7$G motif coupled with the stem loop. The Post_SLP$_3$(0) trace showed ~40% 12-bp duplex and 60% 15-bp duplex. The former was the desired "0" frame product. The latter was the unreacted Post_SLP$_2$(-1). This is because only the amino acyl tRNA corresponding to the "0" frame was present. Similarly, the Post_SLP$_3$(-1) contained ~60% the desired 12-bp duplex, and the remaining 40% unreacted Post_SLP$_2$(0). The "-1" frameshifting percentage was similar to that in Post-SLP$_1$ (Figure 2.4f).

2.3.3 Framshifitings confirmed by toe-printing assay and protein expression

The FIRMS results were confirmed with conventional biochemical assays. First, the ribosome toe-printing was conducted on an mRNA with GA_7G motif implemented.[23] The ribosomes were paused after synthesizing the "MFEKK" peptide. Two control mRNAs, one with a downstream stem-loop after GA_7G and the other with "GAA AGU AAG" in place of GA_7G, were assayed side-by-side. The sequences were named "GA_7G" (Figure 2.8, Lane 3), "SLP" (Lane 2) and "AGU" (Lane 4), respectively. The standard protocol was followed, except that Cy5-labeled primers were used instead of ^{32}P-labeled primers. Given the weak processivity of reverse transcriptase, toe-printing patterns are always present with discrete multi-bands because of enzyme drop-off. Therefore, this assay has limitations in quantifying frameshifting efficiencies. Regardless, the nonrandom multi-bands patterns supported the frameshifting processes. In the nonframeshifting sequence (Lane 4), the ribosome carrying MFESK was 16-nt away from the P-site codon "AAG", generating a 47 nt cDNA. Meanwhile, the "GA_7G" sequence exhibited both "-1" and "-2" frameshifted bands near 47-nt. In the presence of the stem loop, only "-1" frameshifting was observed. The pattern for "GA_7G" was more diffuse because of the more branches of frameshifting pathways, similar to other reports.[24]

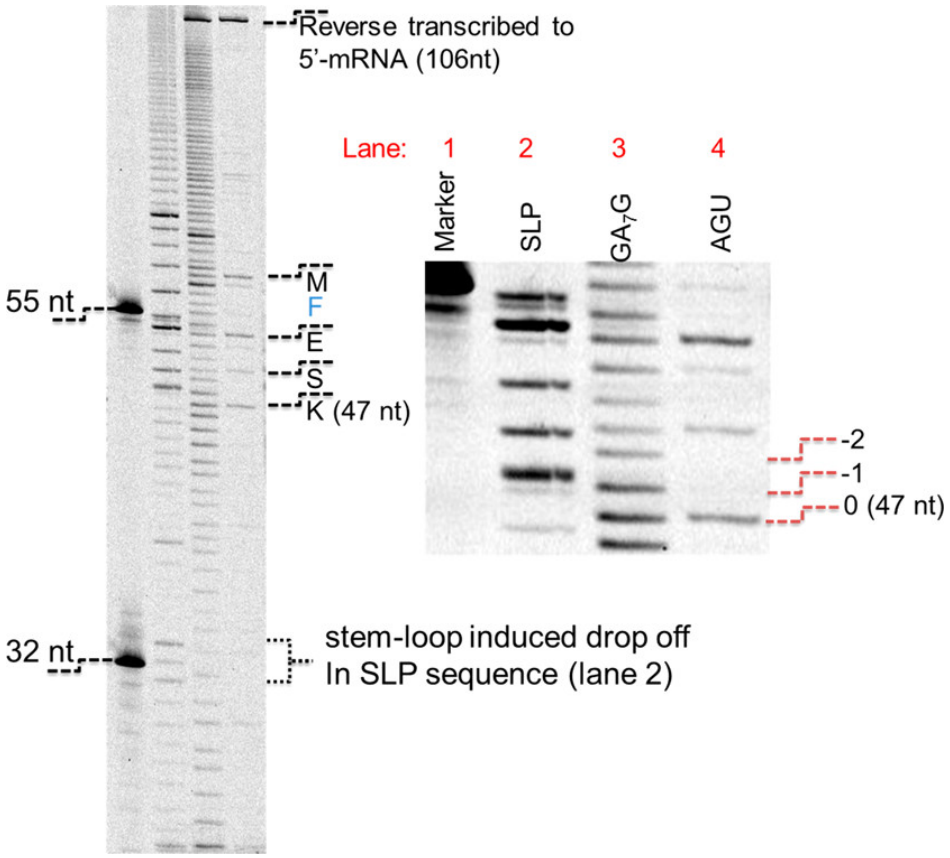

Figure 2.8 Toe-printing assays verified the frameshifting. The toe-printing assays of the cDNAs that were reverse transcribed with Cy5- labeled primer. Lane 1: markers of 32 and 55 nt in lengths; Lanes 2, 3, and 4: toe-printing of SLP, GA_7G, and AGU sequences, respectively. The right panel was a close-up view that was obtained by averaging four repeated scans. In Lane 4, the distinct bands were consistent with the decoding of K, S, E, and M, respectively. The bands near 106-nt at the top of the plots were the cDNAs reverse transcribed to the 5′-of the mRNAs.

Second, the GA_7G motif was tested with recombinant protein expression in the *E. coli* cells. The "GA_7G" motif without the downstream stem loop was incorporated into three constructs that were inserted in the pET20b (+) vectors. The constructs were shown in Table 2.2. The 8.5 kDa protein sequence was modified from a shorter peptide sequence of ribosomal protein L27.[25] Proteins were approximately 8.5, 6.5, and 4.6 kDa (Table 2.3). These constructs were expressed and purified via the Ni-NTA columns. The constructs I

and II generated the 8.5 kDa proteins with similar yields, via "0" and "-1" translocation processes, respectively (Figure 2.2a). The proteins were identified by N- terminal Edman sequencing (Figures 2.2b,c). The time-course of the IPTG induced protein synthesis was monitored with SDS-PAGE (Figure 2.9). Conversely, we were not able to isolate the similar protein in construct III, probably due to plasmid instability or protease digestion. However, the "-2" frameshifting protein was successfully expressed when the 28.8 kDa mCherry protein sequence was placed in the "-2" reading frame of construct II (Figure 2.10). However, no protein bands for the 6.5 or 4.6 kDa were observed. The 6.5 kDa protein sequence was further implemented in the same vector without the slippery site, and it was not isolated. Therefore, the proteins in the other two frames were not stable. Because the proteins decoded in the other two frames were fixed, we could not design a sequence which simultaneously decodes for three stable proteins in all three reading frames.

Table 2.3 The first seven amino acid sequences in the three ORFs of the three constructs

MW (kDA)	Theoretical parameter		Construct I		Construct II		Construct III	
	Solubility[a]	Instability[b]	Sequence[c]	Frame	Sequence	Frame	Sequence	Frame
8.5	Yes	30	MFEKK LS	0	MFEKK AL	-1	MFEKK SL	-2
6.5	Yes	15.2	MFEKK AQ	-1	MFEKK SA	-2	MFEKK PQ	0
4.5	Yes	14.6	MFEKK SS	-2	MFEKK RS	0	MFEKK AS	-1

ORFs: open reading frames

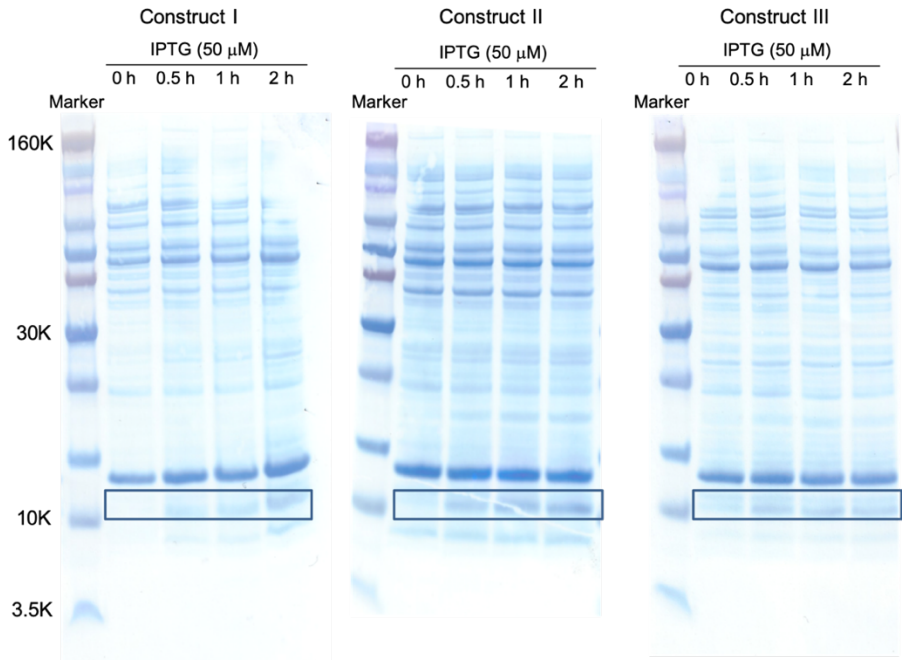

Figure 2.9 The SDS-PAGE images of IPTG induced protein expression in constructs I-III. The boxes framed the protein of interested in crude cell lysates. For constructs I and II, the proteins were expressed more with longer time. For construct III, the similar protein band was not responding to the IPTG induction, which agreed with the N-terminal sequencing result that the targeted protein was not expressed successfully.

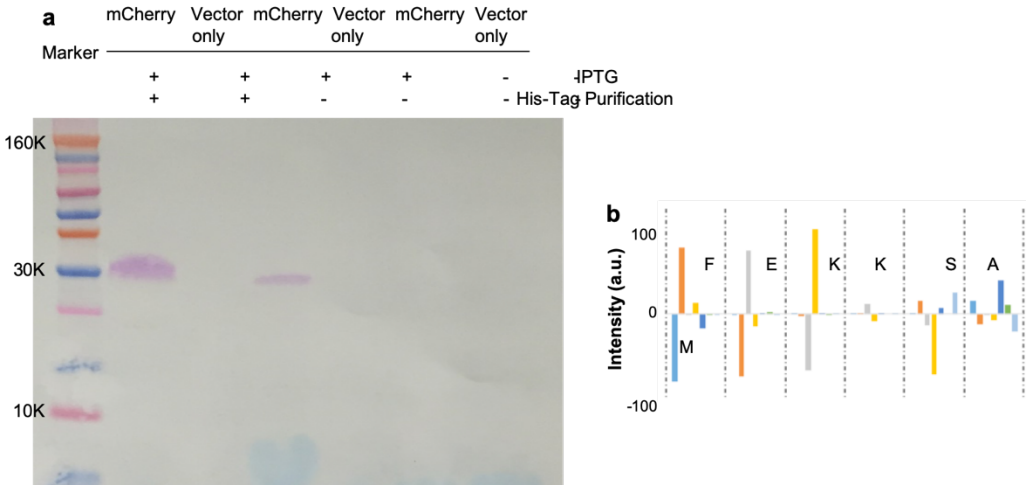

Figure 2.10 Observation of the mCherry fluorescent protein expression in the "-2" reading frame. **(a)** The SDS-PAGE image of the recombinant expression of mCherry protein after the FPLC purification. The ~30 kDa protein was visible without staining. Lanes 2, 4 and 6 showed the mCherry expression was dependent on IPTG induction; and lanes 3, 5 and 7 showed no protein expression with the empty vector. **(b)** Edman sequencing of the mCherry protein, which shows that the peptide in the "-2" frame was translated.

Although we cannot directly estimate the frameshifting efficiencies because not all of the proteins in the three reading frames were expressed simultaneously, the preparation protocol was exactly the same and 500−1000 pmol of the 8.5 kDa protein (for construct I and II) or mCherry protein was obtained, suggesting the similar partition in all three reading frames.

Third, the "GA_7G" motif was tested in the PURExpress kit with mRNAs instead of DNAs. As shown in Table 2.4, four mRNA constructs were synthesized by in vitro transcription, which incorporated with the mCherry protein in the 0, -1, -2, and 0 (without slippery site) reading frames, respectively. Construct IV and V were the positive control and background, respectively. The proteins were synthesized for 2 h and fluorescence were measured. The measurements for experiments I−III were normalized with experiment IV after subtracting background from experiment V. The relative yields for the "0", "-1", and "-2" frameshiftings were then calculated to be 34%, 35%, and 31%, respectively. These results were consistent with the FIRMS observations and agreed with the relative yields deduced from the recombinant protein synthesis results. Although in vitro transcribed mRNA still could not rule out transcriptional slippage, the very high yield of the frameshifting efficiencies compared to the 1-2% yield of the transcriptional slippages [7,8] strongly favored the ribosome slippage in our observations.

Table 2.4 The mRNA sequences and fluorescence readings of the mRNA-based translation with cell-free PURExpress kit

Complex	5'-Fragment[a]	Variation[b]	3'-Fragment	Fluorescence (a.u. X 10^4)
I	ATG-TTT-GAA-AAA-AAG	--	m Cherry sequecne	1.46 ± 0.012
II		CG		1.49 ± 0.014
II		C-		1.41 ± 0.008
IV	ATG-TTT-GAA-AGT-AAG	--		1.51 ± 0.015
V	No mRNA			0.85 ± 0.009

a. Complexes I-III contain the same fragment with GA_7G motif. b. "-" indicates null.

2.3.4 Further investigation on $Post_2$ and $Post_3$

After confirming the FIRMS results with conventional biochemical means, we tracked the second translation step with P15b by incubating $Post_1$ with Lys- $tRNA^{Lys}$ ternary complex and EF-G·GTP. Therefore, 12-, 13-, and 14-bp still, respectively, refer to the "0", "−1", and "−2" reading frames (Figure 2.3b). The result showed only the "−1" and "−2" products (Figure 2.11a). The overlay of the traces for $Post_1$ and $Post_2$ showed that these two traces were almost identical (Figure 2.12), implying that frameshifting may occur only at the translocation of the "AAA" codon, and normal translocation proceeds from $Post_1$ to $Post_2$. However, we cannot rule out the possibility of a second frameshifting step that result in the same distribution of "-1" and "-2" frameshiftings, as indicated by the toe-printing experiments. Nevertheless, a second frameshifting step was indeed observed to form $Post_3(0)$ when the $Post_2$ complexes were incubated with the next "0" frame substrate

Tyr-tRNA^{Tyr} ternary complex (decodes "UAC") and EF-G·GTP. This complex was probe with P15c. Figure 2.11b shows the existence of 12-bp duplexes at 27 pN, corresponding to $Post_3(0)$ (red trace). Both $Post_3(-1)$ and $Post_3(-2)$ were absent. The 15-bp binding force was due to residual $Post_2$ complex in which the ribosome front did not reach the probe. The "+1" or "+2" frameshifting to restore the "0" reading frame is probably via the "hungry codon" mechanism[26] to form $Pre_3(0)$, which exhibited only 15 bp binding force in the absence of EF-G·GTP (green trace).

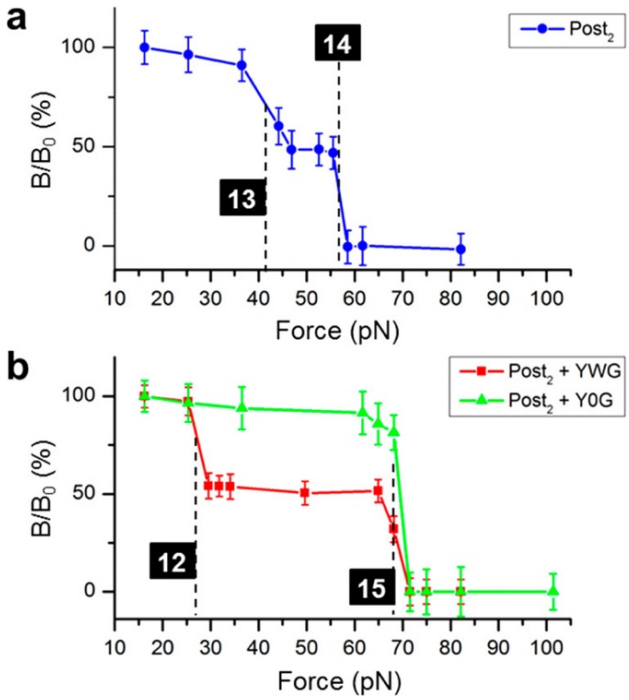

Figure 2.11 Products of the second- and third-step translocations. **(a)** FIRMS profile showing the formation of $Post_2$ (-1) and $Post_2(-2)$, indicated by the 13-bp dissociation at 42 pN and the 14-bp dissociation at 57 pN, respectively. **(b)** FIRMS profiles showing the formation of $Post_3(0)$ via $Post_2$ only in the presence of EF-G·GTP, indicated by the 12-bp duplex. YWG: mix of Y-tRNA^{tyr}, Tu·GTP, and EF-G·GTP. Y0G: mix of Y-tRNA^{tyr} and Tu·GTP only, without EF-G· GTP.

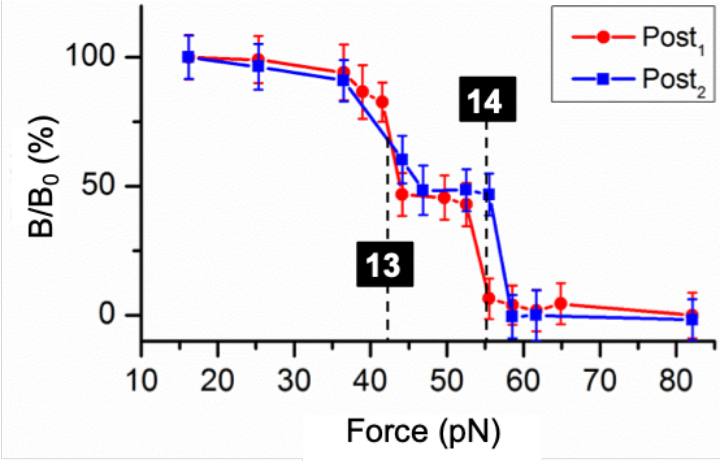

Figure 2.12 Overlaying FIRMS profiles of $Post_1$ probed by P15a and $Post_2$ probed by P15b. The overlapping profiles showed that the reading frame distribution was probably preserved in the second translocation step. In other words, normal translocation proceeded in the second translocation step, in contrast to the "-1" and "-2" frameshiftings occurred in the first translocation step.

To explain the lack of the "0" frame product in $Post_1$ and $Post_2$, the $Post_3$ complexes were prepared in one-pot from the initiation complex, in which the ribosome had completed the slippery sequence. Under these conditions, $Post_3(0)$ was formed, which suggested that the "0" frame translocation may be favored kinetically in the presence of the in-frame aminoacyl tRNAs, without pausing on the slippery site. In addition, when aminoacyl tRNAs for the other reading frames were provided exclusively, the ribosome was biased to the corresponding frame efficiently, indicating the powerful decoding roles of tRNAs.

The initiation complex was incubated with total tRNA and one set of amino acids to form the $Post_3$ complexes in the three frames separately: Phe, Glu, Lys, and Tyr for "0" frame; Phe, Glu, Lys, and Val for "-1" frame; Phe, Glu, Lys, and Ser for "-2" frame. Using probe P15c, the FIRMS results were expected to contain two transitions for each complex: the $Post_3$ of one specific reading frame and the stalled $Post_2$ of the other two frames.

$Post_3(0)$, $Post_3(-1)$, and $Post_3(-2)$ will form 12-, 13-, and 14-bp duplexes with P15c, respectively (Figure 2.13a). All $Post_2$ complexes will form 15-bp duplexes only. Figure 2.13b shows that under each condition, approximately 50% ribosome formed $Post_3$ complex of the specific reading frame, and the remaining was $Post_2$. The high-yield formation of $Post_3(-1)$ and $Post_3$ (-2) demonstrated that the frameshiftings of $Post_1$ on GA_7G motif are intrinsic, not due to *in vitro* artificial pausing, which could induce "-1" and "+1" frameshiftings[26]. However, it is possible that the frameshifting yields in Figure 2.4 were higher in our experiments than in the cell because of the pausing and more complicated factors in the cell.

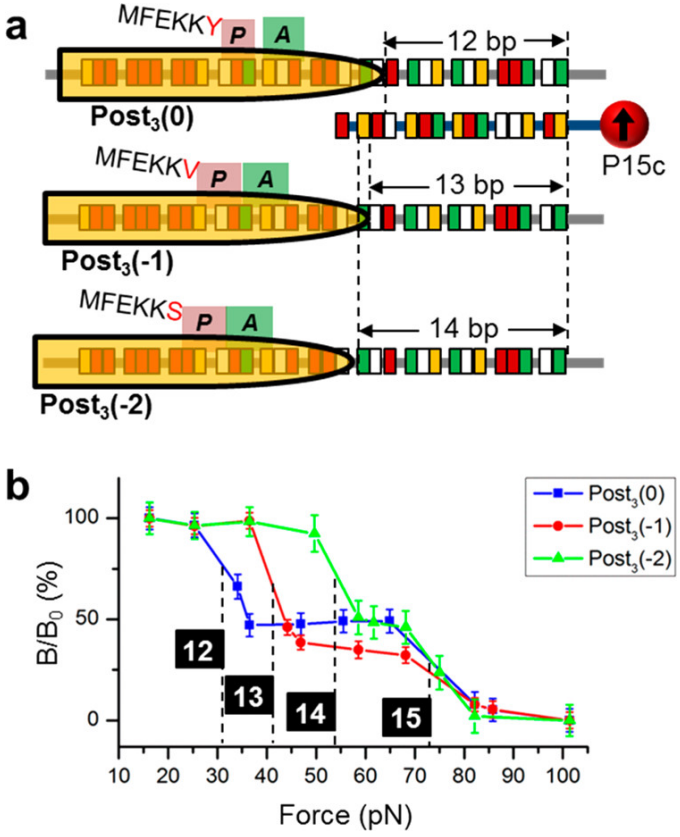

Figure 2.13 Frameshifting products after three continuous translocation steps from the initial complex. **(a)** Detection scheme of the three reading frames using P15c. **(b)** FIRMS profiles. $Post_3$ in all three reading frames were formed, indicated by the 12-bp duplex for $Post_3(0)$, 13-bp for $Post_3(-1)$, and 14-bp for $Post_3(-2)$, respectively.

On the other hand, the absence of the "0" product in $Post_1$ and $Post_2$ may be because the prolonged pausing has weakened the kinetic advantage of normal translocation [13]. To examine this hypothesis, under $Post_3(0)$ formation condition (blue trace of Figure 2.13b), the composition of the residual $post_2$ complexes were studied with the P15b. $Post_3(0)$ would form 9-bp duplex with this probe, which is unstable to be detected by FIRMS. Figure 2.14 showed that $Post_2$ complexes in all three reading frames were formed. The "0" frame ribosomal complexes at $Post_2(0)/Pre_3(0)$ were the major products (indicated by the 12 bp binding force), while $Post_2(-1)$ and $Post_2(-2)$ complexes were also formed with significant percentages (indicated by the 13- and 14-bp binding forces, respectively). Note that $Pre_3(0)$ could form, but it would be indistinguishable from $Post_2(0)$. Therefore, Figure 2.14 showed that the ribosome preferred the "0" frame if it was not halted at the slippery site. Our study implies that the "0" frame product is either the kinetically favored product in the cell (Figures 2.13 and 2.14) or the accumulating outcome of multistep frameshiftings (Figure 2.11).

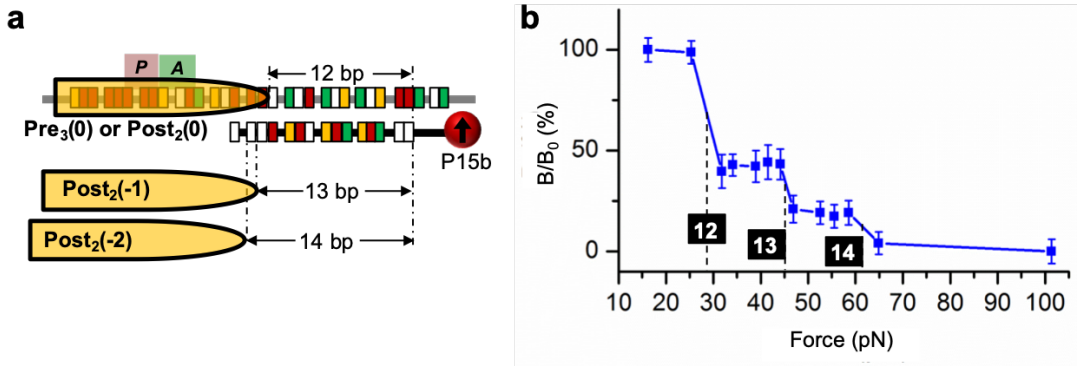

Figure 2.14 Formation of the "0" frame ribosome complex prior to $Post_3(0)$. **(a)** Detection scheme. Probing DNA P15b was used to distinguish the different reading frames following the second translocation step. The "0" reading frame, in the form of either $Post_2(0)$ or $Pre_3(0)$, will be shown as 12-bp duplex. **(b)** FIRMS profile. The main product is 12-bp duplexes, indicating the presence of the "0" reading frame.

2.3.5 The roles of tRNAs and GTP in ribosomal frameshiftings

We observed two tRNA effects in governing the frameshifting. The first one is the suppression of frameshifting when the P-site codon is changed from “GAA” to “GGA”, probably because of the stronger codon-anticodon interaction for an “A-G” than a “T-A” pair. The second one is the induction of the ribosome into any of the three reading frames with the corresponding set of substrates, showing the role of the A-site tRNA. These two observations suggest that frameshifting is the synergistic outcome of P-site tRNA repairing and A-site tRNA sampling, which corroborate a previous model.[27] The A-site tRNA has been suggested to decode with only two nucleotides at a hungry codon, which can prompt frameshifting in both the “+1” and “-1” directions.[26] In addition, changing the codon at the slippery site or its proximity has changed the frameshifting efficiencies.[12,28] However, to our best knowledge, this report is the first time to show that all three reading frames can be translated by their in-frame tRNAs. Therefore, our results showed more prominent active role of tRNAs in guiding the ribosome into certain ORFs.

We have also shown that translocation on the “GA_7G-only” motif with EF-G· GDPCP generated normal translocation, on the contrary to the EF-G·GTP experiments; A-site substrate without EF-G cannot drive $Post_2$ into $Post_3$, on the contrary to when EF-G·GTP is present. Some recent kinetics studies have revealed transient translocation intermediates (67−280 ms lifetime) in which the mRNA has moved three nucleotides while the ribosome is in the process to form the canonical post-translocation configuration.[29,30] However, it is unlikely that the lack of frameshifting with EF-G·GDPCP observed here is due to this intermediate state because of the very different time scale in this study. On the

other hand, EF-G·GDPCP is competent in translocation at 0.5 s^{-1} turnover rate,[30,31] which means that under our experimental conditions, most ribosomes were turned into the post-translocation configuration. Therefore, these results indicate that the GTP energy is essential to overcome the frameshifting reaction barrier, whereas without GTP translocation the process proceeds via alternative pathways. This conclusion is consistent with our previous report that an 89 pN mechanical force accompanies the GTP hydrolysis by EF-G [17]. A Cryo-EM study has revealed significant tRNA deformation induced by EF-G, which also implies the involvement of mechanical force.[32] An X-ray structural study observed the ribosome-EF-G complex in the mid-translocation, showing that while the P-site tRNA moved precisely along the 30S-head swiveling, the A-site tRNA moved 0.65 nm further to avoid clash with the EF-G domain IV.[33] This structure implied that the EF-G exerted its force on the A-site tRNA. Then the mRNA moves accordingly via its interactions with the tRNAs.

2.4 Conclusions

In conclusion, we have unambiguously revealed the highly efficient "-1" and "-2" frameshiftings on a GA_7G slippery mRNA without the downstream secondary structure, using force-induced remnant magnetization spectroscopy combined with unique probing schemes. The result represents the first experimental evidence of multiple frameshifting steps. It is also one of the rare reports of the "-2" frameshifting. Our assay removed the ambiguity of transcriptional slippage involvement in other frameshifting assays. Two significant insights for the frameshifting mechanism were revealed. First, EF-G·GTP is indispensable to frameshifting. Although EFG·GDPCP has been shown to

prompt translocation before, we found that it could not induce frameshifting. This implies that the GTP hydrolysis is responsible for the codon-anticodon repairing in frameshifting, which corroborates our previous mechanical force measurement of EF-G·GTP. Second, translation in all three reading frames of the slippery sequence can be induced by the corresponding in-frame aminoacyl tRNAs. Although A-site tRNA is known to affect the partition between "0" and "-1" frameshifting, it has not been reported that all three reading frames can be translated by their corresponding tRNAs. The *in vitro* results were confirmed by toe-printing assay and protein sequencing.

2.5 References

1. Baranov, P. V., Gesteland, R. F. & Atkins, J. F. Recoding: translational bifurcations in gene expression. *Gene* **286**, 187–201 (2002).
2. Firth, A. E. & Brierley, I. Non-canonical translation in RNA viruses. *J. Gen. Virol.* **93**, 1385–1409 (2012).
3. Adamski, F. M., Donly, B. C. & Tate, W. P. Competition between frameshifting, termination and suppression at the frameshift site in the Escherichia coli release factor-2 mRNA. *Nucleic Acids Res.* **21**, 5074–5078 (1993).
4. Sharma, V., Prere, M. F., Canal, I., Firth, A. W., Atkins, J. F. *et al.* Analysis of tetra- and hepta-nucleotides motifs promoting -1 ribosomal frameshifting in Escherichia coli. *Nucleic Acids Res.* **42**, 7210–7225 (2014).
5. Fang, Y., Treffers, E. E., Li, Y., Tas, A., Sun, Z. *et al.* Efficient −2 frameshifting by mammalian ribosomes to synthesize an additional arterivirus protein. *Proc. Natl. Acad. Sci.* **109**, E2920–E2928 (2012).
6. Chung, B. Y.-W., Miller, W. A., Atkins, J. F. & Firth, A. E. An overlapping essential gene in the Potyviridae. *Proc. Natl. Acad. Sci.* **105**, 5897–5902 (2008).
7. Rodamilans, B., Valli, A., Mingot, A., Leon, D. S., Baulcombe, D. *et al.* RNA polymerase slippage as a mechanism for the production of frameshift gene products in plant viruses of the potyviridae family. *J. Virol.* **89**, 6965–6967 (2015).
8. Olspert, A., Chung, B. Y.-W., Atkins, J. F., Carr, J. P. & Firth, A. E. Transcriptional slippage in the positive-sense RNA virus family Potyviridae. *EMBO Rep.* **16**, 995–1004 (2015).
9. Li, Y., Treffers, E. E., Napthine, S., Tas, A., Zhu, L. *et al.* Transactivation of programmed ribosomal frameshifting by a viral protein. *Proc. Natl. Acad. Sci.* **111**, E2172–E2181 (2014).
10. Grentzmann, G., Kelly, P. J., Laalami, S., Shuda, M., Firpo, M. A. *et al.* Release factor RF-3 GTPase activity acts in disassembly of the ribosome termination complex. *RNA* **4**, 973–983 (1998).
11. Yan, S., Wen, J.-D., Bustamante, C. & Tinoco, I. Ribosome excursions during mRNA translocation mediate broad branching of frameshift pathways. *Cell* **160**, 870–881 (2015).
12. Chen, J., Petrov, A., Johansson, M., Tsai, A., O'Leary, S. E. *et al.* Dynamic pathways of −1 translational frameshifting. *Nature* **512**, 328–332 (2014).
13. Caliskan, N., Katunin, V. I., Belardinelli, R., Peske, F. & Rodnina, M. V. Programmed –1 frameshifting by kinetic partitioning during impeded translocation. *Cell* **157**, 1619–1631 (2014).

14. Shirokikh, N. E., Alkalaeva, E. Z., Vassilenko, K. S., Afonina, Z. A., Alekhina, O. M. *et al.* Quantitative analysis of ribosome–mRNA complexes at different translation stages. *Nucleic Acids Res.* **38**, e15–e15 (2010).

15. Gamper, H. B., Masuda, I., Frenkel-Morgenstern, M. & Hou, Y.-M. Maintenance of protein synthesis reading frame by EF-P and m(1)G37-tRNA. *Nat. Commun.* **6**, 7226 (2015).

16. Gamper, H. B., Masuda, I., Frenkel-Morgenstern, M. & Hou, Y.-M. The UGG ssoacceptor of tRNAPro is naturally prone to frameshifts. *Int. J. Mol. Sci.* **16**, 14866–14883 (2015).

17. Yao, L., Li, Y., Tsai, T.-W., Xu, S. & Wang, Y. Noninvasive measurement of the mechanical force generated by motor protein EF-G during ribosome translocation. *Angew Chem*. *Int. Ed.* **52**, 14041-14044 (2013).

18. Qu, X., Wen, J. D., Lancaster, L., Noller, H. F., Bustamante, C. *et al.* The ribosome uses two active mechanisms to unwind messenger RNA during translation. *Nature* **475**, 118–121 (2011).

19. Takyar, S., Hickerson, R. P. & Noller, H. F. mRNA helicase activity of the ribosome. *Cell* **120**, 49–58 (2005).

20. Katunin, V. I., Savelsbergh, A., Rodnina, M. V. & Wintermeyer, W. Coupling of GTP hydrolysis by elongation factor G to translocation and factor recycling on the ribosome. *Biochemistry* **41**, 12806–12812 (2002).

21. Kim, H.-K., Liu, F., Fei, J., Bustamante, C., Gonzalez, R. L. & Tinoco, I. A frameshifting stimulatory stem loop destabilizes the hybrid state and impedes ribosomal translocation. *Proc. Natl. Acad. Sci.* **111**, 5538–5543 (2014).

22. Larsen, B., Wills, N. M., Gesteland, R. F. & Atkins, J. F. rRNA-mRNA base pairing stimulates a programmed -1 ribosomal frameshift. *J. Bacteriol.* **176**, 6842–6851 (1994).

23. Vazquez-Laslop, N., Thum, C. & Mankin, A. S. Molecular mechanism of drug-dependent ribosome stalling. *Mol. Cell* **30**, 190–202 (2008).

24. Koutmou, K. S., Schuller, A. P., Brunelle, J. L., Radhakrishnan, A., Djuranovic, S. *et al.* Ribosomes slide on lysine-encoding homopolymeric A stretches. *eLife* **4**, e05534 (2015).

25. Altuntop, M. E., Ly, C. T. & Wang, Y. Single-molecule study of ribosome hierarchic dynamics at the peptidyl transferase center. *Biophys. J.* **99**, 3002–3009 (2010).

26. Gallant, J. & Lindsley, D. Ribosome frameshifting at hungry codons: sequence rules, directional specificity and possible relationship to mobile element behaviour. *Biochem. Soc. Trans.* **21**, 817–821 (1993).

27. Baranov, P. V., Gesteland, R. F. & Atkins, J. F. P-site tRNA is a crucial initiator of ribosomal frameshifting. *RNA N. Y. N* **10**, 221–230 (2004).

28. Mathew, S. F., Crowe-McAuliffe, C., Graves, R., Cardno, T. S., McKinney, C. *et al.* The highly conserved codon following the slippery sequence supports -1 frameshift efficiency at the HIV-1 frameshift site. *PloS One* **10**, e0122176 (2015).
29. Wasserman, M. R., Alejo, J. L., Altman, R. B. & Blanchard, S. C. Multiperspective smFRET reveals rate-determining late intermediates of ribosomal translocation. *Nat. Struct. Mol. Biol.* **23**, 333–341 (2016).
30. Belardinelli, R., Sharma, H., Caliskan, N., Cunha, C. E., Peske, F. *et al.* Choreography of molecular movements during ribosome progression along mRNA. *Nat. Struct. Mol. Biol.* **23**, 342–348 (2016).
31. Rodnina, M. V., Savelsbergh, A., Katunin, V. I. & Wintermeyer, W. Hydrolysis of GTP by elongation factor G drives tRNA movement on the ribosome. *Nature* **385**, 37–41 (1997).
32. Namy, O., Moran, S. J., Stuart, D. I., Gilbert, R. J. C. & Brierley, I. A mechanical explanation of RNA pseudoknot function in programmed ribosomal frameshifting. *Nature* **441**, 244–247 (2006).
33. Zhou, J., Lancaster, L., Donohue, J. P. & Noller, H. F. How the ribosome hands the A-site tRNA to the P site during EF-G-catalyzed translocation. *Science* **345**, 1188–1191 (2014).

Chapter 3 Dual DNA Rulers Reveal an 'mRNA looping' Intermediate State during Ribosome Translocation

3.1 Introduction

One essential step of protein biosynthesis is the ribosomal translocation on the mRNA by exactly three nucleotides to decode the correct amino acid. There is no gap between codons. Therefore, one translocation error impacts all of the downstream codons, which is lethal and worse than single amino acid misincorporation errors.[132] However, the mechanism of accurate mRNA movement remains elusive, even after multiple seminal structural studies revealed an extensive rRNA to tRNA guiding network[133–136] because mRNAs lack well-defined conformations that can be aligned among different structures. Conversely, a method for objectively probing both the entrance and exit sites of the mRNA with single-nt resolution is necessary and has not been reported in the literature. For example, the toe-printing assay uses a reserve transcriptase primed at the 3′-distal end to transcribe the mRNA toward the ribosome.[78] The residue at the 3′ end of the mRNA exiting the ribosome is deduced by the cDNA length that was limited by the clash between the reserve transcriptase and the ribosome. The ribosome profiling method maps ribosome-covered mRNA with high throughput sequencing, which reveals the global ribosome distribution but lacks single codon precision.[79] Among indirect translocation assays, the tandem LC/MS/MS analysis of oligopeptide composition deduces the ribosome reading frame based on the synthesized peptide.[110] Fluorescently labeled tRNA binding/moving events reveal the translating codons,[112] and the puromycin reactivity assay is the conventional method for confirming the A-site vacancy resulting from translocation.[137]

None of these methods can reveal the movement at the 5′ end of the mRNA that is entering the ribosome.

Recently, we developed a force-induced remnant magnetization spectroscopy (FIRMS) technique that used DNA rulers to precisely determine the positions of the 3′ end of mRNA during ribosome translocation and frameshifting.[138,139] Briefly, the DNA rulers, which were labeled with magnetic beads, formed duplexes with a portion of the mRNA uncovered by the ribosome, and the length of the duplexes was then obtained from the dissociation force of the duplexes, which was measured by a sensitive atomic magnetometer through the decrease in magnetic signals resulting from the DNA ruler's removal from the surface under centrifugal forces. Single-nt resolution for the duplex length has been routinely achieved, resolving all the three reading frames of the ribosome on the mRNA. However, we have not shown effective probing at the 5′ end of mRNA and thus have not been able to provide the whole picture of mRNA movement.

In this report, we have developed a dual ruler assay that probes the ribosome-uncovered mRNA from both sides with single-nt resolution. For the first time, our results indicate a novel intermediate state that implied a ribosomal conformation in which the mRNA had moved 2 nt at the exit site (3′- end) but only 1 nt at the entrance site (5′-end). Based on structural and computational studies, we have suggested that the ribosome may translocate in a stepwise manner via an inchworm-like mRNA 'looping' mechanism.

3.2 Experimental section

3.2.1 Materials

All of the mRNAs and DNA probes are purchased from IDTDNA (Integrated DNA Technologies). The sequence of the mRNA was 5′-Bio- CAA CUG UUA AUU AAA UUA AAU UAA AAA GGA AAU AAAA AUG UUU AAU UUU UUA GGG CGC AAU CUA CUG CUG AAC UC-3′ (Bio: biotin functionalized). The underline indicates the slippery U6A motif that causes frameshifting. The probes are tabulated in Table 3.1 below.

Table 3.1 All probe DNA sequences

Translocation probes (TEG: linker molecule)		
Ribosome complex	5′-probe	3′probe
MF-Pre/Post	3′-**TAA TTT AAT TTA ATT TTT C**GA AAU AT_{50}/TEGBio/-5′	3′ -**AAA ATC CCG CGT TAG A**AC UGG GG/TEGBio/-5′
MFNF-Pre/Post	3′ -**AAT TTA ATT TTT CCT TTA** AAA AT_{50}/TEGBio/-5′	3′ -**CCG CGT TAG ATG ACG A**GA ACG GG/TEGBio/-5′
Force calibration probes		
12bp	3′ -**AGA TGA CGA CTT** CTC GGG/TEGBio/-5′	
13bp	3′ -**T AGA TGA CGA CTT** CTC GGG/TEGBio/-5′	
14bp	3′ -**TT AGA TGA CGA CTT** CTC GGG/TEGBio/-5′	
15bp	3′ -**GTT AGA TGA CGA CTT** CTC GGG/TEGBio/-5′	

The magnetic beads were purchased from Invitrogen, under commercial name M280 that represents the particle diameter of 2.8 μm. All antibiotics were purchased from Sigma-Aldrich and used directly.

3.2.2 Preparation of ribosome complexes

All the mixtures were in TAM10 buffer, which consisted of 20 mM Tris-HCl (pH 7.5), 10 mM Mg $(OAc)_2$, 30 mM NH_4Cl, 70 mM KCl, 5 mM EDTA, and 7 mM BME (2-mercaptoethanol), and 0.05% $Tween_{20}$. Five mixtures were prepared: the ribosome mix, TuWG mix, Tu0G mix, Phe mix and Asnmix. The ribosome mix contains 1 μM ribosome, 1.5 μM each of IF1, IF2, IF3, 2 μM of mRNA, 4 μM of charged fMet-$tRNA^{fMet}$, and 4 mM of GTP. The TuWG mix contained 4 μM EF-Tu, 0.4 μM EF-Ts, 2 μM EF-G, 4 mM GTP, 4 mM PEP, and 0.02 mg/mL pyruvate kinase. The Tu0G mix contained no EF-G but all the other components in the TuWG mix. The Phe mix contained 100 mM Tris (pH 7.8), 20 mM $MgAc_2$, 1 mM EDTA, 4 mM ATP, 7 mM BME, 0.1 mg/mL total synthetase, 50 A260/ml total tRNA, and 0.25 mM phenylalanine. The Asn mix contained the same components except that the phenylalanine was replaced by Asparagine.

The five mixes were incubated at 37 °C for 25 min before making the ribosome complexes. The ribosome mix, TuWG mix, and Phe mix were incubated with 1:2:2 volume ratio at 37 °C for 15 min. The resulting MF-Post ribosome complex was added on 1.1 M sucrose cushion and purified by ultra- centrifuge. The ribosome preparation was similar to our previous work.[138]

The MF-Pre complex was formed by incubating the ribosome mix, Tu0G mix and A mix in the volume ratio of 1:2:2, at 37 °C for 2 min. The resulting ribosome complex was added on 1.1 M sucrose cushion and purified by ultra-centrifuge.

The MFN-Post was formed by incubating MF-Post (1 μM) with the Asn mix and TuWG mix in the volume ratio of 1:2:2 at 37 °C for 15 min. The resulting ribosome complex was added on 1.1 M sucrose cushion and purified by ultra-centrifuge.

The MFNF-Post was formed by incubating MFN-Post (1 μM) with the Phe mix and TuWG mix, in the volume ratio of 1:2:2, at 37 °C for 15 min. The resulting ribosome complex was added on 1.1 M sucrose cushion and purified by ultra-centrifuge.

The MFNF-Pre was formed by incubating the MFN-Post with Phe mix and Tu0G mix in the volume ratio of 1:2:2, at 37 °C for 2 min. The resulting ribosome complex was added on 1.1 M sucrose cushion and purified by ultra-centrifuge.

To capture the mRNA-looping intermediate state, neomy- cin was added into the MF-Pre ribosome complexes and incubated for 10 min at 37 °C. EF-G solution pre-incubated with fusidic acid for 20 min at 37 °C was added to the ribosome-mRNA complex, and incubated at 37 °C for an additional 5 min. The final conditions were 0.1 μM ribosome complexes, 2 μM EF-G, 4 mM GTP, 4 mM PEP, 0.02 mg/mL pyruvate kinase, 0.2 mM neomycin, and 0.25 mM fusidic acid.

All other antibiotics were prepared similarly. Viomycin, hygromycin B, and fusidic acid pre-incubated with EF-G were incubated with MF-Pre ribosome complexes, respectively. The final concentrations were 0.2 mM viomycin, 0.4 mM hygromycin B, 0.25 mM fusidic acid, respectively.

3.2.3 Sample preparation prior to magnetic and force measurements

A sample well with dimensions of 4×3×2 mm^3 (L×W×D) was glued with a piece of biotin coated glass on the bottom surface. An aqueous solution of 0.25 mg/mL streptavidin was loaded into the sample well and incubated for 40 min. Then the sample well was rinsed twice with TAM_{10} buffer.

For studies involving no antibiotics, 20 μL of 0.1 μM ribosome complexes were immobilized on the surface via the 5′-end biotin on the mRNA and incubated for 1 h. After rinsing the surface, 20 μL of 1 μM biotinylated probing DNA strand was added and incubate for overnight. The formed DNA-mRNA duplex was rinsed with TAM_{10} buffer. Subsequently, the streptavidin-coated magnetic beads were introduced into the sample well and incubated for 2 h, the non-specific bound magnetic particles were removed from the surface by applying centrifuge with the speed of 1000 rpm for 5 min. The sample was then magnetized for 2 min using a permanent magnet (~ 0.5 T).

3.2.4 Magnetic and force measurements

Figure 3.1 shows magnetic signal of the samples was measured by an atomic magnetometer as a function of mechanical force, using the force-induced remnant magnetization spectroscopy (FIRMS) technique.[138,139] The atomic magnetometer had a sensitivity of ~ 100 $fT/(Hz)^{1/2}$. The force was provided by a centrifuge (5427R from Eppendorf), with the speed increasing by 100 rpm (revolution per minute) per step. The dissociation of the DNA-mRNA duplexes was indicated by a decrease in the magnetic signal, which occurred when the centrifugal force reached the dissociation force of the

DNA-mRNA duplex. This is because the dissociated magnetic beads were removed from the sample. The typical force range in this work was 90 pN, after which the residual magnetic signal was taken as the background. FIRMS profiles were obtained by normalizing the overall magnetic signal decrease (B_0) to be 100% and then plotting the relative magnetic signal decrease (B/B_0) vs. the external force. The force values were calculated according to $m\omega^2 r$, in which m is the buoyant mass of M280 magnetic beads (4.6×10^{-15} kg), ω is the centrifugal speed, and r is the distance of the magnetic beads from the rotor axis (7.5 cm for 5427R). The typical force resolution was 3–4 pN in this work. Each profile reported in this work was repeated at least three times to assure reproducibility.

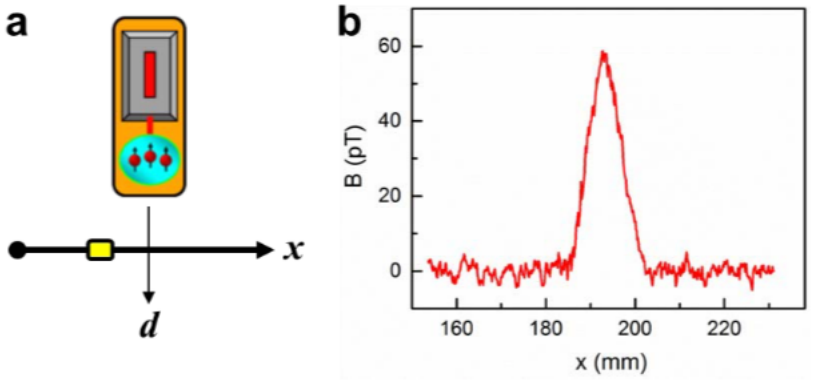

Fig. 3.1 Magnetic signal measurement of the samples. (**a**) Scheme of scanning magnetic detection with an atomic magnetometer. The sample is scanned along the *x*-axis, driven by a linear motor. Its magnetic field along the *d*-axis is measured by an atomic magnetometer.[82] (**b**) Representative magnetic measurement of a sample. The typical signal amplitude is 50 pT, corresponding to approximately 1.1×10^5 magnetic particles.[140] The noise level is approximately ±3.5 pT. Prior to magnetic measurement, the sample was subjected to 1000 rpm (revolution per minute) centrifugal force to remove nonspecifically absorbed particles on the surface.

3.3 Results and discussion

3.3.1 Dual DNA ruler assay and force calibration

The dual ruler assay is schematically shown in Figure 3.2(a). Two DNA rulers were designed to form duplexes with the uncovered mRNA: Ruler-In for the 5′-end and Ruler-Out for the 3′-end. The lengths of the duplexes are limited by the ribosome position on the mRNA. Consequently, the number of basepairs (bp) of the DNA-mRNA duplexes will reveal the mRNA movement during translocation. The DNAs are labeled with magnetic beads, so the existence of the DNA- mRNA duplexes is indicated by a magnetic signal. The number of bp of each duplex can be determined by FIRMS.[138,139] The challenge is for the DNA rulers to reach the mRNA between the ribosome and the surface, as shown at the 5′-mRNA side. To solve this problem, extra polyT linkers of 0, 10, 30, 50, and 70 T were introduced for Ruler-In. As shown in Figure 3.2(b), only linkers of at least 50 T led to successful DNA-mRNA hybridization, as indicated by a substantial magnetic signal. The length of 50 T is approximately 17 nm. Considering the approximately 20-nm diameter of ribosomes, 17 nm is approximately a quarter of the circumference of the cross-section circle (Figure 3.3). All Ruler-Ins in this report contained 50 T linkers. The linker does not affect the measured force, which is determined only by the binding strength of the mRNA-DNA duplex. At the dissociation force, the DNA probe (to which the magnetic beads are bound) is completely sheared from the surface in one step, in contrast to optical trap experiments in which the displacement of the bead correlates with the force via Hooke's law. In those experiments, an extra linker may interfere with the bead displacement through stretching of the additional linker. Conversely, a probe DNA with a 70 T linker was tested,

and the mRNA- DNA duplex exhibited the same dissociation force as the corresponding probe with a 50 T linker, demonstrating the linker's trivial effect on the measurement (Figure 3.4).

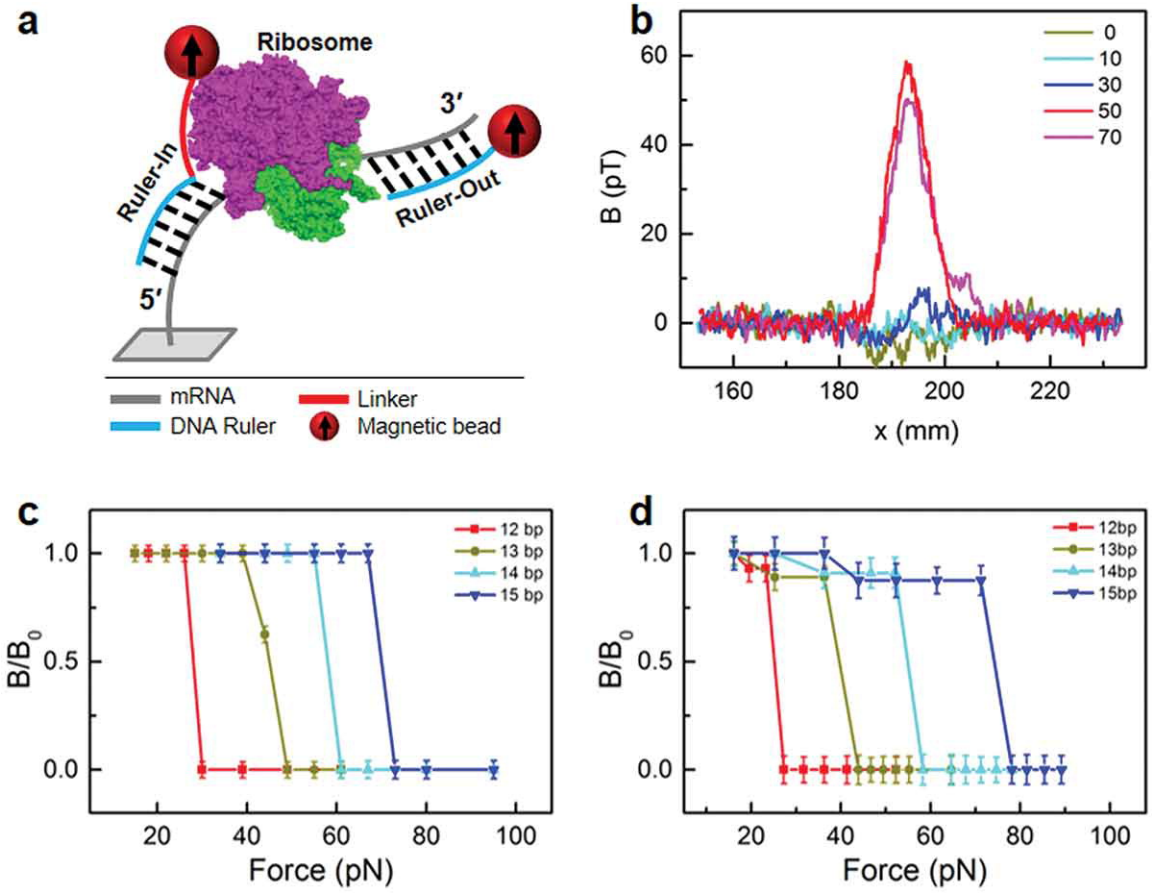

Figure 3.2 Dual ruler assay with single-nt resolution for studying ribosome translocation. (**a**) Schematic of the dual ruler assay, in which two DNA rulers are designed to respectively probe the 5′- and 3′-termini. The red line indicates the polyT linker. (**b**) Optimization of the linker length for Ruler-In. (**c**) FIRMS results to determine the dissociation forces of the duplexes between Ruler-Ins and mRNA. (**d**) Dissociation forces of the duplexes between Ruler-Outs and mRNA.

Figure 3.2 also shows the typical signal amplitude of 50 pT, which corresponds to 1.1×10^5 magnetic DNA-mRNA duplexes. Detection from the 3′-end with Ruler-Outs is similar to a previous report.[138] To demonstrate single-nt resolution for both rulers, we calibrated the force measurements for the DNA-mRNA duplexes in the absence of ribosomes. Figure 3.2(c) shows the FIRMS results for the 12-, 13-, 14- and 15-bp duplexes for Ruler-Ins, which were 28, 44, 57, and 70 pN, respectively. The force uncertainty was 3 pN. Because the force difference between duplexes with a 1-bp length difference was usually 12–18 pN, which is much greater than the force uncertainty, single-nt resolution was achieved for the 5′ end of the mRNA. Similarly, single-nt resolution was obtained for the 3′ end of the mRNA, which yielded 25, 40, 55, and 74 pN for the 12-, 13-, 14- and 15-bp duplexes, respectively, formed between the Ruler-Outs and the mRNA (Figure 3.2(d)). The force values are plotted against the length (bp) of the duplexes in Figure 3.4.

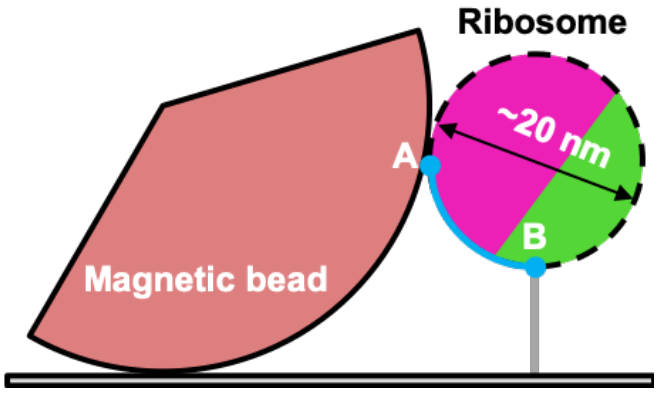

Figure 3.3 Scheme of probing the hindered mRNA at the 5′-terminus. The arc AB is a quarter of the circumference of the ribosome, which is approximated as a ~20-nm diameter circle.[135] The length of arc AB is therefore 16.5 nm. For the probing DNA labeled with a magnetic bead, it should have a linker that overcomes this distance to the reach the mRNA.

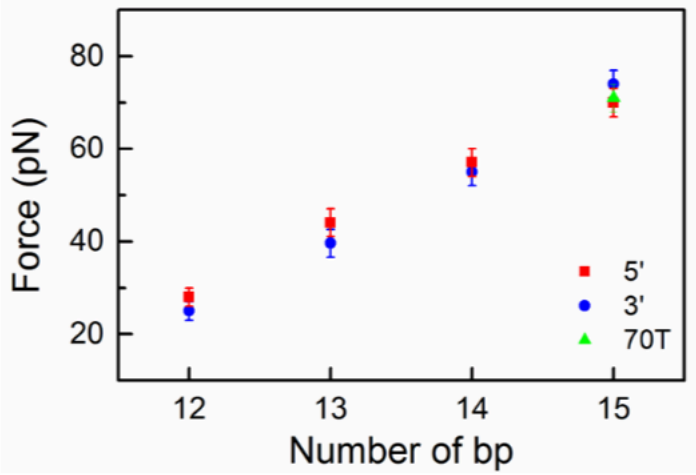

Figure 3.4 Plot of the dissociation force vs. bp for the DNA-mRNA duplexes. The duplexes include both formed by Ruler-Ins (probing 5′-mRNA with 50T linker) and Ruler-Outs (probing 3′-mRNA). The Ruler-In 15bp with 70T linker gives the same force as that measured by probe with 50T linker.

3.3.2 Normal translocation with and without antibiotics

We first applied the dual ruler assay to investigate normal translocation with and without various antibiotics (Figure 3.5(a)). The pre-translocation and post-translocation ribosome complexes are denoted Pre and Post, respectively. In these experiments, the MF-Pre complex carries vacant $tRNA^{fMet}$ and MF-$tRNA^{Phe}$ at the P- and A-sites, respectively. MF-Post carries $tRNA^{fMet}$ and MF-$tRNA^{Phe}$ at the E- and P-sites, respectively, with a vacant A-site (Figure 3.5(a), inset).

In the absence of antibiotics, the ribosome moved 3 nt toward the 3′-end; therefore, the mRNA-DNA duplexes at the 5′ side exhibited 12 bp and 15 bp binding forces in Pre and Post, respectively (Figure 3.5(b)). Conversely, the duplexes at the 3′ side exhibited a comparable but reversed change from 15 to 12 bp (Figure 3.5(c)). For clarity, the force

axes were oriented in opposite directions for the 3′ and 5′ sides so that the FIRMS traces for the Pre to Post transition were consistent with the ribosome movement direction. Together, Figure 3.5(b, c) showed that the ribosome covered 27 nt of the mRNA, in excellent agreement with the literature.[116] However, in the presence of both fusidic acid and neomycin (Figure 3.5(d, e), highlighted), our force spectra suggested that the ribosome moved only 1 nt at the 5′ side but 2 nt at the 3′ side. This result implied that the ribosome translocated via a stepwise mechanism and that the mRNA formed a loop with an extra nucleotide inside the ribosome. Alternatively, it is possible that the ribosome stretches to cover 28 nt of mRNA. Interestingly, normal translocation was completed after washing away of the antibiotics, as evidenced by 3 nt movements from both the 5′ and 3′ sides (purple trace in Figure 3.5(d, e)). For comparison, with only fusidic acid, the force spectra was consistent with the ribosome movement of 3 nt at both sides, similar to the situation for normal translocation (Figure 3.5(f, g)). Similar results were obtained when only neomycin was used (Figure 3.6(a, b)). Two other antibiotics known to inhibit translocation, viomycin (Figure 3.5(h, i)) and hygromycin B (Figure 3.6(c, d)), were also studied to confirm the detection method.[16] Both antibiotics inhibited translocation completely, as shown by 0 nt movement on both sides.

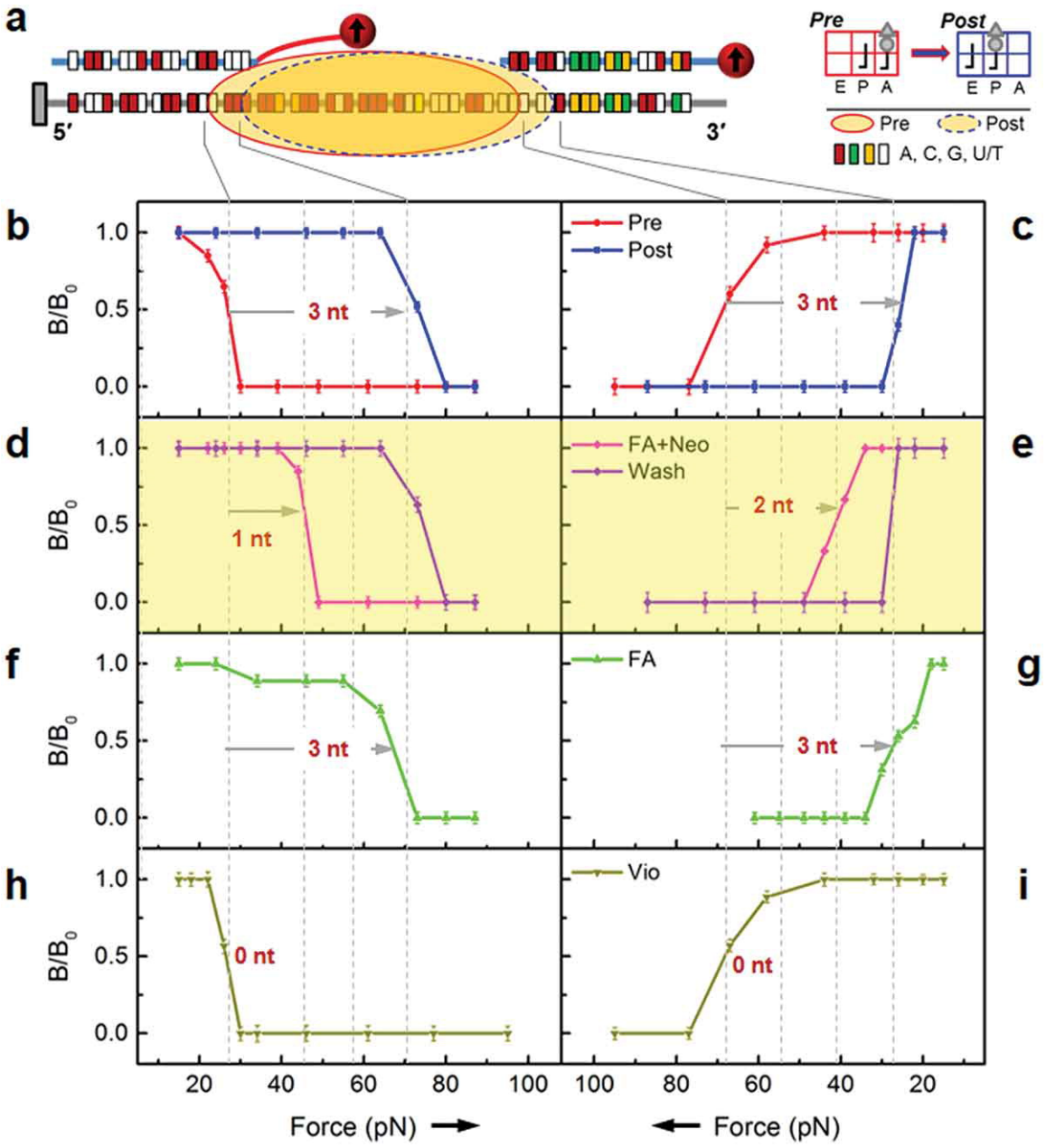

Figure 3.5 Probing translocation under the influence of various antibiotics. (**a**) Probing scheme for the MF-Pre and MF-Post complexes. Inset indicates the schematic ribosomes in Pre and Post, which correspond to the solid and dash-lined ovals, respectively. (**b, c**) FIRMS results with no antibiotics. (**d, e**) Results with both fusidic acid and neomycin. (**f, g**) Results with fusidic acid only. (**h, i**) Results with viomycin only. Left panels: Ruler-In from the 5' side; right panels: Ruler-Out from the 3' side.

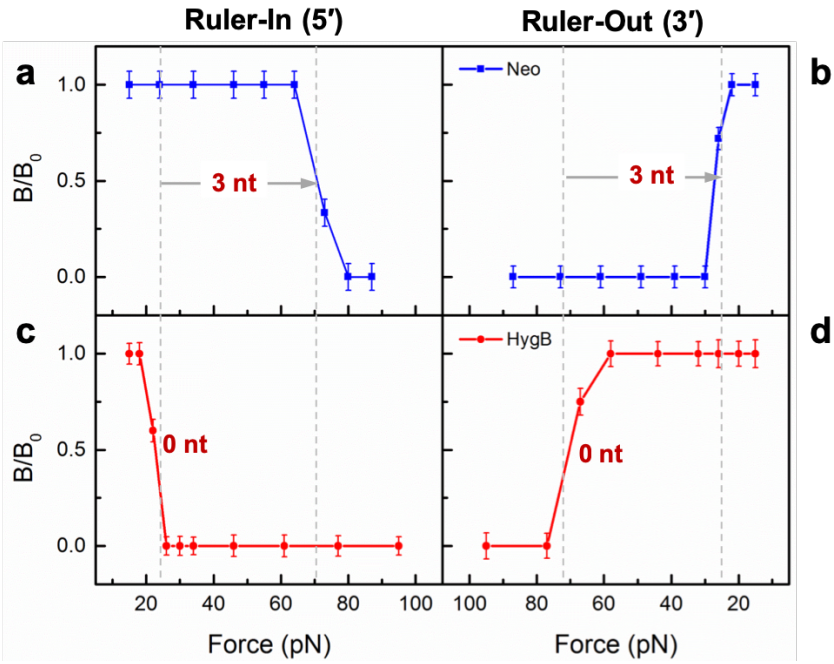

Figure 3.6 FIRMS results of MF-Pre and MF-Post using different antibiotics (the number of nt indicated the FIRMS measured mRNA movements). (**a, b**) With neomycin only. (**c, d**) With hygromycin B only. Left panels: Ruler-In from the 5′ side; right panels: Ruler-Out from the 3′ side.

3.3.3 Frameshifting with and without antibiotics

We then studied whether this partially translocated ribosome could form on a '-1' frameshifting motif. The MFNF-Pre and MFNF-Post ribosome complexes carried MFNF oligopeptide at the A- and P-sites, respectively. The translocation took place on the 'U6A' motif, which is part of the '-1' frameshifting motif in HIV.[17] As shown in Figure 3.7(a, b), duplexes shortening and lengthening of 2 and 3 nt were observed at 3′- and 5′-ends, respectively, suggesting both normal and '-1' frameshifting translocations, with nearly 50-50 partitions, as indicated by the corresponding magnetic signals. In the presence of both neomycin and fusidic acid, similar forces consistent with the inferred intermediate state

were also detected, which suggested the ribosome moved 2 and 1 nt at the 3′- and the 5′-ends, respectively (Figure 3.7(c, d)). However, in the presence of only fusidic acid (Figure 3.7(e, f)), the result was nearly the same as for MFNF-Post in Panels a and b (blue traces). These results implied that the partially translocated ribosome conformation that is inferred from our assay had formed regardless of the mRNA motif. Therefore, the different outcomes of normal and frameshifting translocations may diverge at a later stage of the process.

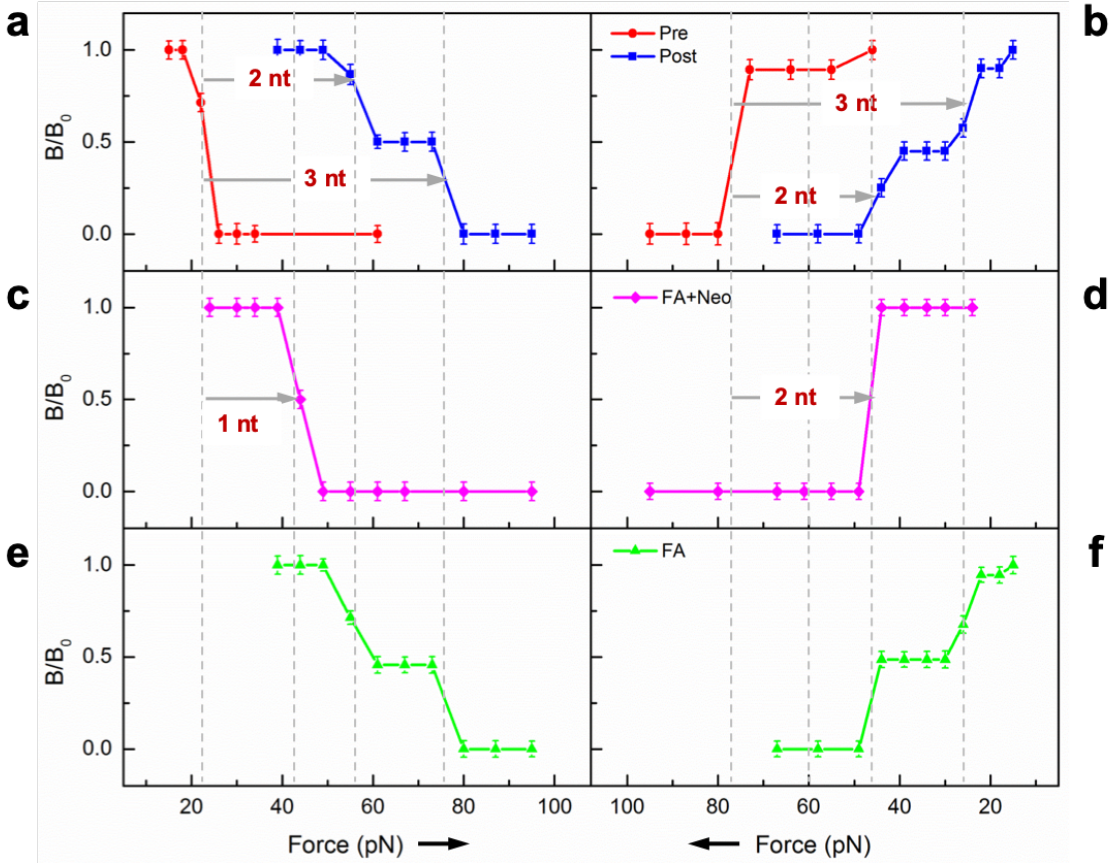

Figure 3.7 FIRMS results of dual rulers to probe frameshifting. (**a, b**) MFNF-Pre and MFNF-Post without antibiotics. (**c, d**) Results with both fusidic acid and neomycin. (**e, f**) Results with only fusidic acid. Left panels: Ruler-In from the 5′ side; right panels: Ruler-Out from the 3′ side.

Our results correlate well with two important structural studies. An intermediate trapped with fusidic acid and neomycin exhibited a 21° head swivel and 2.7° body rotation (Int1), while another intermediate trapped with fusidic acid alone exhibited an 18° head swivel and 5° body rotation (Int2).[2,3] In Int2, the A- and P-site tRNAs are in ap/P and pe/E configurations, respectively. The letters separated by the '/' indicate the tRNA binding sites in the 30S and 50S ribosomes, respectively. The two letters (ap) for the 30S binding site indicate the intra-30S hybrid state due to the 30S head swivel.[18] Conversely, in Int1, the tRNAs are in the ap/ap (the two letters for the 50S binding site indicate the intermediate location of the tRNA between the classic A- and P-sites[19,20]) and pe/E configurations. During translocation, the tRNAs move from the A- and P-sites to the P- and E-sites. Therefore, the ap/ap state must occur before the ap/P state along its moving track, i.e. Int1 occurs before Int2. Accordingly, we assign the ribosome states that exhibited force spectra in Figure 3.5(d, e) and 3.5(f, g) to Int1 and Int2, respectively, based on the use of the same antibiotic conditions. With both antibiotics, the translocation is partial, while complete translocation is observed with fusidic acid alone, which agrees with the transition from Int1 to Int2.

It is known that fusidic acid binds between EF-G domains I and III to prevent protein release, but fusidic acid does not inhibit one round of translocation,[21] Figure 3.5(f, g),are consistent with this circumstance. Conversely, neomycin binds at multiple sites, including h44 and around H69 and H70.[2] This drug was necessary to trap Int1 for the above- mentioned crystallographic study. It is also essential to trap the unique ribosome conformations here. In the structural study, alignment of mRNAs in Int1 and a pre-

translocation ribosome indicated that the mRNA had already translocated one codon at the 3′-side in Int1. Our results in Figure 3.5(d, e) agreed with this conclusion within experimental uncertainty, except that only 2 nt were translocated at the 3′-side.

3.3.4 'mRNA looping' intermediate state

Using the FIRMS technique to probe both the 3′ and 5′ sides of the ribosome-uncovered mRNA, we have obtained evidence for a unique ribosome conformation that is consistent with the mRNA movement of 2 and 1 nt at the 3′- and 5′- ends, respectively. These findings imply that the translocation is asymmetric and stepwise. In this conformation, the ribosome covered 28 nt of the mRNA, which is 1 nt longer than the normal 27 nt coverage in both the Pre and Post complexes. This conformation could be a consequence of either a 'looped' mRNA or ribosome expansion. A computational simulation indicated that the mRNA was clamped at 3′- and 5′-ends by two groups of proteins, (S3-5) and (S7, 8, 11), respectively. The clamps opened and closed alternately to keep the mRNA reading frame.[22] More recently, Nguyen and Whitford (2016) identified a 30S head tilting motion that is essential to release the steric hindrance along the mRNA pathway.[23] Both simulations indicated that the mRNA motion and the correct codon reading frame were tightly controlled by the ribosome internal structures. In addition, the Int1 state that was identified by X-ray crystallography has exhibited multiple expected intermediate rRNA-tRNA interactions that can guide tRNA movements, such as the approach of the 16S 966 loop to the A-tRNA and the simultaneous interaction of the A and P loops with the A-tRNA. Based on this information, it seems reasonable to assume that the inferred asymmetrically and partially translocated ribosome conformation in our study

corresponds to an intermediate state in which the 5′-clamp is closed, the head tilting has not finished, the 3′-clamp is opened, and the head has swiveled through a large angle. In Int1, the codon-anticodon interaction remained intact while the tRNAs adopted a compact conformation.[2] Therefore, it is possible that when the tRNAs become closer to each other, the attached mRNA is forced to form a loop.

Because this unique ribosome conformation is only observed in the presence of both fusidic acid and neomycin, it is unclear whether this conformation is kinetically sampled during normal translocation. However, two available observations support its biological significance. First, the above mentioned Int1 ribosome complex was prepared with the same two antibiotics with which many ribosomal components changed in the correct direction for the proper tRNA transition. Second, after antibiotics were washed away in our experiments, full translocation was achieved, which implies that the trapped intermediate state was along the true translocation pathway. Time-resolved measurements should be able to clarify this issue in the future.

Our result and its consistency with the literature enable us to propose a novel translocation mechanism (Figure 3.8). The ribosome conformation that exhibited the specific force spectra in Figure 3.5(d, e) and Figure 3.7(c, d) was probably the abovementioned Int1, in which the mRNA is transiently packed to form a loop due to the nonsynchronous dynamics at the two ribosome edges, as well as complex internal rearrangements. Washing away the antibiotics led this intermediate state to switch to Post, implying that the translocation steps after this intermediate state did not require energy. Therefore, the energy barrier before this intermediate state should be higher and probably

needs GTP hydrolysis energy from EF-G. We have measured an 89 pN force generated by EF-G. Given the approximately 75% usage of the hydrolysis energy of one GTP, this force should correspond to a distance of 1 but not 3 nt (0.5 nm for 1 nt movement).[24] Interestingly, this predicated working distance of 0.5 nm agreed well with the conformational change in Int1, which underwent a 0.6 nm A-site tRNA displacement concurrent with the movement of EF-G domain IV.[2] More simulations and experiments are desired to test this model.

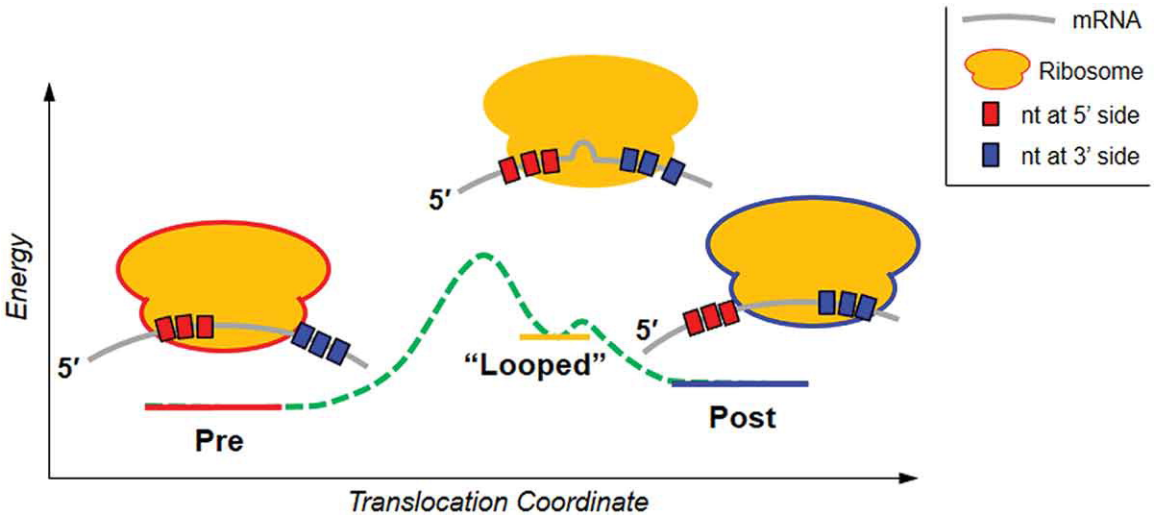

Figure 3.8 Proposed translocation mechanism based on the observed partial translocation intermediate.

3.4 Conclusions

In conclusion, a novel assay of dual DNA rulers is developed. By uniquely probing both the 3′- and 5′-ends of mRNA, an antibiotic-trapped intermediate state was observed that is consistent with a ribosomal conformation containing mRNA asymmetric partial displacements at its entry and exit sites. Based on the available ribosome structures and

computational simulations, a ‘looped’ mRNA conformation was proposed, which suggested a stepwise ‘inchworm’ mechanism for ribosomal translocation. The same ‘looped’ intermediate state identified with the dual rulers persists with a ‘-1’ frameshifting motif, indicating that the branching point of normal and frameshifting translocations occurs at a later stage of translocation.

3.5 References

1. Noller, H. F., Lancaster, L., Mohan, S. & Zhou, J. Ribosome structural dynamics in translocation: yet another functional role for ribosomal RNA. *Q. Rev. Biophys.* **50**, e12 (2017).
2. Zhou, J., Lancaster, L., Donohue, J. P. & Noller, H. F. How the ribosome hands the A-site tRNA to the P site during EF-G-catalyzed translocation. *Science* **345**, 1188–1191 (2014).
3. Ramrath, D. J. F., Lancaster, L., Sprink, T., Mielke, T., Loerke, J. *et al.* Visualization of two transfer RNAs trapped in transit during elongation factor G-mediated translocation. *Proc. Natl. Acad. Sci. U. S. A.* **110**, 20964–20969 (2013).
4. Schuwirth, B. S., Borovinskaya, M. A., Hau, C. W., Zhang, W., Vila-Sanjurjo, A. *et al.* Structures of the bacterial ribosome at 3.5 A resolution. *Science* **310**, 827–834 (2005).
5. Frank, J. & Agrawal, R. K. A ratchet-like inter-subunit reorganization of the ribosome during translocation. *Nature* **406**, 318–322 (2000).
6. Spiegel, P. C., Ermolenko, D. N. & Noller, H. F. Elongation factor G stabilizes the hybrid-state conformation of the 70S ribosome. *RNA N. Y. N* **13**, 1473–1482 (2007).
7. Woolstenhulme, C. J., Guydosh, N. R., Green, R. & Buskirk, A. R. High-precision analysis of translational pausing by ribosome profiling in bacteria lacking EFP. *Cell Rep.* **11**, 13–21 (2015).
8. Yan, S., Wen, J.-D., Bustamante, C. & Tinoco, I. Ribosome excursions during mRNA translocation mediate broad branching of frameshift pathways. *Cell* **160**, 870–881 (2015).
9. Caliskan, N., Katunin, V. I., Belardinelli, R., Peske, F. & Rodnina, M. V. Programmed –1 frameshifting by kinetic partitioning during impeded translocation. *Cell* **157**, 1619–1631 (2014).
10. Kemkhadze, K. S., Odintsov, V. B., Semenkov, Y. P. & Kirillov, S. V. Quantitative study of the interaction of aminoacyl-tRNA with the a site of Escherichia coli ribosomes: equilibrium and kinetic parameters of binding in the absence of EF-Tu factor and GTP. *FEBS Lett.* **125**, 10–14 (1981).
11. Tsai, T.-W., Yang, H., Yin, H., Xu, S. & Wang, Y. High-efficiency '-1' and '-2' ribosomal frameshiftings revealed by force spectroscopy. *ACS Chem. Biol.* **12**, 1629–1635 (2017).
12. De Silva, L., Yao, L., Wang, Y. & Xu, S. Well-defined and sequence-specific noncovalent binding forces of DNA. *J. Phys. Chem. B* **117**, 7554–7558 (2013).
13. Yao, L. & Xu, S. Long-range, high-resolution magnetic imaging of nanoparticles. *Angew. Chem. Int. Ed.* **48**, 5679–5682 (2009).

14. Hu, Q., Yang, H., Wang, Y. & Xu, S. Quantitatively resolving multivalent interactions on macroscopic scale using force spectroscopy. *Chem. Commun. Camb. Engl.* **52**, 3705–3708 (2016).
15. Qu, X., Wen, J. D., Lancaster, L., Noller, H. F., Bustamante, C. *et al.* The ribosome uses two active mechanisms to unwind messenger RNA during translation. *Nature* **475**, 118–121 (2011).
16. Peske, F., Savelsbergh, A., Katunin, V. I., Rodnina, M. V. & Wintermeyer, W. Conformational changes of the small ribosomal subunit during elongation factor G-dependent tRNA-mRNA translocation. *J. Mol. Biol.* **343**, 1183–1194 (2004).
17. Jacks, T., Power, M. D., Masiarz, F. R., Luciw, P. A., Barr, P. J. *et al.* Characterization of ribosomal frameshifting in HIV-1 gag-pol expression. *Nature* **331**, 280–283 (1988).
18. Ratje, A. H., Loerke, J., Mikolajks, A., Brunner, M., Hidebrand P. W. *et al.* Head swivel on the ribosome facilitates translocation by means of intra-subunit tRNA hybrid sites. *Nature* **468**, 713–716 (2010).
19. Brunelle, J. L., Youngman, E. M., Sharma, D. & Green, R. The interaction between C75 of tRNA and the A loop of the ribosome stimulates peptidyl transferase activity. *RNA N. Y. N* **12**, 33–39 (2006).
20. Samaha, R. R., Green, R. & Noller, H. F. A base pair between tRNA and 23S rRNA in the peptidyl transferase centre of the ribosome. *Nature* **377**, 309–314 (1995).
21. Belardinelli, R. & Rodnina, M. V. Effect of fusidic acid on the kinetics of molecular motions during EF-G-induced translocation on the ribosome. *Sci. Rep.* **7**, 10536 (2017).
22. Kurkcuoglu, O., Doruker, P., Sen, T. Z., Kloczkowski, A. & Jernigan, R. L. The ribosome structure controls and directs mRNA entry, translocation and exit dynamics. *Phys. Biol.* **5**, 046005 (2008).
23. Nguyen, K. & Whitford, P. C. Capturing transition states for tRNA hybrid-state formation in the ribosome. *J. Phys. Chem. B* **120**, 8768–8775 (2016).
24. Yao, L., Li, Y., Tsai, T.-W., Xu, S. & Wang, Y. Noninvasive measurement of the mechanical force generated by motor protein EF-G during ribosome translocation. *Angew Chem*. *Int. Ed.* **52**, 14041-14044 (2013).

Chapter 4 Modulation and Visualization of EF-G Power Stroke during Ribosomal Translocation

4.1 Introduction

The ribosome translates mRNA into peptides processively. In contrast to many transport motor proteins with fluctuating step sizes, it moves on the mRNA by exactly three nucleotides (nt) per step.[1] Otherwise the codon contents will be altered, which is accumulative to all downstream codons, resulting in incorrect peptides. Therefore, ribosomal translocation on the mRNA is unique and vital to cell survival. The translocation process can be described as the following steps. First, the peptide elongation cycle starts with the aminoacyl tRNA binding to the ribosomal A-site. Then the amino acid forms peptide bond with the peptidyl chain that is held at the P-site tRNA. Consequently, the peptidyl chain becomes one amino acid longer and is transferred to the A-site tRNA. Then the tRNAs move from the P- and A-sites to E- and P-sites, respectively, leaving a vacant A-site for the next cycle. Overall, translocation involves large-scale ribosome conformational changes and extensive tRNA-ribosome interaction reorganization.

The mechanism for the precise control of the translocation step is unclear. The ribosome can translocate spontaneously at an extremely slow rate of $\sim 5\times10^{-4}$ s^{-1}.[2] With GTP hydrolysis and the translocase EF-G, the rate is improved by approximately 50,000 fold to 25 s^{-1}, which is comparable for the rate of protein synthesis *in vivo*. There are two possible mechanisms for EF-G catalysis: the Brownian motor model and the power stroke model.[3] The key difference between the two models is whether a substantial mechanical

force, termed as power stroke, is generated. In the Brownian motor model, EF-G utilizes the GTP energy to bind tightly to the A-site after A-site tRNA diffuses to the P-site. The driving force is thermal fluctuation; no mechanical force is generated. In the power stroke model, however, the EF-G generates a burst of force via GTP hydrolysis that pushes the A-site tRNA to move towards the P-site. The ribosome structure trapped with both A-site tRNA and EF-G showed that while the P-site tRNA moved the same distance as the ribosome inter-subunit ratcheting and head swiveling would have generated, the A-site tRNA moved more and maintained tight contact with EF-G. This intermediate state was consistent with an active power stroke model.[4] Another structural study revealed an unusually compact EF-G structure bound with the pre-translocation ribosome.[5] Compared to the extended conformation on the post-translocation ribosome, the catalytic domain IV of EF-G must move by approximately 100 Å during translocation. This large conformational change is also consistent with the formation of force because average thermal fluctuations can only lead to short distance movements (< 1 Å) due to the large viscous dragging force of solution.[6] Thermal energy-driven movements of 100 Å are possible but extremely rare to be compatible with the 25 s^{-1} turnover numbers of EF-G. However, structural studies alone cannot provide the amplitude of power stroke.

Three different methods have been used to quantify the power stroke with different results, none of which has established correlation between power stroke and structural changes of EF-G.[7–9] Using a series of DNA-mRNA duplexes as the force rulers, we determined the EF-G power stroke to be 89±11 pN.[7] The critical dissociation force of the duplexes were obtained by force-induced remnant magnetization spectroscopy (FIRMS)[10].

Because shear rupture of DNA duplexes into separate single strands exhibited cooperative dissociation with a sharp transition, they have been used reference systems for force measurements.[11–13] Liu and co-workers used optical tweezers and determined the power stroke to be approximately 13 pN.[8] Chen and colleagues used an indirect method to deduce the power stroke.[9] However, it remains unknown whether the EF-G force plays a role in controlling the precise 3-nt stepping of ribosome, or whether the force can be varied by structural modifications or other factors. In addition, because different techniques produced inconsistent power stroke values, a more straightforward detection method will be beneficial to the precise quantification of power stroke and to measure the widely occurring force generation in the cell.

Here, we report that the EF-G power stroke can be changed by internal crosslinking and antibiotics binding. We also report a new microscope-based technique to measure the power stroke, which is more straightforward and easier to implement than the previous magnetic-based approach. Both techniques produced similar results. Furthermore, we reveal for the first time that a smaller power stroke only induced a lower translocation yield and did not affect translocation fidelity. These new discoveries confirmed the substantial power stroke accompanying EF-G catalysis that we previously determined, and indicated precise mRNA translocation is achieved by the ribosome itself.

4.2 Experimental section

4.2.1 Materials

The Bis-Maleimide -$(PEG)_6$ and -$(PEG)_{11}$ were from BroadPharm. Act Thiol Sepharose® 4B was from GE Healthcare LifeSciences. Maleimide Mag Beads were from Ocean Nanotech. Streptavidin-conjugated magnetic beads were purchased from Thermo Fisher (Dynabeads M-280). All other reagents were from Sigma.

The FPLC binding buffer contains: 50 mM Tris-pH 7.8, 300 mM NaCl. The FPLC elution buffer is the same as the binding buffer except with 1 M of imidazole. The protein storage buffer contains: 20 mM Tris-pH 7.5, 10 mM $MgCl_2$, 0.5 mM EDTA, 4 mM BME (2-mercaptoethanol), 40 mM KCl. The PBS (pH 7.4) buffer contains: 137 mM NaCl, 2.7 mM KCl, 8 mM Na_2HPO_4, and 2 mM KH_2PO_4. The electro elution upper tank buffer contains: 375 mM Tris (no need to pH), 192 mM Glycine, 0.2% SDS. The lower tank buffer contains: 50 mM MOPS-pH 7.2, 1 mM EDTA. The TAM_{10} buffer contains: 20 mM tris-HCl (pH 7.5), 10 mM Mg $(OAc)_2$, 30 mM NH_4Cl, 70 mM KCl, 5 mM EDTA, and 7 mM BME (2-mercaptoethanol), and 0.05% Tween 20.

The bi-cys mutants were introduced via the “GeneArt Site-Directed Mutagenesis PLUS” kit (Thermo Fisher). The F411C-Y535C double mutated EF-G was transformed and expressed in BL21(DE3)pLysE cell (Thermofisher), and purified with Histrap HP 5 ml column on an Akta Purifier FPLC instrument with imidazole gradients (GE Healthcare Life Sciences). The His-tagged protein eluted around 200 mM imidazole.

All nucleic acids were purchased from Integrated DNA Technologies. The mRNA sequence was 3′-C**UC AAG UCG UCA UCU AAA** U*GC AAA AUU GUA AAA AUA AAG GAA AAA U*UA AAU UAA AUU AAU UGU CAA C /TEGBio/-5′. TEG: an 18-atom spacer; Bio: biotin (Integrated DNA Technologies). The bold section was complementary to the ruler DNAs; the italic section was covered by the ribosome during power stroke measurement; the underscored section was used to hybridize with the DNA on the magnetic beads. The ruler DNAs were 5′-/BioTEG/CTC AAG T**GC AGT AGA TTT**-3′, 5′-/BioTEG/CTC AAG **AGC AGT AGA TTT**-3′, 5′-/BioTEG/CTC AA**C AGC AGT AGA TTT**-3′, 5′-/BioTEG/CTC A**TC AGC AGT AGA TTT**-3′, 5′-/BioTEG/CTC **TTC AGC AGT AGA TTT**-3′, 5′-/BioTEG/CT**G TTC AGC AGT AGA TTT**-3′, and 5′-/BioTEG/C**AG TTC AGC AGT AGA TTT**-3′. They would form 11-17 bp duplexes with the exposed mRNA, respectively. The bold nucleotides were complementary to the bold ones on the mRNA. The DNA used for conjugating the magnetic beads with the 5′-end of the mRNA was 5′-TTA ATT TAA TTA ACA GTT GT_{30} /TEGBio/-3′. The underscored nucleotides were complementary to the underscored ones on the mRNA. To study translocation efficiency, the probing DNA was 5′-/BioTEG/GGG CTC A**TC AGC AGT AGA TTT A**-3′.

4.2.2 Electrophoresis

For Tris-Gly PAGE or native gel, the Bio-Rad Mini-PROTEAN Tetra Cell, Model 491 Prep Cell, and Mini-PROTEAN 3 Multi-Casting Chamber or hand cast system were used. The electroelution was conducted with the Bio-Rad Model 422 Electro-Eluter. All the PAGE reagents were from Bio-Rad. The Novex™ Sharp Pre-stained Protein Standard

and Precision Plus Protein™ Kaleidoscope™ Prestained Protein Standard were from Thermo Fisher and Bio-Rad, respectively.

4.2.3 EF-G mutants and crosslinking

The cysteineless EF-G cloned in pET24b was introduced with two cysteine mutations at the Phe411 and Tyr535 (*e. coli.* sequence) positions via the "GeneArt Site-Directed Mutagenesis PLUS" kit (Thermo Fisher). The F411C-Y535C double mutated EF-G was transformed and expressed in BL21(DE3)pLysE cell (Thermo Fisher), and purified with Histrap HP 5 ml column on a Akta Purifier FPLC instrument with gradients (GE Healthcare Life Sciences). The His-tagged protein eluted around 200 mM imidazole. The protein was concentrated with AmiconUltra centrifugal filters (Millipore), and buffer-exchanged into the storage buffer via Nap25 desalting column (GE Healthcare Life Sciences). The protein concentration was measured at 260 nm with extinction coefficient of 600,000 cm^{-1} M^{-1}.

The first step of the corsslinking reaction was to reduce the di-sulfhydryl groups via 2-folds of TCEP (Sigma) at rt for 30 min. Higher TECP caused protein precipitation, which was not recommended. Then the TCEP was removed via buffer exchange with PBS buffer without any free thiol group. The bis-maleimide functionalized crosslinkers were dissolved in DMSO to form 20 mM stock solution, then added at 2-fold excess to the protein and reacted at rt for 1 h. The excess crosslinkers were then removed by Nap10 desalting column (GE Healthcare Life Sciences) with PBS buffer, and the reaction mixture was subject to either PAGE, or sepharose gel or magnetic beads purifications.

4.2.4 Preparative separation of CL EF-G with PAGE

CL EF-G and un-crosslinked EF-G were separated with the Bio-Rad Model 491. Because of the very close R_f values of the two bands, only 300-400 pmol of total protein was loaded. The eluted fractions (6 ml/fraction) were concentrated and ran on analytical gel. After approximately 10 h, the two bands were eluted with reasonable separation. The separated aliquots were pooled and concentrated. The CL EF-G fraction was of 70% purity, while the un-crosslinked EF-G was of 80% purity. Because of the long running time, this direct elution method is not practical to generate large amount of pure CL EF-G.

We then tried electroelution after manually incising the protein bands. The mini-Gel running time was 10 times less than the Bio-Rad 491 cylindrical gel (45 min at 200 V), and protein was eluted into 400 μL volume that was sealed with dialysis membrane, using Bio-Rad Model 422. The elution was approximately 3 h with 10 mA per elution tube. Each elution process consumed incised bands from 12 mini gels that were run in parallel, obtained around 200 pmol of CL EF-G after elution. The SDS was removed by using the lower tank buffer without SDS, followed by buffer exchange to protein storage buffer. Although this method was tedious and difficult to scale up, it was sufficient for mass spectrometry analysis and power stroke study.

4.2.5 Preparative separation of CL EF-G with gel binding

Two cysteine-binding gels were used. For act thiol gel binding: 0.25 g of the dried sepharose powder was swelled with PBS buffer to 1 mL. Additional buffer was added to transfer the slurry into a Bio-Rad Mini Bio-Spin Column. The liquid phase was drained at

100 rpm (revolution per minute) for 30 sec to 1 min in a micro centrifuge. Faster or longer spinning could dry the matrix, which should be avoided. The gel was washed with approximately 5 mL of buffer, or until the elution read near "0" at 260 nm on a spectrophotometer. 1 nmol of protein mixture in less than 400 μL was loaded on the column. The solution was allowed to fully enter the gel bed, and then the column was capped at both ends. The binding was incubated at 30 °C for varied time, and the protein was eluted with 5 mL of PBS buffer. The elution was concentrated to 100-200 μL, and 1/9 volume of 10× protein storage buffer was added. The protein concentration was measured with spectrophotometer at 260 nm, and the purity was checked with PAGE. For magnetic beads binding: 50 mg of dried magnetic beads were washed with PBS buffer. The beads were pulled down with a magnetic separator (Thermo Fisher). And the supernatant was drained. The washing step was repeated until the reading at 260 nm was "0". 1 nmol of the protein mixture in 400 μL was incubated with the beads at rt for varied time. The beads were separated via the magnetic separator. 1/9 volume of 10× protein storage buffer was added and the protein was concentrated to 100-200 μL. The concentration was measured with spectrophotometer at 260 nm, and the purity was checked with PAGE.

4.2.6 Tryptic digestion and mass spectrometry analysis

The crosslinked EF-G was confirmed by mass spectrometry after tryptic digestion of the incised lower band, using In-Gel Tryptic Digestion Kit (Thermo Fisher). Analysis was carried out at the Mass Spectrometry Laboratory at the University of Houston, using HPLC-MS. The HPLC instrument was NanoElute (Bruker). The mass spectrometer was

timsTOF Pro (Bruker), with PASEF default method. The data analysis software was Peaks Studio 8.5. The sample concentration of CL6 was approximately 0.11 μg/40 μL.

4.2.7 Formation of ribosome complexes

All the mixtures were in TAM_{10} buffer. Three mixtures were prepared: the ribosome mix, Tu0G mix, Leu mix. The ribosome mix contains 1 μM ribosome, 1.5 μM each of IF1, IF2, IF3, 2 μM of mRNA coding for "ML" at the first 2 codons, 4 μM of charged fMet-$tRNA^{fMet}$, and 4 mM of GTP. The Tu0G mix contained no EF-G but all the other components in the TuWG mix. The Leu mix contained 100 mM Tris (pH 7.8), 20 mM $MgAc_2$, 1 mM EDTA, 4 mM ATP, 7 mM 2-merchaptoethanol, 0.1 mg/mL total synthetase, 50 A_{260}/mL total tRNA, and 0.25 mM leucine. These mixtures were incubated at 37 ^oC for 25 min, separately. The ML-Pre complex was formed by incubating the ribosome mix, Tu0G mix and Leu mix in the volume ratio of 1:2:2, at 37 ^oC for 2 min. The resulting ribosome complex was added on 1.1 M sucrose cushion and purified by ultra-centrifuge.

4.2.8 Poly(Phe) assay

Three mixtures were made. (1) The IC mixture contained 1μM ribosomes, 5 μg/μL poly(U) and 2 μM N-acetyl phenylalanine-$tRNA^{Phe}$ in TAM_{10} buffer; (2) the TuMaster mixture contained 3 μM EF-Tu, 4 μM EF-Ts, 0.5 mM GTP, 0.5 mM PEP and 0.006 mg/ml pyruvate kinase in TAM_{10} buffer. Individual EF-G assay solution contained the TuMaster ingredients and 2 μM specific EF-G; (3) The A mixture contained 100 mM Tris (pH 7.5), 20 mM $MgAc_2$, 1 mM EDTA, 4 mM ATP, 7 mM 2-mercaptoetanol, 33 μg/mL purified

$tRNA^{phe}$ aminoacyl synthetase, 50 μM ^{14}C labeled phenylalanine (1100 dpm/pmol) and 5 μM $tRNA^{phe}$.

All three mixtures were incubated separately at 37 ºC for 25 min. Then 15 μL of the ribosome mixture, 15 μL of A mixture and 28 μL of EF-G mixture were gently mixed together at 37 ºC. At 15 s, 30 s, 1 min, 5 min, 8 μL Poly(Phe) aliquot was drawn into 0.5 mL ice-cold 10% TCA. The TCA solutions were boiled at 90 ºC for 10 min and cooled on ice for 30 min. The TCA solutions were then filtered with nitrocellulose filters (Millipore). Each filter was washed with 6 mL ice-cold TCA solution and air dried. The radioactivity of the synthesized poly-phenylalanine on each filter was counted with a scintillation counter.

4.2.9 Power stroke by magnetic detection

A sample well with dimensions of 4×3×2 mm^3 (L×W×D) was glued with a piece of biotin-coated glass on the bottom surface. Aqueous solution of 20 μL 0.25 mg/mL streptavidin was loaded into the sample well and incubated for 40 min. Then the sample well was rinsed twice with TAM_{10} buffer. 20 μL of 1 μM biotinylated probing DNA strand was added and incubate for 1hr. After rinsing twice with TAM_{10} buffer, 20 μL of 0.1 μM ribosome complexes were immobilized on the surface via DNA-mRNA interaction and incubated for 1.5 h.

The magnetic beads were incubated with long DNA strand (containing 19 complementary bases with the mRNA) at room temperature for 1 h. A Vortex shaker was used to enhance conjugation. Each initial volume was 1 μL. The initial DNA concentration

was 100 μM. The mixture was diluted to 100 μL by TAM10 buffer, so the final concentration of the magnetic beads was approximately 3.2×10^7 particle/mL. Excess DNA was washed away by buffer three times. The DNA-conjugated beads were then introduced into the sample well and incubated for another 1.5 h. Nonspecifically bound magnetic particles were removed from the surface by applying centrifugal force at1000 rpm (revolution per minute) for 2 min. The magnetic signal of the samples was measured by a home-built atomic magnetometer. Percentages of remnant magnetic beads were obtained by dividing the magnetic signal after EF-G by the signal before the EF-G. The percentages were normalized to 100% for the strongest ruler (17 bp) and 0% for the weakest ruler (11 bp). Typical error was ±5%. All experiments were repeated to ensure the reproducibility of the percentage profile, based on which power stroke was extracted.

4.2.10 Power stroke by microscope detection

The sample preparation was the same as in magnetic detection, except the density of magnetic beads was reduced to approximately 6.5×10^6 particle/mL to facilitate particle counting. For each sample well, six images were captured using a 20× objective with an inverted microscope (Amscope, Model ME1400TC). The dimensions of each image were 4098×3288 pixels, equivalent to 0.215 mm^2 in area. Subsequently, 2 μL of solution (20 μM EF-G, 4 mM GTP, 4 mM PEP, 0.2 mg/mL PK) in TAM_{10} buffer was added into the sample well and incubated for 20 min at 37 ^oC. Both CL6 and CL11 had the same concentration as the WT EF-G. For the fusidic acid experiment, fusidic acid at 2.5 mM was incubated with WT EF-G before adding onto the surface. The nonspecifically bound magnetic particles were removed from the surface by applying centrifugal force at 1000

rpm for 2 min. Then another six images were captured for the same sample well. The position of the sample well was maintained the same between before and after adding EF-G by using a high-resolution motor (Thorlabs Z725B, resolution: 40 nm). The number of particles on each image was counted by ImageJ. The decreasing percentage was calculated by averaging the six images, and scaled to 100% for the strongest ruler (17 bp) and to 0% for the weakest ruler (11 bp). Typical error in percentage was ±7-8%, which was greater than that of magnetic detection. Surface inhomogeneity was probably one of the main reasons for the error.

4.2.11 Translocation efficiency by FIRMS

Magnetic signal of the samples was measured by an atomic magnetometer as a function of mechanical forces. The atomic magnetometer had a sensitivity of ~200 $fT/(Hz)^{1/2}$. The force was provided by a centrifuge (Eppendorf, Model 5427R). The dissociation of the DNA-mRNA duplexes was indicated by a decrease in the magnetic signal, which occurred when the centrifugal force reached the dissociation force of the DNA-mRNA duplex. The typical force range in this work was 90 pN, after which the residual magnetic signal was taken as the background. FIRMS profiles were obtained by normalizing the overall magnetic signal decrease (B_0) to be 100% and then plotting the relative magnetic signal decrease (B/B_0) vs. the external force. The force values were calculated according to $m\omega^2 r$, in which m is the buoyant mass of M280 magnetic beads (4.6×10^{-15} kg), ω is the centrifugal speed, and r is the distance of the magnetic beads from the rotor axis (7.5 cm for 5427R). The typical force resolution was 3-4 pN in this work. Each profile reported in this work was repeated at least three times to ensure reproducibility.

4.3 Results

4.3.1 Preparation and functional assay of crosslinked EF-G

Two cysteines were introduced at the Phe411 and Tyr535 positions (*E. coli.* sequence) to the cysteine-less EF-G sequence in pET24b.[14] The distances between these two residues were 18.3 and 34.8 Å in the pre- and post-translocation complexes, respectively, in the recent structures of 4WPO/4WQF (Figure 4.1a)[5]. Earlier ribosome-bound EF-G (2WRI) and free EF-G (2BM0) structures indicated the distances between these two residues were 17.5 and 37.4 Å, respectively (Figure 4.2).[15,16] The bifunctional crosslinkers were maleimide-$(PEG)_n$-maleimide, with lengths of 27 and 43 Å, for n = 6 and 11, respectively. After coupling reaction with the two cysteine residues, the crosslinker $(PEG)_6$ would restrict the extended EF-G conformation, while $(PEG)_{11}$ would not. The crosslinked EF-G was distinguishable from the un-crosslinked ones via 5% PAGE after being enriched by four different methods (Figures 4.1b to e, top band, crosslinked; bottom band: un-crosslinked). Figure 4.1b shows the enrichment with Bio-Rad 491 model. The proteins separated on a cylindrical gel were eluted out of the gel and pumped out from the small reservoir confined by dialysis membrane. The fractions were concentrated and analyzed via PAGE. The bottom band was eluted out first, followed by the mixture of both bands, and finally the top band was eluted. Because of the very close R_f values of these proteins (0.74 for un-crosslinked and 0.77 for crosslinked), every 10 h/gel separation only yielded less than 200 pmol of pure protein. We improved the efficiency via batches of mini-gel separation followed by manual incision and electro-elution (Bio-Rad, Model 422, Figure 4.1c). Alternatively, to avoid SDS in PAGE gels, the crosslinked EF-G was purified

via chemical reactions with sulfhydryl reactive beads, such as maleimide-coated magnetic beads (Figure 4.1d) and iodoacetyl gel (Figure 4.1e). Because the crosslinked EF-G could not react with the beads, it was eluted out of the matrix free of un-crosslinked EF-G. Crosslinked EF-G purified with magnetic beads reached more than 90% purity without any SDS, which was used for the biophysical measurements in this work.

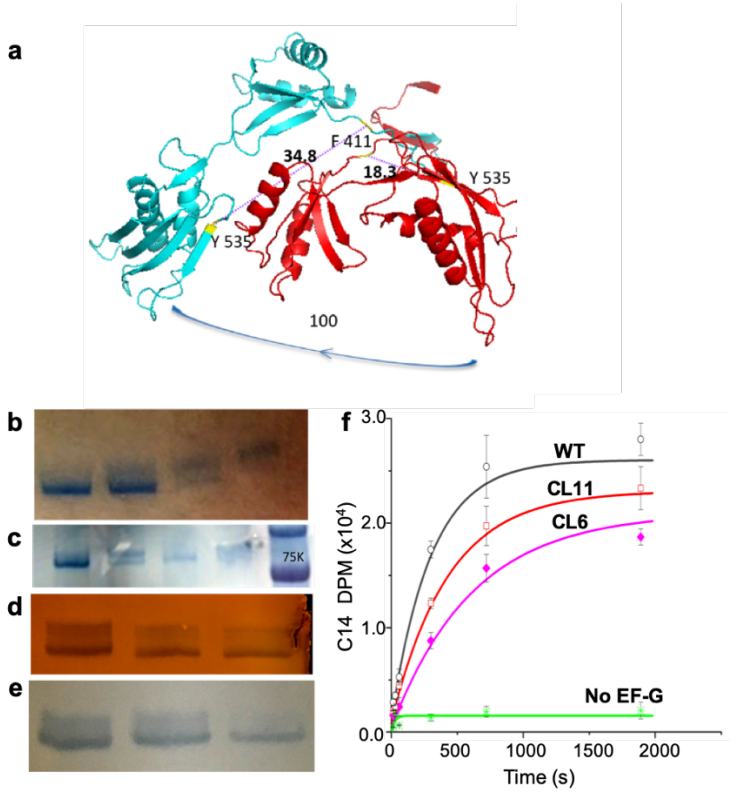

Figure 4.1 Design, purification, and activity assay of crosslinked EF-Gs. **(a)** Crosslinking residues F411 and Y535 (bacterial numbering). **(b)** Separation by Bio-Rad Model 491. Lanes 1 and 4: pure lower and upper bands, respectively; lanes 2 and 3: the transitions from one component to the other. Lanes are numbered from left to right. **(c)** Purification by mini-gel and hand-incision, followed by Bio-Rad Model 422 elution. Lanes 1 and 3: purified CL EF-G with different quantities; lane 2: mixture of un-crosslinked and crosslinked; lane 4: purified un-crosslinked EF-G; lane 5: marker. **(d)** Purification by activated thiol sepharose 4B. Lanes 1-3 were analyzed after 1 hr, 4 hr, and overnight incubation time with the beads, respectively. The final purify was approximately 70%. **(e)** Purification by maleimide-activated magnetic beads. Lanes 1-3 were analyzed after 1, 2 and 3 hr of incubation time, respectively. The final purity was > 90%. **(f)** Radioactivity in dpm unit by Poly(Phe) assay for the WT and two crosslinked EF-Gs.

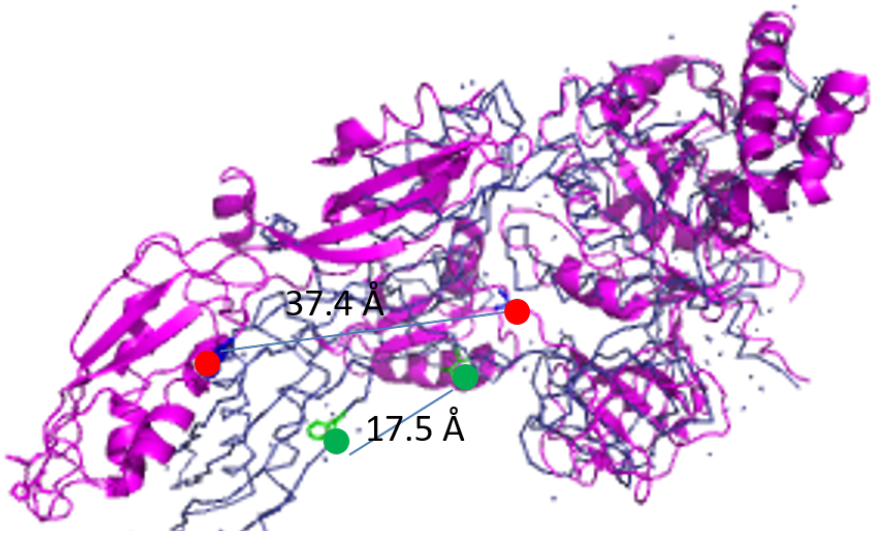

Figure 4.2 Overlay of ribosome-bound EF-G (2WRI, purple) and free EF-G (2BM0, blue) structures. Related to Figure 4.1. The distance between F411 and Y535 was 37.4 Å (red dots) and 17.5 Å (green dots), respectively.

The proper crosslinking was verified by mass spectrometry after PAGE separation and in-gel tryptic digestion (Figure 4.3). The activities of these EF-Gs were measured with the conventional Poly(Phe) assay.[17] Figure 4.1F shows that in the fast phase of Poly(Phe) synthesis, the rates were in the order of WT > CL11 > CL6 (the $(PEG)_n$ crosslinked EF-Gs were denoted as CL6 and CL11 for n = 6 and 11, respectively. Extrapolation of the slow phase of the traces suggested that the asymptotic plateaus reached less level for the modified EF-Gs than that of the WT, indicating that other properties of the EF-G changed in addition to the effect on kinetics. These experiments demonstrated that conformational restriction would diminish but not completely inhibit the EF-G catalysis on the Poly(Phe) synthesis.

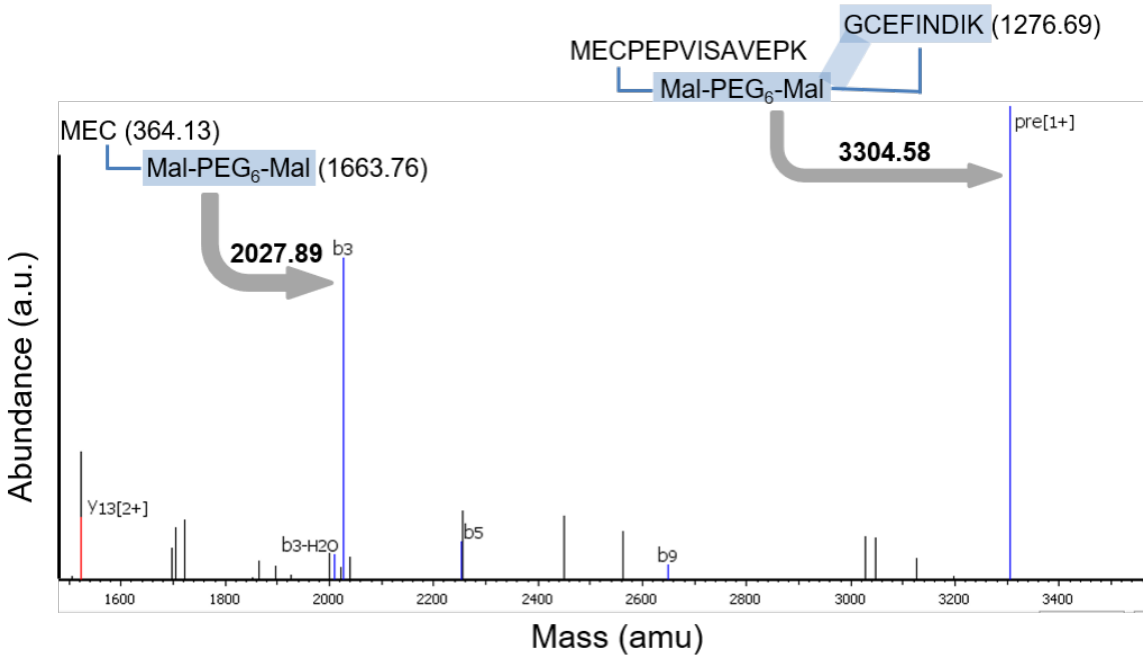

Figure 4.3 Mass spectrum of the lower band after incision and in-gel tryptic digestion for CL6. Related to Figure 4.1. The molecular ion peak was at 3304.58 amu, which equals to the molecular weight sum of the two Cys-containing peptides plus the linker bis-mal-$(PEG)_6$ (right inset scheme). A major fragment at 2027.89 amu was due to the sum of one peptide and the linker (left inset scheme). All other major fragments were also consistent with this assignment.

4.3.2 DNA-mRNA force rulers to determine the power stroke

The experimental approach for detecting the power stroke is shown in Figure 4.4a. A series of DNA-mRNA duplexes with 11-17 basepairs (bp) were constructed and immobilized on the surface via biotin-streptavidin interaction, to serve as the force rulers.[7] Magnetic beads were conjugated with the ribosome complex on the 5′-end of the mRNA via an excessively long (19 bp) duplex between the DNA on the beads and the mRNA. The power stroke generated by EF-G would dissociate the ruler DNA-mRNA duplex if it exceeded the critical force of the duplex, which would result in a significant decrease in the magnetic signal of the sample. Otherwise there would be no significant signal change

because the magnetic beads would remain immobilized on the surface. The magnetic signal was detected by an atomic magnetometer reported previously.[7]

The critical forces of the DNA-mRNA rulers were determined by FIRMS, in which a centrifugal force was applied to induce dissociation.[10] The dissociation was indicated by a sharp decrease in the magnetic signal when the centrifugal force reached the duplex's critical force. Typical FIRMS results for the 13-17 bp duplexes have been obtained previously which cover the force range of this work. Shown in Figure 4.5a, the experimental data were fitted with the prevalent Bell's formula (Equations 1 and 2), in which one transition state was postulated.[18–20]

$$k(f) = k(0) * e^{\frac{f*(n-n0)*\delta}{K_B T}} \quad (1)$$

$$k(0) = A * e^{-\frac{(n-n1)*G^{\neq}}{K_B T}} \quad (2)$$

In this model, the work of applying a shearing force (f) for a distance (δ) contributes to lower the activation energy barrier ($G^{\neq}$). Assuming a linear relationship of both terms with respect to the bp number of the duplex (denoted as n), Equation 1 was deduced. Here, terms n_0 and n_1 were implemented to account for the offset from zero in linear regression fitting. Equation 1 predicted that the dissociation of a duplex is abrupt, regardless of the force exertion time. The fitted $G^{\neq}$ and δ were 3.44 kcal/mol and 0.15 nm, which were within twofold variation with abundant literature estimations.[21–26] Therefore, our experimental data agreed well with the theoretical model for force-induced dissociation.

The time dependence of the mRNA-DNA dissociation (D_t) obeys single-exponential decay:

$$D_t = D_0 * e^{-k(f)*t} \quad (3)$$

Because time is a parameter in the kinetics fitting, the effect of centrifugal duration was simulated on the experimental data of 15 bp duplex dissociation. As shown in Figure 4.5a, the best fit of the experimental data yielded an A*t value of 10^{11} for 5 min centrifugal time. This value varied from 10^9 to 10^{13} when a hypothetic centrifugal time changed from 0.05 min to 500 min. Interestingly, although the critical force varied by 16 pN, the sharp transition behavior hardly changed (Fig 4.5b). This analysis indicated that for ±100 folds of force duration variations, the dissociation force would only change ±8 pN. Therefore, the DNA-mRNA duplexes are robust force rulers for determining the power stroke. In addition, the relationship between critical force and bp value follows an approximately linear function. As shown in Figure 4.5c, the relationship of force to n showed a linear relationship ($R^2 = 0.987$), which was consistent with the literature.[27]

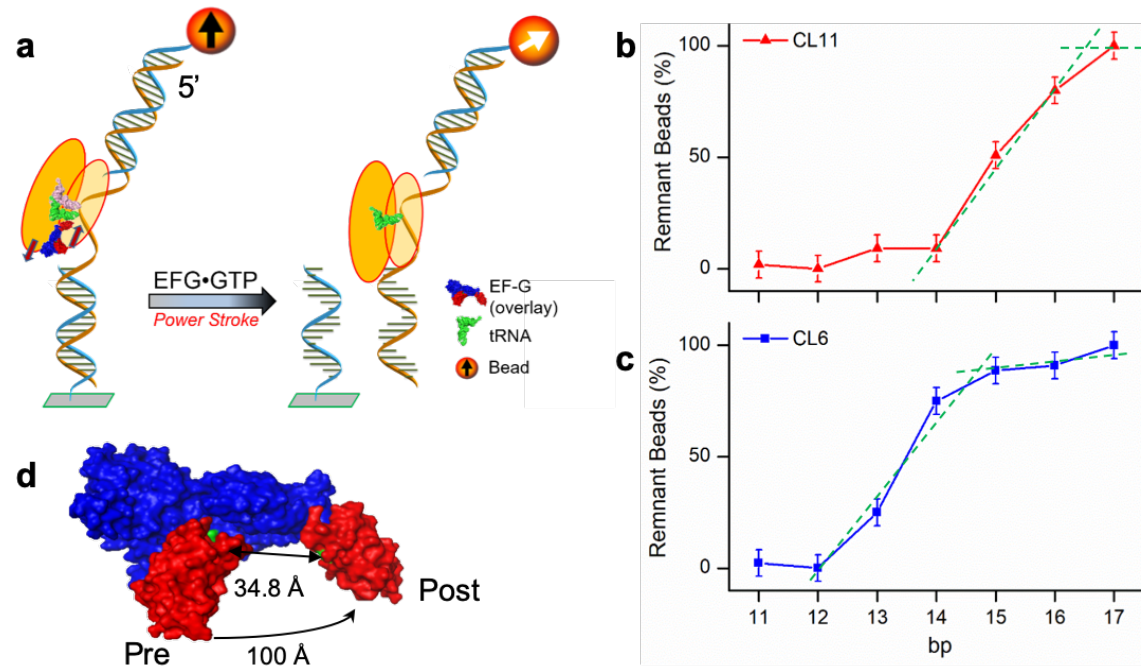

Figure 4.4 Magnetic method for measuring the power stroke of crosslinked EF-Gs. **(a)** Schematic of using DNA-mRNA duplexes as force rulers and magnetic labeling to determine the power stroke. The equal and opposite forces are reminiscent to myosin-actin interaction. **(b)** Plot of remnant magnetic beads vs. duplex length for CL11. **(c)** Plot of remnant magnetic beads vs. duplex length for CL6. **(d)** Overlay of EF-G structures before and after translocation to indicate the extraordinary conformational changes. Red: domain IV; blue: the rest domains.

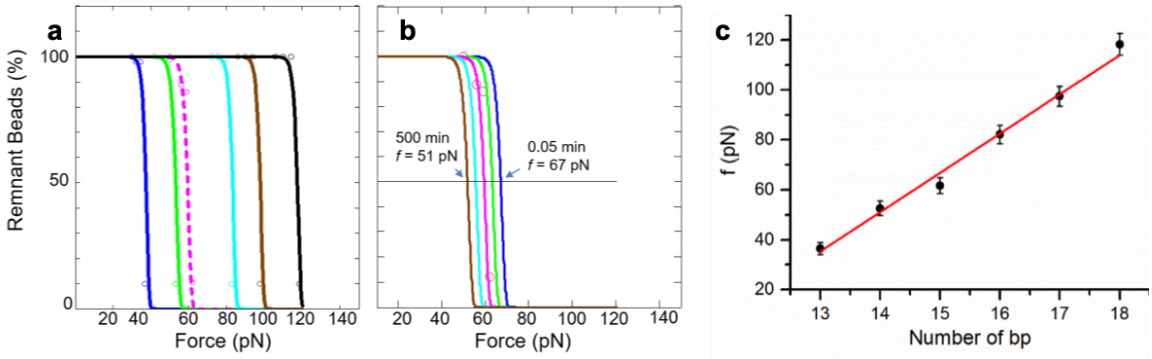

Figure 4.5 Validation and calibration of the DNA-mRNA duplexes as force rulers. **(a)** Theoretical fitting of the force calibration with the Bell's formula (Equation 1 in the main text). **(b)** Simulation of debinding curves of the 15-bp duplexes with ± 100 folds of centrifugal time. The experimental critical force was 65 pN. **(c)** The linear corrlation of the critical forces to the number of bp of duplexes.

4.3.3 Magnetic measurements of the power stroke of crosslinked EF-Gs

The ribosome pre-translocation complex, which carried vacant $tRNA^{fmet}$ and ML-$tRNA^{Leu}$ at the P- and A-sites, respectively, was tethered to the surface via the DNA-mRNA duplex at the 3′-end of the mRNA. Translocation was induced by addition of EF-G•GTP to a final concentration of 2 μM and incubated at 37°C for 20 min. Only one round of power stroke was generated because no free tRNAs and other components were present.

Upon GTP hydrolysis by CL11 and CL6, the EF-Gs exerted force on the A-site tRNA, which chelated to the mRNA via codon-anticodon interaction.[4,16] This force moved the two tRNAs and mRNA together toward the direction of 5'-terminal. Although the actual geometry differed, these interactions and motions were reminiscent to myosin or kinesin motors moving on their tracks while carrying the polystyrene beads.[28,29] EF-G, ribosome and mRNA resembled myosin, polystyrene bead and actin filaments, respectively. The binding of EF-G to the ribosome resembled the interaction of myosin and the bead. In addition, the myosin lever arm tilting resembled the large conformational change of EF-G domain IV.

While the actin filaments were deposited on the surface, the mRNA was suspended in the solution and tethered to the surface via mRNA-DNA duplex as showed in Figure 4.4A. The EF-G power stroke exerted on the tRNA also sheared on the mRNA-DNA duplex, as showed by the arrow in Figure 4.4A. This is similar to the force myosin exerted on its track while moving the bead along the actin filament. For mRNA-DNA duplex, it will dissociate if the force exceeds the duplex's critical force. Consequently, the ribosome

complex is detached from the surface, causing the magnetic signal to decrease as described before.[7] On the other hand, the EF-G bound ribosome experienced equal opposite force from the tRNA, and moved toward the 3'-terminal of the mRNA, similar to the bead movement in the myosin experiments.

Because same EF-G species exerted similar magnitude of force, longer force rulers will be dissociated to a less percentage in comparison to the shorter ones, resulting in higher remnant magnetic beads. As shown in Figure 4.4B for CL11, the largest n with a substantial signal decrease was 16, indicating the power stroke to be in between the critical forces of the 16- and 17-bp duplexes. This result was similar to that of WT EF-G that we studied previously using the same method.[7] To systematically reveal the power stroke, we used the onset of the slope for the signal decrease (the green dashed lines in Figure 2B), a method commonly used in mechanical and thermal analyses.[30,31] This approach yielded that n = 16.5 was the starting point of duplex dissociation by CL11. Therefore, the power stroke of CL11 was determined to be 90±8 pN, the same as that of WT EF-G.[7] The uncertainty was estimated as half of the force difference between n = 16 and 17. This result showed that the $(PEG)_{11}$ linker did not significantly affect the EF-G power stroke.

For CL6, however, the first decrease occurred at n = 14; no significant change was observed for n = 15, 16, and 17 (Figure 4.4C). This result showed that the power stroke of CL6 was much reduced compared to those of CL11 and WT, with the value between 52 and 62 pN according to the forces of the 14- and 15-bp duplexes, respectively. Analysis of the onset of slope gave n = 14.7 (green dashed lines). Therefore, the power stroke of CL6 was 59±5 pN. This result indicated that because the short $(PEG)_6$ linker restricted the

extension between the EF-G domains III and IV (Figure 4.4D), the power stroke was significantly reduced.

4.3.4 Microscope detection of EF-G power stroke

Our method of using force rulers to determine power stroke can also be combined with a microscope instead of an atomic magnetometer. The microscopic images will more straightforwardly visualize the effect of power stroke. The resulting method is simpler to implement compared to the FIRMS method, because it does not involve highly specialized sensors. To facilitate particle counting, the concentration of the magnetic beads was reduced to 1/5 of that in magnetic detection (Supporting Information). The number of magnetic beads before and after the exertion of power stroke was counted using ImageJ,[32] instead of being detected as an overall magnetic signal by the atomic magnetometer. Figure 4.6 shows the microscope images of the sample surfaces of different DNA-mRNA rulers for CL6, CL11, and WT EF-G. For each sample, images before and after the addition of corresponding EF-G were taken using a 20× objective. The images shown in Figure 4.6 were 1/16 of the whole images, while the whole images were used for particle counting. The dimensions of each whole image were 0.518×0.416 mm^2. The images showed that for CL6, the bead density clearly dropped for up to n = 14, whereas for CL11 and WT, up to n = 16 was dissociated. The particle disappearance here was the same as the magnetic signal decrease in the magnetic detection method. The visual difference in the images was sufficient to reveal the order of power stroke for the three EF-Gs.

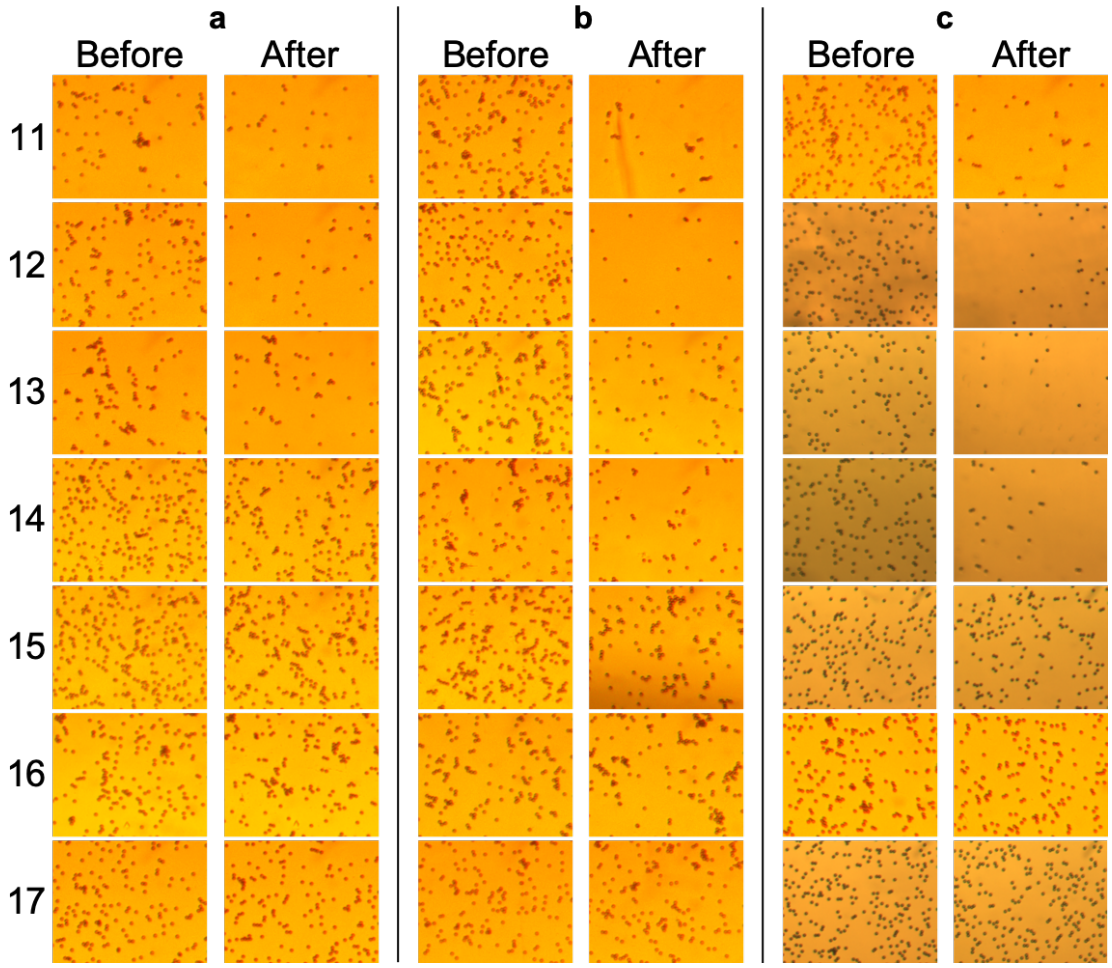

Figure 4.6 Microscope images for determining the power stroke of crosslinked and wild-type EF-Gs. **(a,b)** Crosslinked EF-Gs CL6 (a) and CL11 (b). **(c)** WT EF-G. The numbers 11-17 indicate the bps of DNA-mRNA rulers.

Particle counting was performed on six images for every sample. The positions of the six field-of-views were indicated in Figure 4.7. A two-dimensional stage was implemented for changing the field-of-views. The remaining percentages of the beads are plotted in Figure 4.8, which were scaled to 100% for no change in particle counts and to 0% for the maximum particle loss. This normalization procedure did not affect the onset of the signal decrease. A control experiment was also performed, in which EF-G was absent

(black trace in Figure 4.8). No obvious particle decrease was observed, confirming the particle losses in the samples with EF-G were mainly due to their respective power stroke. Using the same protocol as in the magnetic detection, we obtained the onsets of signal decrease to be 14.8, 16.7, and 16.3, for CL6, CL11, and WT, respectively. They corresponded to force values of 60±6, 93±8, and 87±8 pN, respectively. Therefore, the results by microscope detection were in excellent agreement with those by magnetic detection.

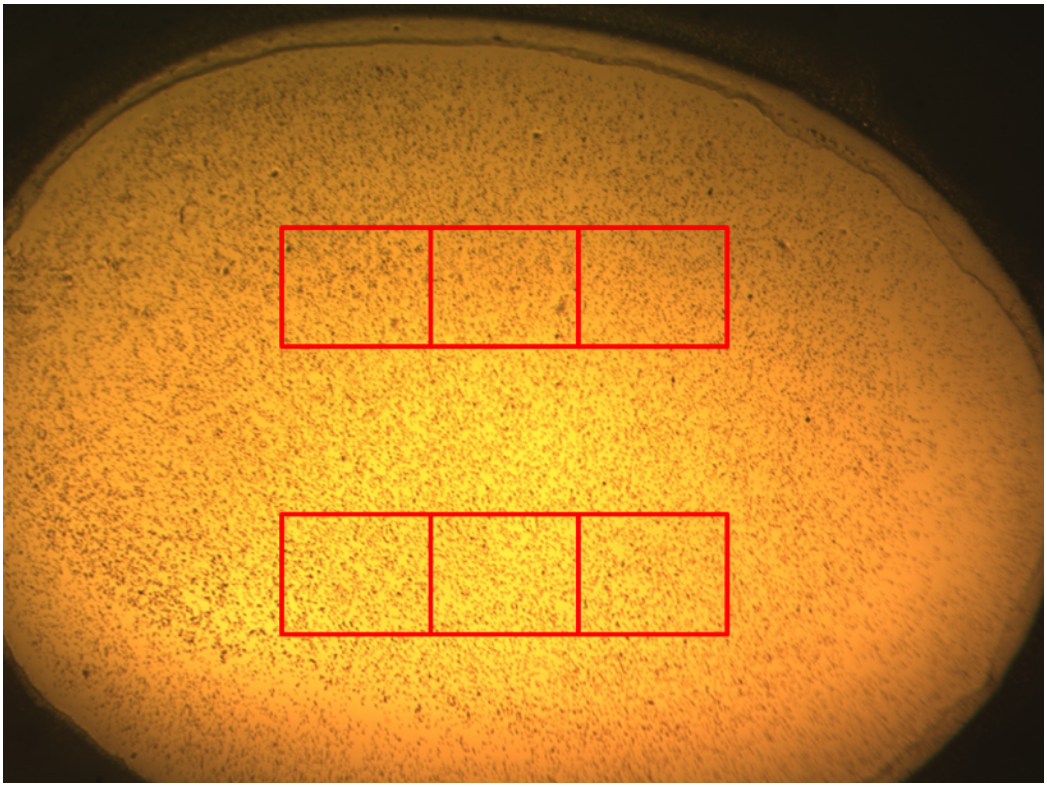

Figure 4.7 The six field-of-views to measure the power stroke with a bright field microscope. Related to Figure 4.6

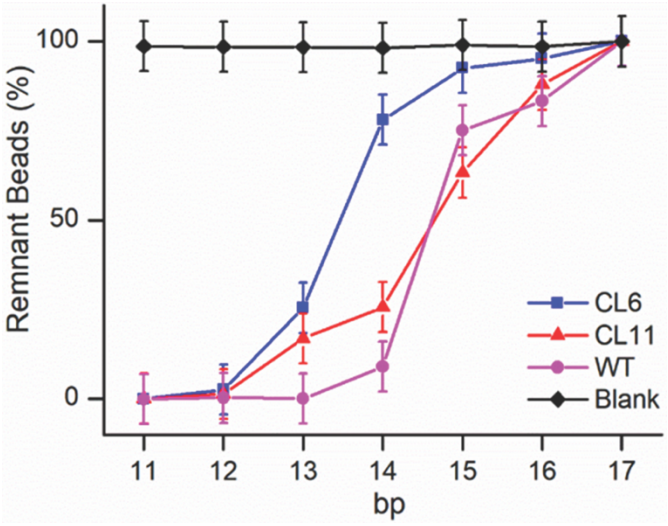

Figure 4.8 Microscope detection of EF-G power stroke measured by particle counting with a microscope. Blank was the control with no EF-G.

To further validate the microscope detection method, we carried out experiments to measure the effect of a ribosome complex reversely hybridized with a surface DNA. In this case, the 5′-end of the mRNA in the pre-translocation complex was hybridized with the DNA on the surface. Because of the direction of the power stroke, no bead dissociation should be observed even for a weak ruler. Figure 4.9 shows the images using a 12-bp ruler. Particle counting showed no significant change in immobilized particles after adding WT EF-G, consistent with both the expectation and our previous FIRMS result.[7]

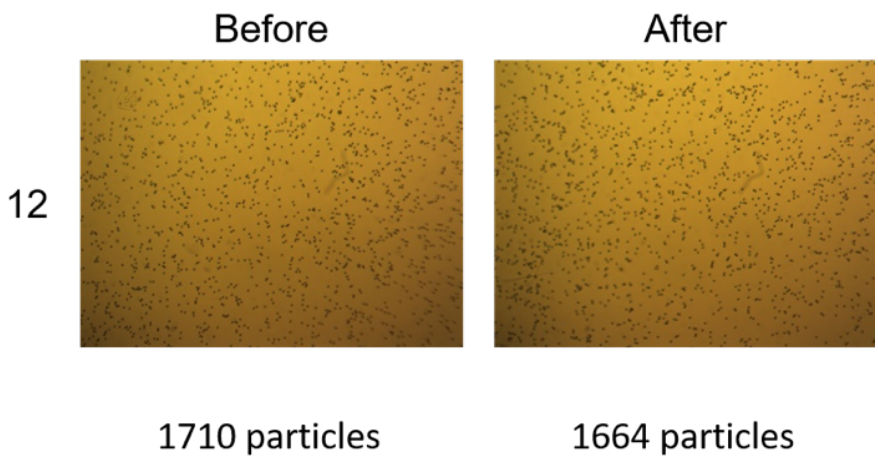

Figure 4.9 Microscope images for measuring the effect of the reversed ribosome as a control experiment. Related to Figures 4.6 and 4.8. The 5′-end mRNA of the ribosome complex formed a 12-bp duplex with the probing DNA. Because the power stroke acted at the opposite direction of pulling the duplex, no change in bead numbers was observed between before and after the addition of EF-G. The number of magnetic beads was 1710 before the addition of EF-G and 1664 afterwards.

4.3.5 Modulation of power stroke with fusidic acid

Power stroke may also be affected by other factors. Fusidic acid is known to bind near the GTP binding pocket of EF-G to prevent its dissociation from the ribosome.[33] The effect of fusidic acid binding on the EF-G power stroke is shown in Figure 4.10. The plot was obtained using the microscope method, with representative images for 12- and 15-bp DNA force rulers. For comparison, EF-G without fusidic acid was also shown. The complete set of images are shown in Figure 4.11. The data indicated that significant bead loss was observed for n = 14 rulers. The onset of slope was analyzed to be n = 15.0, corresponding to a power stroke of 62±5 pN. Therefore, the power stroke of EF-G bound with fusidic acid was much weaker than the WT. For comparison, magnetic detection was

also performed (Figure 4.12). The same onset of slope within error, n = 15.2, was obtained. Therefore, both microscopic and magnetic detections yielded the same results.

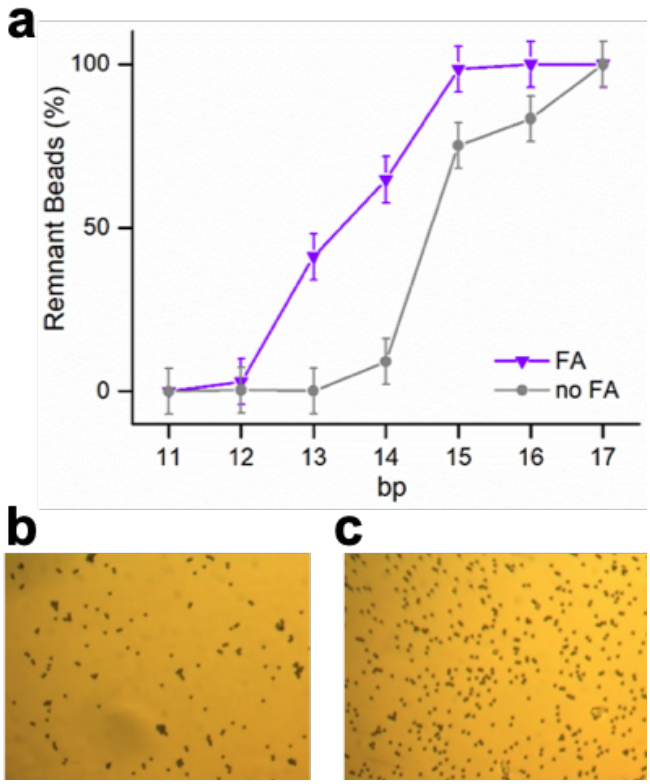

Figure 4.10 Reduced power stroke of EF-G bound with fusidic acid. **(a)** Plot of remnant magnetic beads vs. duplex basepair. WT EF-G without fusidic acid is also shown for comparison. FA: fusidic acid. **(b,c)** Representative microscope images after the power stroke for the 12- (b) and 15-bp rulers (c), respectively.

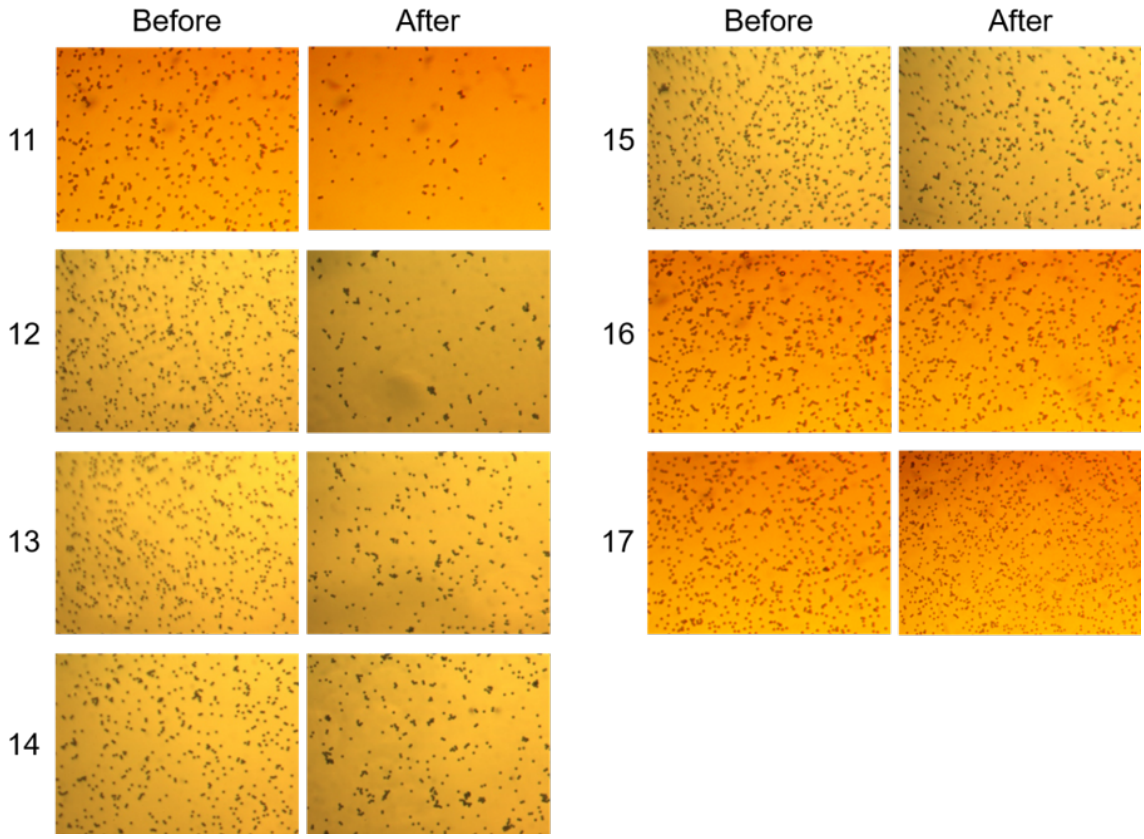

Figure 4.11 Microscope images for measuring the power stroke of EF-G bound with fusidic acid. Related to Figure 4.10. The integers at the left of the corresponding images represent the bp numbers of the DNA-mRNA duplexes.

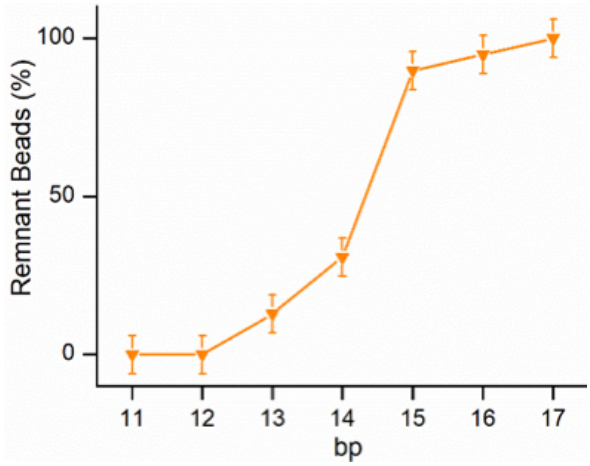

Figure 4.12 Magnetic measurements of the power stroke of EF-G bound with fusidic acid.

4.3.6 Role of mechanical force in translocation

We investigated the effect of reduced power stroke on translocation by identifying the exact ribosome movement on the mRNA. The probing scheme is shown in Figure 4.12A, which has been used in our previous publications.[34,35] Briefly, the ribosome position was revealed by the number of bp between the exposed mRNA and the probing DNA; the number of bp was deduced from the critical force of the duplexes obtained by FIRMS. In these experiments, the magnetic signal decreasing was induced by centrifugal force, on the contrary to the EF-G forces in the previous figures. Single-nt resolution has been routinely achieved. The pre-translocation complex (Pre) was indicated by the 15-bp duplex (at ~62 pN); the post-translocation complex (Post) was indicated by the 12-bp (at ~25 pN). The 3 bp difference was caused by the normal translocation step in which three more mRNA nt would be covered by the ribosome in the Post and could no longer hybridize with the probing DNA (Figure 4.13a, bottom scheme). If frameshifting occurred, we would observe 13-bp duplex for -1 frameshifting, or 14-bp duplex for -2 frameshifting, as we have demonstrated in previous publications.[34,35] The results of the ribosome positions and their corresponding percentages are shown in Figure 4.13B. The data showed that both WT and CL11 led to complete translocation since only Post was present in both cases. For CL6 and fusidic acid-bound EF-G, however, only 55±5% and 53±5% translocation occurred, respectively. The rest remained as unreacted Pre. Furthermore, no frameshifting was observed in all four experiments, because no 13- or 14-bp duplexes were observed (at the positions indicated by the green dashed lines). The results imply that decrease of EF-G force reduced the translocation speed, but did not interfere with translocation fidelity. Our

observations agreed with the hypothesis that the ribosome rRNA residues acted as "paws" to maintain the mRNA reading frames.[36]

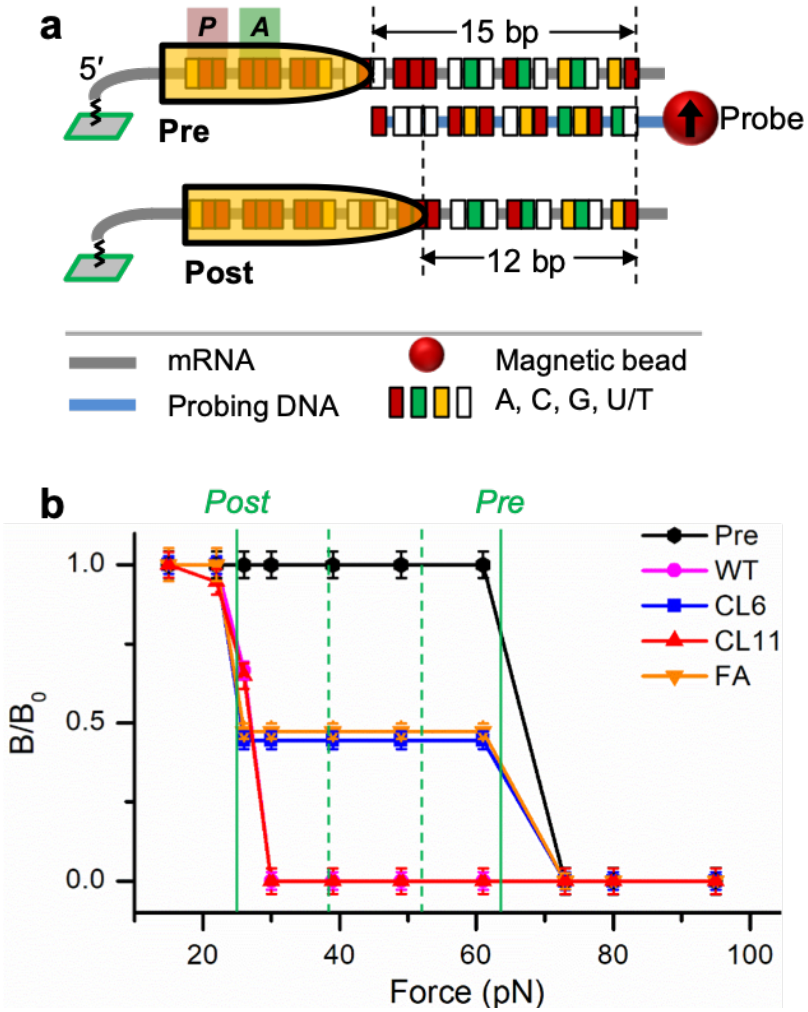

Figure 4.13 Translocation efficiency probed by FIRMS. **(a)** Probing scheme for translocation (the same ribosome complex as in the power stroke experiments). **(b)** Translocation products for different EF-Gs. The two solid lines indicate the positions of Post and Pre, respectively. The two dashed green lines indicate the expected positions of "-1" (left) and "-2" (right) frameshifting products. Both were absent in the results.

4.4 Discussion

4.4.1 A noninvasive force measurement method with visual detection

In summary, we have extended the noninvasive force measurement with magnetic sensing method to a more adaptable microscope detection. The mRNA is tethered to the surface via a DNA-mRNA duplex. The power stroke exerted on the tRNA-mRNA complex, which was transduced to shear the DNA-mRNA duplex. Because the ribosome complex was freely moving in the solution, our force measurement is noninvasive with no additional forces, in contrast to optical tweezers that requires applying a force on motor proteins.[8] We have confirmed the previously measured EF-G force with the new method, and measured two internal crosslinked EF-G mutants. Based on Equation (1), a spectrum of force and catalytic rate will reveal the transition state distance, which will be obtained in the future. Combined with the currently abundant high-resolution structures, the value of the transition state distance will shed light to the translocation mechanism.

4.4.2 Force is the sole factor to induce mRNA-DNA dissociation

The DNA-mRNA duplex paired immediately at the mRNA 3′-exit site with 15 bp length. After one round of translocation, this duplex was unzipped 3 bp by the ribosome. Based on the calibration (Figure 4.5c), the binding force changed from approximately 60 pN to 25 pN. This force was sufficient to resist thermal fluctuation, which would keep the magnetic signal unchanged in the absence of force. On the other hand, duplex formed 3 nucleotides away from the mRNA exit site still dissociate under power stroke, although in

this case the mRNA-DNA duplex did not change.[7] This experiment showed that force was the sore factor that generated signal decrease in both magnetic and microscope methods.

In theory, both Brownian diffusion and power stroke models are compatible with the processive movement of ribosome on the mRNA. Considering an average thermal energy of k_BT ($\sim\frac{3}{2}mv^2$), the most probable traveling distance d of the protein EF-G under dragging force will be less than 1 Å based on Equation (4)[6]

$$d \approx \sqrt{\frac{3*k_B*T*m}{\gamma^2}} \tag{4}$$

in which k_B is the Boltzmann constant, T is temperature, m is molecular mass, and γ is Stoke's friction coefficient. To achieve 100-fold longer distance (100 Å), the energy needs to be 10,000-fold higher, which is ~ $e^{-10,000}$ probability based on the Boltzmann distribution:

$$p_i \propto e^{-\frac{E_i}{K_BT}} \tag{5}$$

in which p_i is the relative population of molecules at energy level E_i at temperature T. Therefore, the very large conformational change of EF-G is less likely to be driven by thermal energy and more compatible with a force-driven process. X-ray structures indicated a displacement of more than 100 Å movement of domain IV (Figure 4.1a), and 37 Å (Figure 4.2), respectively. Because both results substantially exceed the average value from Brownian diffusion, the more plausible interpretation would be the power stroke model. Our previous study has provided direct quantification of power stroke that is consistent with the structural results.[4,5] In this report, the correlation of the force magnitude to the conformational change is revealed, which further confirms the power stroke model.

4.4.3 The crosslinked EF-G with decreased catalytic activity is due to less force generation

As shown in Figure 4.1F, conformational restriction compromised the ribosome's capability of synthesizing poly(Phe) peptides, but this assay alone could not reveal the mechanism of the decreased activity. Our force measurements with both magnetic and microscope detections indicate that the conformational restriction led to less force, therefore limited the ribosome translocation. Similarly, the reduced power stroke is probably also the inhibition mechanism of fusidic acid.

However, it is interesting that the less force magnitude in CL6 did not cause frameshifting. Instead, only less percentage of translocation was observed. This result agreed with the structural and kinetic studies in the literatures. The structural studies showed dynamic interactions of rRNA residues C1397 and A1503 with the mRNA residues before and during mRNA translocation.[4,31] These residues were hypothesized to be the "paws" to maintain the precise 3-nt mRNA movement. Meanwhile, kinetic studies indicated that the EF-G caused a rate-limiting ribosome unlocking step preceding mRNA translocation.[37] These results implied that the role of EF-G was to overcome the activation energy barrier that separated the pre- and post-translocation states. The consequence is to accelerate the reaction rate, but it does not directly determine the translocation stepping size. Based on this knowledge, our power stroke measurements imply that the force is probably utilized to decrease the activation barrier for a rate limiting intermediate state. It remains unclear how to correlate this transition state to the structures. More investigation

on this aspect will be needed in the future to reveal the detailed role of force in ribosomal translocation.

4.5 Conclusions

In conclusion, we have proved to successfully synthesize and purify crosslinked EF-G with two different linker lengths, one restricting EF-G motion and the other not. By applying DNA rulers to both magnetic detection and microscopic scale counting, we have quantified EF-G power strokes and correlate their amplitudes with conformational restriction and drug binding. The results show that the shorter linker of $(PEG)_6$ reduced the power stroke from 89 pN to 59 pN, whereas the longer linker, $(PEG)_{11}$, caused no change. The binding of fusidic acid also reduced the power stroke, to 62 pN that was similar to $(PEG)_6$. In addition, the results represent that the reduced power stroke only lowered the translocation yield but did not introduce translocation error. The force-structure-function correlation for EF-G indicate that power stroke drives ribosomal translocation, but the mRNA reading frame is probably maintained by ribosome itself.

4.6 References

1. Dunkle, J. A. & Cate, J. H. D. Ribosome structure and dynamics during translocation and termination. *Annu. Rev. Biophys.* **39**, 227–244 (2010).
2. Katunin, V. I., Savelsbergh, A., Rodnina, M. V. & Wintermeyer, W. Coupling of GTP hydrolysis by elongation factor G to translocation and factor recycling on the ribosome. *Biochemistry* **41**, 12806–12812 (2002).
3. Achenbach, J. & Nierhaus, K. H. The mechanics of ribosomal translocation. *Biochimie* **114**, 80–89 (2015).
4. Zhou, J., Lancaster, L., Donohue, J. P. & Noller, H. F. How the ribosome hands the A-site tRNA to the P site during EF-G-catalyzed translocation. *Science* **345**, 1188–1191 (2014).
5. Lin, J., Gagnon, M. G., Bulkley, D. & Steitz, T. A. Conformational changes of elongation factor G on the ribosome during tRNA translocation. *Cell* **160**, 219–227 (2015).
6. Moore, P. B. How should we think about the ribosome? *Annu. Rev. Biophys.* **41**, 1–19 (2012).
7. Yao, L., Li, Y., Tsai, T.-W., Xu, S. & Wang, Y. Noninvasive measurement of the mechanical force generated by motor protein EF-G during ribosome translocation. *Angew Chem. Int. Ed.* **52**, 14041-14044 (2013).
8. Liu, T., Kaplan, A., Alexander, L., Yan, S., Wen, J. D. *et al.* Direct measurement of the mechanical work during translocation by the ribosome. *eLife* **3**, e03406 (2014).
9. Chen, C., Cui, X., Beausang, J. F., Zhang, H., Farrell, L. *et al.* Elongation factor G initiates translocation through a power stroke. *Proc. Natl. Acad. Sci.* **113**, 7515–7520 (2016).
10. De Silva, L., Yao, L., Wang, Y. & Xu, S. Well-defined and sequence-specific noncovalent binding forces of DNA. *J. Phys. Chem. B* **117**, 7554–7558 (2013).
11. Albrecht, C., Blank, K., Lalic-Muthaler, M., Hirler, S., Mai, T. *et al.* DNA: a programmable force sensor. *Science* **301**, 367–370 (2003).
12. Albrecht, C. H., Clausen-Schaumann, H. & Gaub, H. E. Differential analysis of biomolecular rupture forces. *J. Phys. Condens. Matter* **18**, S581–S599 (2006).
13. Neuert, G., Albrecht, C. H. & Gaub, H. E. Predicting the rupture probabilities of molecular bonds in series. *Biophys. J.* **93**, 1215–1223 (2007).
14. Wilson, K. S. & Noller, H. F. Mapping the position of translational elongation factor EF-G in the ribosome by directed hydroxyl radical probing. *Cell* **92**, 131–139 (1998).
15. Wang, Q., Young, P. & Walters, K. J. Structure of S5a bound to monoubiquitin provides a model for polyubiquitin recognition. *J. Mol. Biol.* **348**, 727–739 (2005).

16. Gao, Y.-G., Selmer, M., Dunham, C. M., Weixlbaumer, A., Kelley, A. C. *et al.* The structure of the ribosome with elongation factor G trapped in the posttranslocational state. *Science* **326**, 694–699 (2009).
17. Altuntop, M. E., Ly, C. T. & Wang, Y. Single-molecule study of ribosome hierarchic dynamics at the peptidyl transferase center. *Biophys. J.* **99**, 3002–3009 (2010).
18. Bell, G. I. Models for the specific adhesion of cells to cells. *Science* **200**, 618–627 (1978).
19. Evans, E. & Ritchie, K. Dynamic strength of molecular adhesion bonds. *Biophys. J.* **72**, 1541–1555 (1997).
20. Oberbarnscheidt, L., Janissen, R. & Oesterhelt, F. Direct and model free calculation of force-dependent dissociation rates from force spectroscopic data. *Biophys. J.* **97**, L19–L21 (2009).
21. Evans, E. & Ritchie, K. Strength of a weak bond connecting flexible polymer chains. *Biophys. J.* **76**, 2439–2447 (1999).
22. Green, N. H., Williams, P. M., Wahab, O., Davies, M. C., Roberts, C. J. *et al.* Single-molecule investigations of RNA dissociation. *Biophys. J.* **86**, 3811–3821 (2004).
23. Ikuta, S., Takagi, K., Wallace, R. B. & Itakura, K. Dissociation kinetics of 19 base paired oligonucleotide-DNA duplexes containing different single mismatched base pairs. *Nucleic Acids Res.* **15**, 797–811 (1987).
24. Mosayebi, M., Louis, A. A., Doye, J. P. K. & Ouldridge, T. E. Force-induced rupture of a DNA duplex: from fundamentals to force sensors. *ACS Nano* **9**, 11993–12003 (2015).
25. Rauzan, B., McMichael, E., Cave, R., Sevcik, L. R., Ostrosky, K. *et al.* Kinetics and thermodynamics of DNA, RNA, and hybrid duplex formation. *Biochemistry* **52**, 765–772 (2013).
26. Zhang, W. & Chen, S.-J. Exploring the complex folding kinetics of RNA hairpins: II. effect of sequence, length, and misfolded states. *Biophys. J.* **90**, 778–787 (2006).
27. Hatch, K., Danilowicz, C., Coljee, V. & Prentiss, M. Demonstration that the shear force required to separate short double-stranded DNA does not increase significantly with sequence length for sequences longer than 25 base pairs. *Phys. Rev. E* **78**, 011920 (2008).
28. Sheetz, M. P. & Spudich, J. A. Movement of myosin-coated fluorescent beads on actin cables in vitro. *Nature* **303**, 31–35 (1983).
29. Block, S. M., Goldstein, L. S. & Schnapp, B. J. Bead movement by single kinesin molecules studied with optical tweezers. *Nature* **348**, 348–352 (1990).
30. Menard, K. P. Dynamic mechanical analysis : a practical introduction, second edition. (CRC Press, 2008). doi:10.1201/9781420053135
31. Kleinschmidt, A. T. & Lipomi, D. J. Stretchable conjugated polymers: a case study in topic selection for new research groups. *Acc. Chem. Res.* **51**, 3134–3143 (2018).

32. Schneider, C. A., Rasband, W. S. & Eliceiri, K. W. NIH Image to ImageJ: 25 years of image analysis. *Nat. Methods* **9**, 671–675 (2012).
33. Noller, H. F., Lancaster, L., Mohan, S. & Zhou, J. Ribosome structural dynamics in translocation: yet another functional role for ribosomal RNA. *Q. Rev. Biophys.* **50**, e12 (2017).
34. Tsai, T.-W., Yang, H., Yin, H., Xu, S. & Wang, Y. High-efficiency '-1' and '-2' ribosomal frameshiftings revealed by force spectroscopy. *ACS Chem. Biol.* **12**, 1629–1635 (2017).
35. Yin, H., Xu, S. & Wang, Y. Dual DNA rulers reveal an 'mRNA looping' intermediate state during ribosome translocation. *RNA Biol.* **15**, 1392–1398 (2018).
36. Zhou, J., Lancaster, L., Donohue, J. P. & Noller, H. F. Crystal structures of EF-G–ribosome complexes trapped in intermediate states of translocation. *Science* **340**, 1236086 (2013).
37. Savelsbergh, A., Katunin, V. I., Mohr, D., Peske, F., Rodnina, M. V. *et al.* An elongation factor G-induced ribosome rearrangement precedes tRNA-mRNA translocation. *Mol. Cell* **11**, 1517–1523 (2003).

Chapter 5 Conclusions

This thesis investigates the mechanism of ribosomal translocation and quantification of the EF-G power stroke forces via precise magnetic DNA rulers. Tracking of ribosomal position with single-nucleotide resolution was achieved. The mechanical force of power stroke was also directly measured by both magnetic detection and particle-counting using a microscope.

By unique probing the 3′-end of mRNA with the magnetic DNA rulers, we have unambiguously revealed the highly efficient "-1" and "-2" frameshiftings on a GA_7G slippery mRNA without the downstream secondary structure, using force-induced remnant magnetization spectroscopy (FIRMS). Two significant insights for the frameshifting mechanism were revealed. First, EF-G·GTP is indispensable to frameshifting. Although EFG·GDPCP has been shown to prompt translocation before, we found that it could not induce frameshifting. This implies that the GTP hydrolysis is responsible for the codon-anticodon repairing in frameshifting, which corroborates our previous mechanical force measurement of EF-G·GTP. Second, translation in all three reading frames of the slippery sequence can be induced by the corresponding in-frame aminoacyl tRNAs. Although A-site tRNA is known to affect the partition between "0" and "-1" frameshifting, it has not been reported that all three reading frames can be translated by their corresponding tRNAs.

To achieve a complete position tracking of ribosome, a dual magnetic DNA rulers assay was developed that uniquely probing both the 3′- and 5′-ends of mRNA. An antibiotic-trapped intermediate state was observed that is consistent with a ribosomal

conformation containing mRNA asymmetric partial displacements at its entry and exit sites. Based on the available ribosome structures and computational simulations, a 'looped' mRNA conformation was proposed, which suggested a stepwise 'inchworm' mechanism for ribosomal translocation. The same 'looped' intermediate state identified with the dual rulers persists with a '-1' frameshifting motif, indicating that the branching point of normal and frameshifting translocations occurs at a later stage of translocation.

In Chapter 4, we have successfully synthesized and purified crosslinked EF-G with two different linker lengths, one restricting EF-G motion and the other not. By applying DNA rulers to both magnetic detection and microscopic scale counting, we have quantified EF-G power strokes and correlate their amplitudes with conformational restriction and drug binding. The results showed that the shorter linker of $(PEG)_6$ reduced the power stroke from 89 pN to 59 pN, whereas the longer linker, $(PEG)_{11}$, caused no change. The binding of fusidic acid also reduced the power stroke, to 62 pN that was similar to $(PEG)_6$. In addition, the results indicated that the reduced power stroke only lowered the translocation yield but did not introduce translocation error. The force-structure-function correlation for EF-G indicate that power stroke drives ribosomal translocation, but the mRNA reading frame is probably maintained by ribosome itself.